

Olivine–metal mixtures: Spectral reflectance properties and application to asteroid reflectance spectra



Edward A. Cloutis^{a,*}, Juan A. Sanchez^b, Vishnu Reddy^c, Michael J. Gaffey^d, Richard P. Binzel^e, Thomas H. Burbine^f, Paul S. Hardersen^d, Takahiro Hiroi^g, Paul G. Lucey^h, Jessica M. Sunshineⁱ, Kimberly T. Tait^j

^a Department of Geography, University of Winnipeg, 515 Portage Avenue, Winnipeg, MB R3B 2E9, Canada

^b Max Planck Institut für Sonnensystemforschung, Göttingen, Germany

^c Planetary Science Institute, 1700 East Fort Lowell, Suite 106, Tucson, AZ 85719-2395, USA

^d Space Studies Department, John D. Odegard School of Aerospace Sciences, University of North Dakota, Grand Forks, ND 58202-9008, USA

^e Department of Earth, Atmospheric, and Planetary Sciences, Massachusetts Institute of Technology, Cambridge, MA 02139, USA

^f Department of Astronomy, Mount Holyoke College, South Hadley, MA 01075, USA

^g Department of Geological Sciences, Brown University, Box 1846, Providence, RI 02912, USA

^h Hawaii Institute of Geophysics and Planetology, University of Hawaii, 1680 East-West Road, Honolulu, HI 96822, USA

ⁱ Department of Astronomy, University of Maryland, College Park, MD 20742, USA

^j Royal Ontario Museum, Department of Natural History, Toronto, ON M5S 2C6, Canada

ARTICLE INFO

Article history:

Received 8 April 2014

Revised 12 September 2014

Accepted 1 October 2014

Available online 13 October 2014

Keywords:

Asteroids, composition

Meteorites

Mineralogy

Regoliths

Spectroscopy

ABSTRACT

Olivine-rich asteroids appear to be common in the main asteroid belt as well as present in the near-Earth asteroid population. There are a number of meteorite classes that are dominated by olivine ± metal. To determine whether relationships exist between these asteroids and meteorites, we spectrally characterized a number of olivine + meteoritic metal powder intimate and areal mixtures, pallasite slabs, and olivine powders on a metal slab. Our goal is to understand the spectral characteristics of olivine + metal assemblages and develop spectral metrics that can be used to analyze reflectance spectra of olivine-dominated asteroids. We found that the major olivine absorption band in the 1 μm region is resolvable in intimate mixtures for metal abundances as high as ~90 wt.%. The wavelength position of the 1 μm region olivine absorption band center is sensitive to Fa content but insensitive to other variables. However, the band minimum position moves to shorter wavelengths with increasing metal abundance due to changes in spectral slope. The full width at half maximum (FWHM) of this band and reflectance at 1.8 μm are both most sensitive to olivine Fa content, metal abundance, and grain size, and much less to the presence of nanophase iron that reddens spectra. Reflectance at 0.56 μm and the 1.8/0.56 μm reflectance ratio are sensitive to these same parameters as well as to nanophase iron-associated spectral reddening. The wavelength position of the local reflectance maximum in the 0.7 μm region moves to longer wavelengths with increasing metal abundance and is most useful for constraining metal abundance in high metal-content mixtures. Pallasite slab spectra differ in a number of respects from powdered assemblages and multiple spectral parameters can be used to discriminate them. The spectra of increasingly fine-grained olivine + metal assemblages and those involving low-Fa olivine show increasing spectral dominance by metal. Systematic application of multiple spectral metrics allows olivine + metal assemblage properties such as Fa content, olivine/metal ratio, and grain size to be quantified or constrained. Analysis of reflectance spectra of 22 presumed olivine ± metal-rich asteroids indicates that most of them possess low- to medium-Fa content olivine (Fa_{~67}), with variable abundances of macroscopic metal. A number exhibit visible region absorption bands that are indicative of some fraction of coarser-grained olivine (>45 μm). Most asteroid spectra can be plausibly linked to specific olivine ± metal-bearing meteorite classes. Most of the asteroid spectra examined exhibit some degree of spectral reddening below ~1.8 μm which is most consistent with the presence of fine-grained nanophase iron, likely produced by space weathering.

© 2014 Elsevier Inc. All rights reserved.

* Corresponding author. Fax: +1 (204) 774 4134.

E-mail addresses: e.cloutis@uwinnipeg.ca (E.A. Cloutis), sanchez@mps.mpg.de (J.A. Sanchez), reddy@psi.edu (V. Reddy), gaffey@space.edu (M.J. Gaffey), rpb@mit.edu (R.P. Binzel), tburbine@mholyoke.edu (T.H. Burbine), hardersen@space.edu (P.S. Hardersen), takahiro_hiroi@brown.edu (T. Hiroi), lucey@higp.hawaii.edu (P.G. Lucey), jess@astro.umd.edu (J.M. Sunshine), ktait@rom.on.ca (K.T. Tait).

1. Introduction

Olivine ± metal-rich asteroids appear to be relatively common in the main asteroid belt (e.g., Cruikshank and Hartmann, 1984; Sunshine et al., 2007; Sanchez et al., 2014), and are also present in the near-Earth asteroid population (Reddy et al., 2011b). Previous analyses of reflectance spectra for these bodies have focused on determining olivine composition, and only roughly constraining metal abundance and grain size. The observational data has also suggested spectral variability among these bodies. This variability is matched by the compositional variability that exists among olivine ± metal meteorites: multiple olivine ± metal-dominated meteorite classes exist, ranging from primitive to differentiated. Collectively, this suggests that multiple parent bodies, characterized by varying olivine/metal ratios and olivine composition, and ranging from primitive to differentiated, should be present in the main asteroid belt and possibly among the near-Earth asteroid population.

This study was motivated by the fact that even though a number of meteorite classes are composed largely of olivine + metal, and, by implication, the potentially large number of associated parent bodies, there exists a lack of systematic examination of the spectral reflectance properties of olivine + metal assemblages. In particular we were interested in examining how varying olivine/metal ratios affect spectral properties and metrics such as absolute reflectance, spectral slope, absorption band minima and centers, and band widths. Our goal was to provide guidelines that enable olivine + metal assemblages to be uniquely recognized and develop spectral metrics that can be used to constrain these properties.

1.1. Background

Many classes of meteorites contain varying proportions of metal and mafic silicates. A number of these contain olivine ± metal as the dominant component(s) and include both primitive and differentiated meteorite classes. Relevant meteorite classes include primitive chondrites such as CB carbonaceous chondrites, and partially- or

fully-differentiated groups and/or impact-generated assemblages such as lodranites, pallasites, IAB and IIE iron meteorites. Meteorite classes that contain olivine as the dominant mafic silicate, but with low abundances of metal, include many angrites, ureilites, R chondrites, olivine diogenites, brachinites, the chassignite Mars meteorites, CR, CO, CV, CK, and CH carbonaceous chondrites. Consequently, we expect olivine ± metal assemblages to be common among asteroids. The major meteorite groups that include at least some members that contain olivine as the dominant mafic silicate ± metal are summarized in Table 1.

Spectroscopy-based characterization of the parent bodies of olivine ± metal meteorites has been hampered by a dearth of laboratory reflectance spectra of relevant assemblages. The few existing studies have shown that the addition of macroscopic metal causes reddening of spectral slope, decreases in olivine absorption band depths, and movement of the major 1 μm region olivine absorption band minimum to shorter wavelengths (e.g., Cloutis et al., 1990; Hiroi and Takeda, 1991; Burbine et al., 2007).

Polarimetric data suggest that asteroid regoliths are fine-grained, implying that metal on asteroid surfaces will exist in particulate form (e.g., Dollfus, 1971; Dollfus and Geake, 1975; Dollfus et al., 1979). Because of the difficulties in producing powdered metal for spectral measurements, most studies that have examined olivine + metal assemblage spectra have been confined to slabs (e.g., Hiroi and Takeda, 1991; Hiroi et al., 1992). Studies that examined powdered assemblages (e.g., Cloutis et al., 1990) involved only a limited number of samples. As shown by Britt and Pieters (1988) and Cloutis et al. (2010a), metal slab spectra can be very spectrally variable, depending on surface roughness and viewing geometry, while metal powder spectra generally show a much more constrained range of spectral variability (Cloutis et al., 2010a).

2. Spectral reflectance properties of olivine and metal

Olivine reflectance spectra (0.3–2.5 μm) are dominated by absorption bands attributable to spin-allowed crystal field

Table 1
Characteristics of olivine ± metal-dominated meteorites. Sources of data: Keil (1962, 1968), Mason (1963, 1965), Keil and Fredriksson (1964), Powell (1969, 1971), Mason and Jarosewich (1973), Scott and Bild (1974), Scott and Wasson (1975, 1976), Buseck (1977), Graham et al. (1977), Scott (1977), Floran et al. (1978), Prinz et al. (1980), Grossman et al. (1988), McKay et al. (1988), McCoy et al. (1993, 1996), Schulze et al. (1994), Yanai (1994), Bischoff et al. (1994), Benedix et al. (1995, 2000), Kallemeyn et al. (1996), Brearley and Jones (1998), Mittlefehldt et al. (1998, 2003), Grossman and Zipfel (2001), Weisberg et al. (2001, 2002), Goodrich et al. (2012), Warren and Rubin (2012), Cloutis et al. (2013), Corder et al. (2013, 2014), Gardner-Vandy et al. (2013), Hyde et al. (2013) and Larouci et al. (2013).

Meteorite class	Metal abundance (wt.%)	Mafic silicate abundance (wt.%) and composition
<i>Primitive meteorites</i>		
CB chondrites	~70–90	OLV (Fa ₂₋₃) > LCP
CH chondrites	~30	LCP > OLV (Fa ₀₋₃)
CK chondrites	<1	OLV (Fa ₂₉₋₃₃) > PYX
CO chondrites	0–8	OLV (Fa ₃₀₋₆₀) > PYX
CR chondrites	~10–16	OLV (Fa ₁₋₅) > PYX
CV chondrites	0–8	OLV (Fa ₁₀₋₆₀) > PYX
R chondrites	<1	60–75% OLV (Fa ₃₇₋₄₀); 7–13% PYX
<i>Differentiated meteorites</i>		
Angrites	<1	0–64% OLV (Fa ₄₀₋₁₀₀); HCP
Brachinites	<1	79–93% OLV (Fa ₂₅₋₄₀); 1–15% PYX
Chassignites	<1	OLV (Fa ₃₁)
IAB irons	Variable	Variable: OLV (Fa ₁₋₈); LCP (Fs ₁₋₉)
IIE irons	Variable	Variable: OLV (Fa ₁₅₋₂₀) and LCP (Fs ₁₄₋₂₄)
Lodranites	~15–40	Variable OLV (Fa ₃₋₁₅); LCP (Fs ₄₋₁₄)
Olv-diogenites	<1	Up to >90% OLV (Fa _{7,5})
Pallasites	~25–75	~25–75% OLV (Fa ₁₀₋₁₂ ; 18–20)
Pyroxene pallasites	60–90	8–30% OLV (Fa ₁₁), 1–20% LCP
Ureilites	<1	Variable OLV (Fa ₅₋₂₂); LCP (Fs ₄₋₂₀)
LEW88763	<4	OLV (Fa ₃₆) ≫ PYX
MIL 090206	<1	OLV (Fa ₂₈) ≫ PYX
MIL090405	<1	OLV (Fa ₂₇) ≫ PYX
MIL 090340	<1	OLV (Fa ₂₈) ≫ PYX
NWA 5363	<1	80% OLV (Fa ₃₀) > PYX
NWA 7680	Variable	OLV (Fa ₄₅)

Abbreviations: HCP: high-calcium pyroxene; LCP: low-calcium pyroxene; OLV: olivine; PYX: pyroxene.

transitions in Fe^{2+} . These transitions give rise to two absorption bands near 0.85 and 1.25 μm due to Fe^{2+} located in the M1 crystallographic coordination site, and a band near 1.05 μm , attributable to Fe^{2+} located in the M2 site (Burns, 1970; King and Ridley, 1987; Sunshine and Pieters, 1998). Fe^{2+} partitions approximately equally into the M1 and M2 sites (Burns, 1970), and this composite feature results in a strong absorption band near 1.05 μm , with weaker shoulders near 0.85 and 1.25 μm . With increasing Fe^{2+} content, the center of this composite band moves from ~ 1.048 to 1.096 μm , and the side bands appear to become deeper relative to the central band (Fig. 1a and b). Olivine also exhibits weaker absorption bands below 0.7 μm which are attributable to various causes (Sunshine and Pieters, 1998), and which become more evident in larger grain size spectra (Cloutis, 1997) (Fig. 1c). The bands near 0.400, 0.450, and 0.495 μm are attributed to spin forbidden

transitions in Fe^{2+} (Burns et al., 1972), while the cause of a weak band near 0.65 μm is uncertain, but is present in nearly all fine-grained ($<45 \mu\text{m}$) olivine spectra (King and Ridley, 1987; Sunshine and Pieters, 1998; Sunshine et al., 2007). It likely includes contributions from both Fe^{2+} and Ni^{2+} , as the latter strongly partitions into olivine from a basaltic melt (Wood, 1974; Rossman et al., 1981; Rager et al., 1988).

2.1. Meteoritic versus terrestrial olivines

Reflectance spectra of olivine separates from olivine-bearing meteorites (e.g., pallasites, brachinites, chassignites, R chondrites) are all dominated by the major olivine absorption band in the 1 μm region (Fig. 1d). Overall spectra slopes, as measured by the 1.8/0.56 μm reflectance ratio (Table 2) range from slightly to

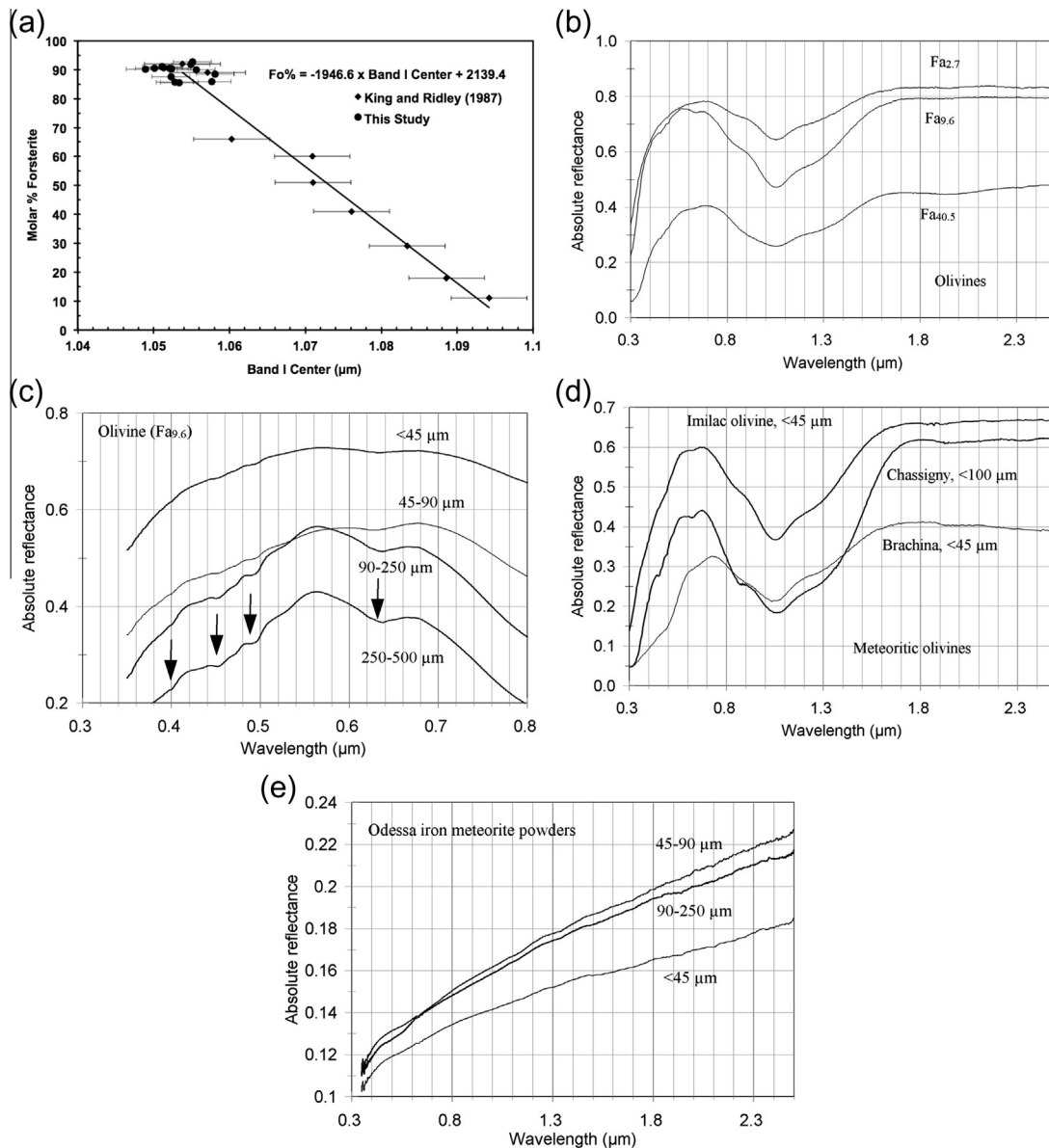


Fig. 1. Reflectance spectra of olivine and metal. (a) Improved olivine calibration plot developed by Reddy et al. (2011b) after combining data from King and Ridley (1987) and this study, showing relationship between band I center and Fo content. The solid line represents a linear fit to the data. The linear best fit equation is provided. (b) Olivines of varying Fe^{2+} (Fa) content showing decreasing reflectance and increasing band depth with increasing Fa content; all spectra are for $<45 \mu\text{m}$ size powders. (c) Olivine of constant Fa content and varying grain size showing how minor absorption bands in the visible region (i.e., near 0.400, 0.455, 0.495, and 0.625 μm , indicated by arrows) become more apparent with increasing grain size. (d) RELAB spectra of olivine from Imilac pallasite (this study), and whole rock powders of Brachina and Chassigny (from RELAB public data base; the Chassigny spectrum may be for a $<50 \mu\text{m}$ size powder). (e) Reflectance spectra of powdered samples of the Odessa octahedrite iron meteorite; thinnest line: $<45 \mu\text{m}$; medium line: 45–90 μm ; thickest line: 90–250 μm .

Table 2
Selected spectral parameters for olivine-rich meteorites and olivine ± metal ± chromite spectra.

Meteorite ^a	Reflectance at 0.56 μm (%)	Reflectance ratios			1 μm band depth (%)	Band minimum (μm)	Band center (μm)	0.7 μm position	FWHM ^c (nm)
		2.4/1.8 μm	1.8/0.56 μm	0.6/0.4 μm					
Brachina	22	0.94	1.27	3.00	34	1.055	1.055	0.72	380
Brenham	49	1.01	1.13	1.55	34	~1.07	~1.07	~0.68	400
Chassigny1	34	1.00	1.35	1.35	77	1.065	1.070	0.67	530
Chassigny2	42	0.99	1.48	1.21	64	1.060	1.060	0.68	550
Chassigny3	35	1.03	1.41	2.28	72	~1.05	~1.055	0.68	520
EET 99402	16	0.98	1.18	2.10	54	~1.07	~1.07	0.68	520
Imilac	58	1.01	1.14	1.60	40	1.060	1.065	0.68	480
NWA 753	12	0.98	1.18	2.10	14	~1.05	~1.05	~0.74	~400
Rumuruti	18	0.98	1.12	1.30	30	~1.07	~1.07	~0.65	480
Thiel Mountain	31	1.02	1.13	1.19	44	~1.05	~1.055	0.68	500
wt.% olv.									
<i>Series OM1: Intimate mixtures: 25 wt.% intervals: OLV003/MET101 (both 45–90 μm) RELAB (i = 0°, e = 15°)</i>									
100	67.0	1.02	1.11	1.36	67.8	1.054	1.057	0.56	665
75	25.8	1.09	1.21	1.05	34.0	1.046	1.054	0.67	450
50	15.6	1.13	1.49	1.14	12.1	1.038	1.053	0.73	265
25	12.1	1.16	1.78	1.21	2.3	n.p.	1.037	0.73	150
0	10.3	1.18	2.06	1.22	0	n.p.	n.p.	n.p.	0
<i>Series OM2: Intimate mixture: 50 wt.% intervals: OLV003/MET101 (both <45 μm) RELAB (i = 0°, e = 15°)</i>									
100	76.0	0.99	1.06	1.21	41.0	1.055	1.055	0.56	535
50	36.6	1.02	1.09	1.07	13.8	1.049	1.054	0.69	350
0	9.9	1.13	1.92	1.35	0	n.p.	n.p.	n.p.	0
<i>Series OM3: Intimate mixture: 50 wt.% intervals: OLV003/MET101A (both 45–90 μm) HOSERLab (i = 30°, e = 0°)</i>									
100	45.0	1.01	1.12	1.34	63.6	1.054	1.055	0.56	635
50	15.4	1.08	1.20	1.10	18.3	1.046	1.053	0.69	435
0	9.3	1.10	1.45	1.12	0	n.p.	n.p.	n.p.	0
<i>Series OM3A: Areal mixture: 50 wt.% intervals: OLV003/MET101A (both 45–90 μm) HOSERLab (i = 30°, e = 0°)</i>									
100	45.0	1.01	1.12	1.34	63.6	1.054	1.055	0.56	635
50	26.5	1.02	1.17	1.34	51.0	1.039	1.054	0.56	615
0	9.3	1.10	1.45	1.12	0	n.p.	n.p.	n.p.	0
<i>Series OM4: Intimate mixtures: 10 wt.% intervals OLV003/MET101A (both <45 μm) HOSERLab (i = 30°, e = 0°)</i>									
100	57.1	0.98	1.04	1.20	32.9	1.053	1.054	0.60	490
90	38.0	0.99	1.00	1.08	19.8	1.054	1.054	0.66	390
80	27.3	0.99	1.00	1.06	13.7	1.053	1.053	0.65	370
70	23.1	1.00	1.01	1.05	10.7	1.053	1.051	0.69	360
60	18.8	1.01	1.02	1.05	8.0	1.051	1.052	0.71	345
50	16.7	1.02	1.06	1.05	6.0	1.050	1.055	0.76	360
40	14.0	1.04	1.10	1.06	4.4	1.047	1.055	0.77	285
30	12.3	1.07	1.14	1.07	1.6	1.030	1.048	0.91	190
20	12.0	1.07	1.20	1.06	1.5	1.032	1.054	0.97	190
10	10.4	1.07	1.27	1.07	0.9	n.p.	1.045	1.01	205
0	11.9	1.10	1.35	1.13	0	n.p.	n.p.	n.p.	0
<i>Series OM4A: Areal mixtures: 10 wt.% intervals OLV003/MET101A (both <45 μm) HOSERLab (i = 30°, e = 0°)</i>									
100	57.1	0.98	1.04	1.20	32.9	1.053	1.054	0.60	490
90	52.6	0.99	1.05	1.18	32.7	1.053	1.054	0.61	490
80	48.0	0.99	1.06	1.19	31.7	1.052	1.053	0.61	475
70	43.5	0.99	1.07	1.18	30.4	1.052	1.053	0.67	475
60	39.0	1.00	1.08	1.17	28.9	1.050	1.054	0.67	465
50	34.5	1.01	1.10	1.17	26.9	1.050	1.054	0.67	465
40	30.0	1.01	1.11	1.18	24.2	1.049	1.053	0.68	475
30	19.7	1.04	1.17	1.16	17.7	1.045	1.053	0.68	450
20	21.0	1.04	1.18	1.16	16.2	1.043	1.054	0.68	460

10	16.4	1.06	1.24	1.15	9.1	1.031	1.053	0.72	410
0	11.9	1.10	1.35	1.13	0	n.p.	n.p.	n.p.	0
Series OM5: Intimate mixture: 50 wt.% intervals: OLV011/MET101 (both <45 μm) HOSERLab ($i = 30^\circ$, $e = 0^\circ$)									
100	20.7	1.02	1.57	2.93	46.1	1.073	1.084	0.70	675
50	17.2	1.06	1.26	1.58	23.8	1.053	1.079	0.67	675
0	11.9	1.10	1.35	1.13	0	n.p.	n.p.	n.p.	0
Series OM6: Intimate mixture: 50 wt.% intervals: OLV007/MET101 (both <45 μm) HOSERLab ($i = 30^\circ$, $e = 0^\circ$)									
100	71.7	1.00	1.09	1.20	20.0	1.052	1.055	0.67	485
50	25.2	1.02	1.09	1.03	3.0	1.032	1.044	0.78	345
0	11.9	1.10	1.35	1.13	0	n.p.	n.p.	n.p.	0
Series OM7: OLV003 (<45 μm) sprinkled on roughened Odessa iron meteorite slab: 4 coating thicknesses HOSERLab ($i = 30^\circ$, $e = 0^\circ$)									
No coating	29.5	1.02	1.12	0.98	0	n.p.	n.p.	0.45	0
Light	26.1	1.05	1.23	1.03	4.4	1.024	1.070	0.48	655
Medium	34.0	1.04	1.19	1.04	14.1	1.045	1.056	0.56	525
Heavy	50.3	1.02	1.09	1.08	28.2	1.053	1.057	0.56	475
Heaviest	48.0	1.03	1.07	1.14	30.0	1.057	1.059	0.56	540
Pure olv ^b	50.0	1.02	1.04	1.17	27.7	1.060	1.064	0.59	580
Series OM8: MET030 (Imilac pallasite) roughened slab: 4 spot spectra HOSERLab ($i = 30^\circ$, $e = 0^\circ$)									
Spot 1	11.9	0.99	1.29	1.26	52.0	1.300	1.354	0.67	895
Spot 2	11.6	0.98	1.29	1.21	36.4	1.300	1.389	0.68	935
Spot 3	15.3	1.09	1.43	1.06	11.5	0.820	1.067	0.67	985
Spot 4	20.7	1.08	1.25	1.11	11.5	0.825	1.281	0.67	880
Series OM8R1: Y-8451 pallasite roughened slab: 3 diffuse non-specular spot spectra (RELAB; Hiroi et al., 1992)									
Spot 1	13.9	0.88	1.38	1.20	16.8	~0.95	n.d.	0.71	590
Spot 2	14.7	0.87	1.40	1.42	22.0	~1.02	n.d.	0.71	650
Spot 3	16.6	0.91	1.36	1.32	19.5	~1.05	n.d.	0.72	630
Series OM8R2: Imilac pallasite roughened slab: 4 diffuse non-specular spot spectra (RELAB; Hiroi et al., 1992)									
Spot 1 (rough)	18.0	0.78	1.23	1.79	28.3	~1.01	n.d.	0.70	670
Spot 2 (smooth)	15.8	0.68	1.59	2.42	64.8	~1.05	n.d.	0.69	740
Spot 3 (rough)	13.3	0.68	1.09	1.56	42.3	~1.08	n.d.	0.69	720
Spot 4 (smooth)	9.8	0.50	1.64	2.24	65.1	~1.08	n.d.	0.68	740
Series OM9: Intimate mixtures: 90/10 wt.% OLV003/CHR103 and 67.5/22.5/10 wt.% OLV003/MET101/CHR103 (all <45 μm) HOSERLab ($i = 30^\circ$, $e = 0^\circ$)									
100	66.0	0.99	1.06	1.20	41.0	1.054	1.048	0.56	535
90	36.5	0.87	1.27	1.20	21.1	1.042	0.946	0.75	375
67.5	25.5	0.84	1.20	1.13	10.0	1.048	1.052	0.77	315
0 ^c	8.2	1.10	1.35	1.13	0	n.p.	n.p.	n.p.	0
0 ^d	9.0	0.60	1.00	1.70	5.7	n.p.	0.970	0.88	185
Series OM10: Intimate mixtures: 90/10 wt.% OLV003/CHR103, and 67.5/22.5/10 wt.% OLV003/MET101/CHR103 (<45 μm CHR, 45–90 μm OLV and MET) HOSERLab ($i = 30^\circ$, $e = 0^\circ$)									
100	52.0	1.02	1.11	1.37	70.2	1.055	1.056	0.56	670
90	17.0	0.81	1.11	1.53	28.1	1.042	1.053	0.74	420
67.5	14.2	0.82	1.24	1.36	22.9	1.043	1.055	0.76	400
0 ^c	9.2	1.10	2.05	1.22	0	n.p.	n.p.	n.p.	0
0 ^d	9.0	0.60	1.00	1.70	5.7	n.p.	0.970	0.88	185
Series OM11: Intimate mixtures: <250 μm OLV003 + 50 nm Fe ⁰ (HOSERLab; $i = 30^\circ$, $e = 0^\circ$)									
100	65.0	1.02	1.03	1.30	56.4	1.055	1.055	0.56	660
99.9	57.5	1.03	1.03	1.27	52.1	1.058	1.058	0.56	630
99.5	33.8	1.05	1.04	1.15	51.4	1.059	1.060	0.56	615
99.0	27.0	1.07	1.01	1.03	32.7	1.059	1.060	0.55	550
98.0	15.4	1.08	1.12	1.01	22.5	1.040	1.062	0.56	590
95.0	11.8 ^f	1.06	0.92 ^f	0.91 ^f	18.8 ^f	1.070	1.06 ^f	n.p.	600 ^f
90.0	8.1 ^f	1.04	0.89 ^f	0.88 ^f	19.0 ^f	1.070	1.06 ^f	n.p.	600 ^f
80.0	5.8 ^f	1.04	0.90 ^f	0.84 ^f	16.0 ^f	1.080	1.05 ^f	n.p.	550 ^f
70.0	5.3 ^f	1.04	0.88 ^f	0.97 ^f	15.0 ^f	1.085	1.05 ^f	n.p.	485 ^f
0	3.5	1.22	1.25	1.03	8.0	0.840	0.860	0.59	340

Table 2 (continued)

Meteorite ^a	Reflectance at 0.56 μm (%)	Reflectance ratios			1 μm band depth (%)	Band minimum (μm)	Band center (μm)	0.7 μm position	FWHM ^e (nm)
		2.4/1.8 μm	1.8/0.56 μm	0.6/0.4 μm					
<i>Series OM12: Intimate mixtures: <45 μm OLV003 + 50 nm Fe^o (HOSERLab; i = 30°, e = 0°)</i>									
100	72.5	1.04	1.07	1.12	29.1	1.055	1.056	0.56	510
95.0	41.1	1.04	0.97	0.99 ^f	18.1	1.052	1.055	0.61	510
0	3.5	1.22	1.25	1.03	8.0	0.840	0.860	0.59	340
<i>Series OM13: Intimate mixtures: 45–90 μm OLV003 + 50 nm Fe^o (HOSERLab; i = 30°, e = 0°)</i>									
100	60.7	1.06	1.07	1.22	52.5	1.054	1.056	0.56	575
95.0	14.9	1.06	0.95	0.99 ^f	27.6	1.053	1.055	0.61	550
0	3.5	1.22	1.25	1.03	8.0	0.840	0.860	0.59	340
<i>Series OM14: Intimate mixtures: <250 μm OLV003 + 10 μm Fe^o (HOSERLab; i = 30°, e = 0°)</i>									
100	65.0	1.02	1.03	1.30	56.4	1.055	1.055	0.56	660
99.9	62.5	1.06	1.14	1.33	55.7	1.055	1.056	0.56	660
99.5	57.5	1.06	1.14	1.27	54.1	1.052	1.058	0.56	630
99.0	51.7	1.03	1.07	1.20	53.5	1.058	1.060	0.56	630
98.0	43.0	1.03	1.08	1.15	47.5	1.058	1.060	0.56	600
95.0	32.1	1.06	1.10	1.09	41.8	1.050	1.054	0.56	590
90.0	22.3	1.08	1.17	1.05	34.7	1.049	1.060	0.56	590
80.0	19.1	1.11	1.22	1.00	22.7	1.040	1.062	0.55	610
70.0	15.6	1.19	1.29	1.00	20.3	1.037	1.055	0.55	640
0	2.6	1.46	1.00	0.79	0	n.p.	n.p.	n.p.	n.p.
<i>Series OM15: Intimate mixtures: <45 μm OLV003 + 10 μm Fe^o (HOSERLab; i = 30°, e = 0°)</i>									
100	72.5	1.04	1.07	1.12	29.1	1.055	1.056	0.56	510
95.0	54.6	1.03	1.05	1.08	24.6	1.058	1.061	0.57	460
0	2.6	1.46	1.00	0.79	0	n.p.	n.p.	n.p.	n.p.
<i>Series OM16: Intimate mixtures: 45–90 μm OLV003 + 10 μm Fe^o (HOSERLab; i = 30°, e = 0°)</i>									
100	60.7	1.06	1.07	1.22	52.5	1.054	1.056	0.56	575
95.0	39.2	1.07	1.09	1.11	44.0	1.051	1.058	0.56	540
0	2.6	1.46	1.00	0.79	0	n.p.	n.p.	n.p.	n.p.
<i>Series OLI: Pure olivine (Fa_{9,6}), varying grain size (HOSERLab; i = 30°, e = 0°)</i>									
Grain size									
<45 μm	80.0	1.04	1.09	1.17	35.2	1.055	1.057	0.57	500
45–90 μm	54.8	1.08	1.39	1.28	55.2	1.055	1.057	0.68	570
90–250 μm	56.5	1.10	1.31	1.51	75.4	1.055	1.057	0.56	560
250–500 μm	43.0	1.06	1.39	1.74	85.1	1.055	1.062	0.56	800
500–1000 μm	27.4	1.06	1.61	1.94	88.0	1.055	1.060	0.56	820

Abbreviations: n.p.: not present.

Notes: MET030: Imilac pallasite slab; MET101: Odessa iron meteorite metal powder, <45 or 45–90 μm beaten in alumina mortar and pestle to create more equidimensional grains; MET101A: Odessa iron meteorite powder with no further treatment after grinding, sieving, and magnetic separation. Minerals: CHR103: chromite; OLV003: olivine (Fa_{9,6}); OLV007: olivine (Fa_{2,7}); OLV011: olivine (Fa_{99,9}); PYX117: low-calcium pyroxene (Fs_{24,6} Wo_{0,7}). Uncertainties (based largely on measurements of duplicate samples) are on the order of 2% for reflectance at 0.56 μm , 2% for band depths, 3 nm for band minima and centers, up to ~15 nm for 0.7 μm region peak positions (for samples with broad peaks), and 10 nm for FWHM.

^a Description and sources of meteoritic olivine spectra: Brachina (Fa₃₀): brachinite, <45 μm whole rock powder (RELAB data base); Brenham (Fa₁₂): pallasite, <30 μm (King and Ridley, 1987). Chassigny1 (Fa₃₂): chassignite Mars meteorite, <100 μm powder (RELAB data base); Chassigny2 (Fa₃₂): chassignite Mars meteorite, unsorted powder (RELAB data base); Chassigny3 (Fa₃₂): chassignite Mars meteorite, <150 μm powder (Gaffey, 1976); EET 99402 (Fa₃₆): brachinite, fine powder (Sunshine et al., 2007); Imilac (Fa_{12,6}): pallasite, <45 μm olivine separate (RELAB data base); NWA 753 (Fa₃₉): R chondrite, <125 μm (Sunshine et al., 2005); Rumuruti (Fa₃₉): R chondrite, <150 μm (Burbine, 2002); Thiel Mountain (Fa₁₅): pallasite, <74 μm olivine separate (Sunshine et al., 2007).

^b Pure olivine powder in a sample cup.

^c Pure metal (<45 μm).

^d Pure chromite (<45 μm).

^e Full width at half maximum of 1 μm region absorption band.

^f Spectrum is strongly blue-sloped (probably anomalously so), therefore best continuum position is uncertain and values are approximate.

strongly red, similar to or slightly redder than terrestrial olivines. They almost invariably exhibit the minor Fe^{2+} olivine-associated absorption bands in the 0.4–0.5 μm region.

Small deviations from “pure” olivine spectra, such as redder slopes and reduced band depths are likely due, in some cases, to the presence of accessory minerals, such as pyroxene and/or chromite, e.g., Brachina (Nehru et al., 1983) and Chassigny (Floran et al., 1978). The apparent absorption band in the Chassigny spectrum near 0.83 μm (Fig. 1d) is a spectral artifact. It is also possible that the redder 1.8/0.56 μm reflectance ratios in some of the meteorites may be due to small amounts of nanophase iron metal and/or sulfides, produced either as a result of impact shock dispersal of opaques or production of red-sloped nanophase opaques by space weathering, although the latter effect has not been documented in these olivine-rich meteorites. Some of the olivine-rich meteorite spectra or separates exhibit larger 0.6/0.4 μm reflectance ratios than clean terrestrial olivines. These redder slopes may be due to some combination of accessory phases, shock, and terrestrial weathering.

In addition to the spectra shown in Fig. 1d, at least some members of the olivine-bearing meteorites described in Table 1 show reflectance spectra dominated by olivine. These include CH chondrites (Cloutis et al., 2012e), CK chondrites (Cloutis et al., 2012d), CO chondrites (Johnson and Fanale, 1973; Gaffey, 1976; Cloutis et al., 2012c), CR chondrites (Cloutis et al., 2012a), CV chondrites (Johnson and Fanale, 1973; Gaffey, 1976; Cloutis et al., 2012b), ordinary chondrites (Gaffey, 1976), R chondrites (Berlin et al., 2003; Sunshine et al., 2005), angrites (Gaffey, 1976; Burbine et al., 2006; Cloutis et al., 2006b), brachinites (Sunshine et al., 2005), chassignites (Gaffey, 1976), lodranites (Hiroi and Takeda, 1991; Hiroi et al., 1993), olivine-diogenites (Cloutis et al., 2013), pallasites (Hiroi et al., 1992; Sunshine et al., 2005; this study), and ureilites (Gaffey, 1976; Cloutis et al., 2010b).

2.2. Meteoritic metal

Powdered meteoritic metal is red-sloped over the 0.3–2.5 μm interval with no strong absorption features. It can exhibit changes in slope near 0.6 and 1.3 μm (Cloutis et al., 2010a), due to changes in real and imaginary indices of refraction (Cahill et al., 2012), but is otherwise spectrally featureless (Cloutis et al., 2010a) (Fig. 1e). With decreasing grain size, meteoritic metal, as well as Fe and Ni, powders become darker and slightly less red (Hoffmann et al., 1991), at least for grain sizes in the few to few tens of μm range. Schreibersite and troilite, also present in pallasites (Buseck, 1977) are both red-sloped and dark, and schreibersite has a weak absorption band near 0.9 μm (Cloutis et al., 2010a). As with meteoritic metal, their spectral slopes are also grain size dependent.

3. Experimental procedure

The samples used to produce the various olivine + metal mixtures include a roughened slab of, and powder made from, the Odessa IAB coarse octahedrite (7.3 wt.% Ni), and a number of terrestrial olivines (OLV007: $\text{Fa}_{2.7}$; OLV003: $\text{Fa}_{9.6}$; OLV011: $\text{Fa}_{99.9}$). Olivine samples were ground by hand in an alumina mortar and pestle and dry sieved by gently brushing the ground samples in stainless steel or brass mesh sieves to facilitate the separation of fine from coarse grains. A sawn slab of Odessa was ground by hand with 60 grit garnet sandpaper to produce a powder that was separated from sandpaper grains by repeated passes of a hand magnet; the purity of the sample was assessed with a binocular microscope. Hand-grinding was used because previous experience had shown that mechanical high-speed grinding resulted in near-instantaneous formation of a bluish iridescent coating on the metal grains,

likely due to rapid oxidation promoted by the high temperatures inherent in mechanical grinding (Cloutis et al., 2010a). The metal powders were dry sieved as described above. The mineral mixtures were produced on a weight percent basis by weighing out the requisite end member powders with a balance accurate to ± 0.1 mg. Each mixture consisted of approximately 1 g in total, providing end member abundances accurate to $\sim \pm 0.01$ wt.%.

We also examined the effects of metal grain size on olivine + metal spectra to determine whether nanophase iron (npFe), generated by space weathering of olivine (e.g., Hiroi and Sasaki, 2001; Sasaki et al., 2001, 2002, 2003; Noguchi et al., 2011), would exhibit different spectral properties than our olivine + metal mixtures. Mixture of olivine and two different sizes of npFe (50 nm or 10 μm) were intimately mixed with olivine in varying proportions. All handling of the npFe samples and spectral measurements were conducted in a glove box which was purged with dry, pure nitrogen. The reflectance spectra were measured using the same procedures as for the other mixtures.

As a complement to the mixture spectra, we measured point spectra on roughened saw-cut slabs of the Imilac (MET030) and Springwater pallasites (Table 2). Imilac consists of ~ 30 vol.% metal (9.6–11.3% Ni; Mason, 1963; Scott, 1977) and ~ 70 vol.% olivine ($\text{Fa}_{12.6}$; Mason, 1963), while Springwater consists of ~ 47 wt.% each of olivine and metal and ~ 6 wt.% phosphates (Buseck, 1977). Olivine grains in our Imilac slab range up to 7 mm in diameter and exhibit small but variable amounts of iron oxyhydroxide staining along fractures. The slabs were roughened with 120 grit garnet sandpaper prior to the spectral measurements. We measured point spectra (~ 5 mm in diameter) on spots that included nearly pure metal, olivine, and phosphates.

We also measured reflectance spectra of < 45 μm powders of OLV003 sprinkled on a slab of the Odessa iron meteorite roughened with 120 grit sandpaper. The olivine was brushed through a 90 μm size sieve to produce relatively uniform coatings. Different amounts of olivine were sprinkled onto the slab; we did not quantify thicknesses, but noted that coating thicknesses, visually, ranged from light coatings where the underlying slab was partially visible, to heavy coatings which completely obscured the underlying metal. Our intent was to simulate surfaces where the metal may be largely intact but any mafic silicates have been comminuted by impacts. This type of assemblage may exist on asteroids whose temperatures are such that metal will be in the ductile failure regime and mafic silicates in the brittle failure regime (e.g., Zukas, 1969; Auten, 1973; Marcus and Hackett, 1974; Remo and Johnson, 1975; Matsui and Schultz, 1984).

Reflectance spectra (~ 0.35 –2.5 μm) were measured at both the NASA-supported RELAB spectrometer facility at Brown University (Pieters, 1983), and the University of Winnipeg HOSERLab (Cloutis et al., 2006a). Spectra measured at RELAB were acquired at $i = 0^\circ$ and $e = 15^\circ$ (series OM1 and OM2 in Table 2) with 5 nm spectral sampling. They were measured relative to halon and corrected for dark current and minor offsets in halon's reflectance in the 2.0–2.5 μm region. Spectra measured at HOSERLab (remaining series in Table 2) were acquired at $i = 30^\circ$ and $e = 0^\circ$ with an ASD Field-Spec Pro HR spectrometer. They were measured relative to a calibrated Spectralon[®] disc and also corrected for dark current and minor offsets in Spectralon's[®] reflectance in the 2.0–2.5 μm region. The ASD data were corrected for occasional small detector offsets at 1.00 and 1.83 μm . The ASD spectrometer has a spectral resolution of between 2 nm (in the visible region) and 7 nm (in the near infrared), with a sampling interval of 1.4 nm. The data are internally interpolated by the instrument to provide output at 1 nm intervals. These data were supplemented with reflectance spectra of olivine-rich meteorites from the RELAB public database.

Spectral parameters that were extracted from the data include band minima, band centers, band depths, slopes (as reflectance

ratios), and band widths. Absorption band minima were determined in two ways: (1) by fitting a third-order polynomial to ~10–20 data points on either side of the visually determined minimum; and (2) by constructing a series of chords across the absorption band at various points and averaging their midpoints or projecting the midpoints of progressively shorter chords to the band minimum (in the case where the chords showed a progressive change in position). The reported values are the mean of the two methods.

For determination of band centers and band depths, the 1 μm region absorption feature was isolated by fitting a straight line continuum such that it was tangent to the spectrum on either side of this feature. Band centers were determined in the same two ways as for band minima using the continuum-removed spectra. Band depths were calculated using Eq. [32] of Clark and Roush (1984): $Db = (Rc - Rb)/Rc$, where Db is band depth, Rc is reflectance of the continuum at the band center, and Rb is the reflectance at the band center. Overall slope was measured as the ratio of the reflectance at 1.8 μm to that at 0.56 μm . These wavelengths were chosen to span as wide a wavelength range as possible and to largely fall outside the major absorption bands of both olivine and pyroxene. Samples included in this study are described in Table 2.

Our analysis included a reexamination of existing reflectance spectra for a number of previously identified olivine \pm metal-rich asteroids. We measured the same spectral metrics for the asteroids as we did for the laboratory spectra. As the asteroids are present at different heliocentric distances, we needed to account for how temperature differences between the asteroids and laboratory spectra may affect the interpretation of spectral metrics. It has been found that temperature variations have a small effect on band depth (on the order of 1–2% over a range of 300 K (Lucey et al., 1998)), and band position (Singer and Roush, 1985). This is on the order of the observational uncertainties, and hence we did not apply corrections to band depths and wavelength positions for the asteroid spectra. Temperature has its greatest effect on band widths (Lucey et al., 1998). We used the full width at half maximum (FWHM) as a measure of band width. FWHM is the horizontal width of an absorption feature measured at the reflectance midpoint between the band center and the continuum. We measured FWHM for asteroid spectra and applied a simple correction to the FWHM of asteroid spectra using the approach of Burbine et al. (2009) to determine FWHM at 300 K. We used the average heliocentric distance of each asteroid (semi-major axis), and an emissivity factor of 0.9 (Burbine et al., 2009).

4. Olivine + metal laboratory spectra

As described in Table 2, olivine + metal intimate and areal mixtures were generated using multiple types and grain sizes of end members. The various series allow us to examine spectral changes associated with varying metal/olivine ratios, areal versus intimate mixtures, varying grain size of one or both end members, olivine composition, and the presence of chromite. These mixtures were supplemented with spectra of powdered olivine sprinkled on an iron meteorite slab, and point spectra measured on pallasite slabs.

4.1. End member variation effects in powdered mixtures

Series OM1 (Table 2) involves 45–90 μm size metal + olivine intimate mixtures generated at 25 wt.% intervals. Increasing metal content causes a decrease in overall reflectance and band depth (Fig. 2a and b). The spectra also become increasingly red-sloped and the band minimum moves to shorter wavelengths; at 75 wt.% metal, the olivine band is barely visible. Band centers are recoverable to ± 2 nm with the exception of the 25/75 olivine/metal

mixture; in this case the band center is underestimated (1.037 versus 1.057 μm expected for pure olivine). The visible region slope, as measured by the 0.6/0.4 μm reflectance ratio does not vary systematically. With increasing metal content, FWHM decreases, and the 0.7 μm region peak moves to longer wavelengths.

Series OM4 (Table 2) is a more comprehensive mixture series, involving <45 μm size fractions, and 10 wt.% intervals. As with series OM1, increasing metal content leads to a generally systematic decrease in reflectance (Fig. 2c and d), although the 30 and 20 wt.% olivine mixtures show some overlap. The pure metal spectrum is, at some point, brighter than the mixtures containing <40 wt.% olivine, and is entirely brighter than the 10 wt.% olivine mixture. The normalized spectra become increasingly red-sloped with increasing metal content, the olivine absorption band becomes shallower and narrower, and its minimum moves to shorter wavelengths (Fig. 2e and f). The olivine band is barely apparent at 10 wt.% olivine. The movement of the band minimum to shorter wavelengths accelerates at >60 wt.% metal (Table 2). Band centers vary by ≤ 6 nm with the exception of the 10/90 olivine/metal mixture, whose center is underestimated (Table 2). With increasing metal content, the 0.7 μm region olivine peak becomes increasingly broad, and the reflectance dropoff below ~ 0.56 μm becomes shallower. Appreciable reddening of the spectra begins around 60 wt.% metal. Olivine band depth is greatly reduced by the addition of metal: it decreases to 50% of its starting values with the addition of ~ 30 wt.% metal for the 45–90 μm size mixtures and ~ 15 wt.% metal for the <45 μm mixtures (Table 2).

4.2. Grain size effects in powders

Fig. 3a and b shows how varying grain size can affect 50/50 metal/olivine spectra (series OM1 and OM2: Table 2). The pure <45 μm olivine is brighter but has a shallower absorption band than the 45–90 μm fraction, and the finer-grained metal is slightly darker and less red-sloped than the coarser metal. For the 50/50 mixtures, the finer-grained sample spectrum is less red-sloped and substantially brighter than the coarser-grained sample spectrum, but band depths are similar (12.1% versus 13.8%: Table 2). FWHM is smaller for the coarser versus the finer 50/50 mixture and also shows a greater decrease relative to the pure olivine.

The 50/50 mixtures in series OM3 and OM4 (Fig. 3c and d, Table 2), are more similar to each other than the comparable OM1–OM2 spectra (for these mixtures we used unbeaten metal powders, so metal grain texture may be having an effect). The 50/50 finer grain size absorption band is much shallower than the equivalent coarser-grained sample (6.0% versus 18.3%) and less red. Decreases in FWHM are similar (35% versus 27% decrease for the 50/50 mixtures relative to the pure olivine).

We also measured reflectance spectra of saw-cut fines from Springwater, which were retained when it was dry cut with a diamond wire saw. The fines should consist of an approximately 50:50 wt.% mixture of olivine based on petrographic analysis (Buseck, 1977) and visual inspection of the slab; the ~ 6 wt.% phosphates that are present in Springwater (Buseck, 1977) were not detected in our sample by XRD: we detected only olivine and metal. The saw-cut fines are extremely fine-grained (<20 μm), resulting in a very clumpy powder.

Powders were prepared for spectral measurements in two ways: (1) pouring them into an aluminum sample cup and drawing a glass slide across the powder surface, and (2) gently pressing the poured powder into the cup with the face of a glass slide. Because the powder was very fine-grained, the first method resulted in a very irregular surface with many divots and grooves. The spectra of these samples have 0.56 μm reflectance of ~ 15 –16%, and are slightly red-sloped, with 2.5/0.8 μm ratios of ~ 1.1 (Fig. 3e). By contrast, the samples with smooth surfaces are brighter, with 0.56 μm

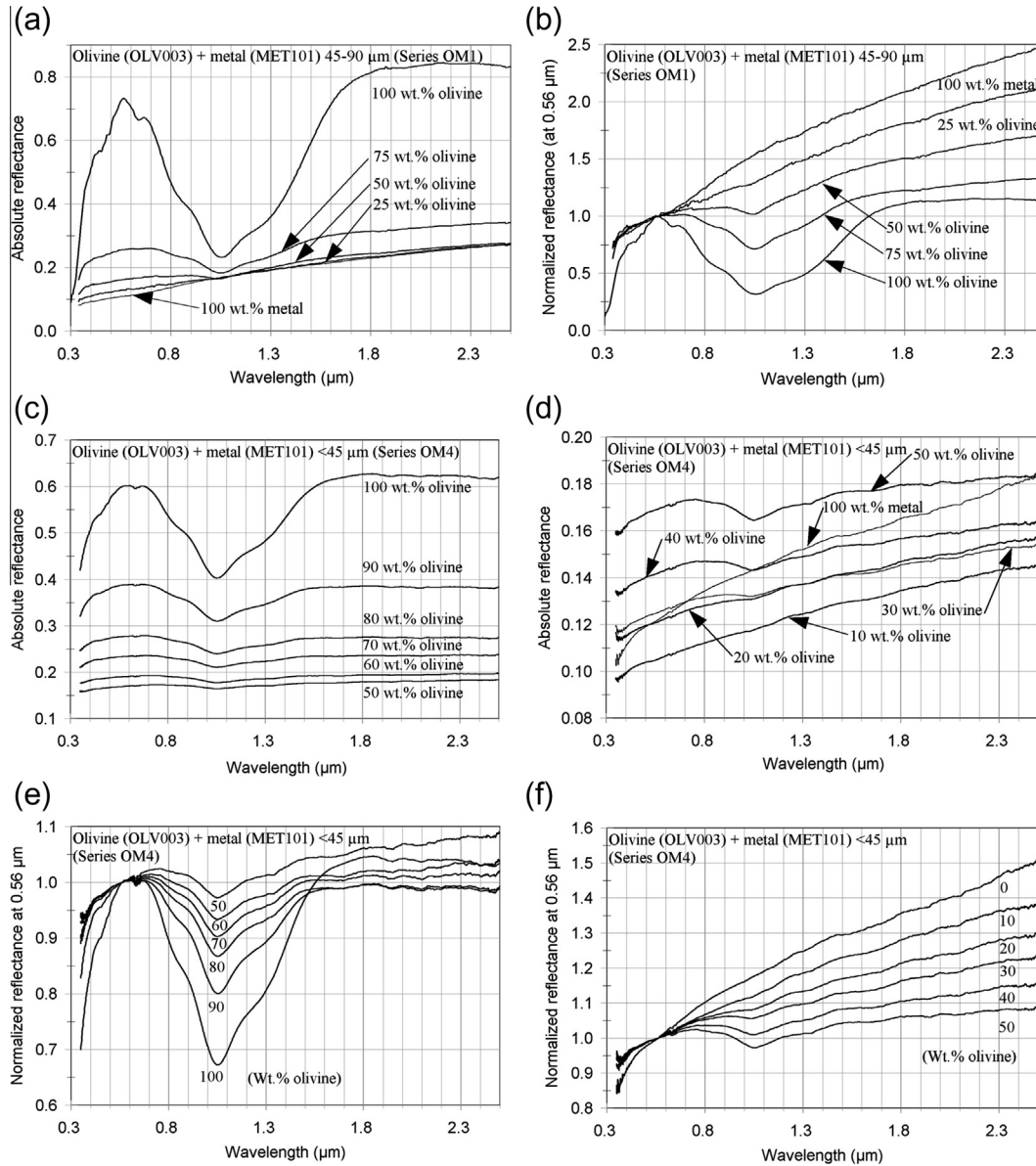


Fig. 2. Reflectance spectra of olivine + metal series. (a) 45–90 μm size 25 wt.% interval intimate mixture series (series OM1 in Table 2). (b) Same as (a) normalized at 0.56 μm . (c) <45 μm size 10 wt.% interval intimate mixture series (series OM4 in Table 2) from 100 to 50 wt.% olivine. (d) Same as (c) for olivine abundances from 50 to 0 wt.%. (e) Same as (c) normalized at 0.56 μm . (f) Same as (d) normalized at 0.56 μm .

reflectance of 19–20%, and somewhat redder. The reason for these differences is likely due to greater shadowing for the rough surface spectra. These results indicate that surface texture variations, even at small phase angles (30°) can affect overall reflectance and spectral slope. These spectra show little or no evidence for the 0.4–0.7 μm minor olivine absorption bands.

4.3. Olivine compositional effects

Spectra of 50/50 olivine/metal of similar grain sizes (<45 μm), involving three compositionally different olivines were also measured (series OM4, OM5, and OM6: Table 2; Fig. 4). Olivine composition affects the spectra in a number of ways. The 50/50 mixture with the most Fe-poor olivine has the highest overall reflectance, and the smallest band depth and FWHM. In all three cases, the mixture spectra have smaller band depths than the corresponding pure olivines. More metal is required to suppress olivine

absorption bands as the olivine becomes more Fa-rich; band depth is most reduced (as a percentage of the pure end member olivine band depth) for the lowest Fa olivine and least for the highest Fa olivine (Table 2). Interestingly, the most fayalitic olivine (OLV011; Fa_{99.9}) shows no appreciable decrease in FWHM at 50 wt.% metal (Table 2).

4.4. Areal versus intimate mixtures

We compared intimate to areal mixtures (series OM3, OM3A, OM4, and OM4A: Table 2). Areal 50/50 mixtures (a mathematical average of the two end members) versus 50/50 intimate mixtures clearly show that metal has a larger influence on the intimate mixtures, with overall reflectance of an intimate mixture being much closer to that of metal than a comparable areal mixture (Fig. 5a and b). Intimate mixture spectra have a much shallower olivine absorption feature than comparable areal mixture spectra (Table 2).

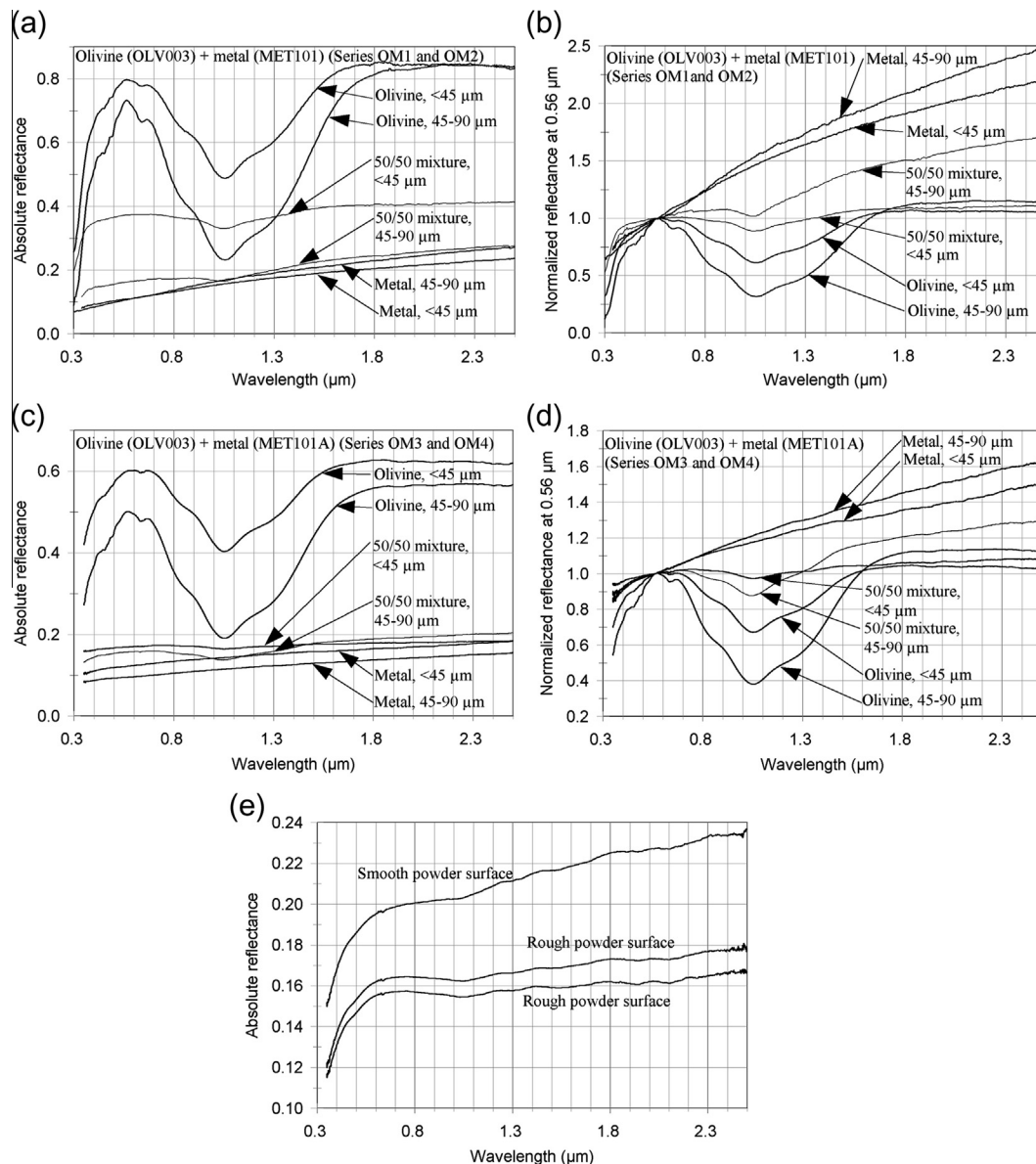


Fig. 3. Reflectance spectra of olivine + metal series. (a) 50/50 wt.% olivine/metal intimate mixtures and end members for two different grain sizes (series OM1 and OM2 in Table 2). (b) Same as (a) normalized at 0.56 μm . (c) 50/50 wt.% olivine/metal intimate mixtures and end members for two different grain sizes (series OM3 and OM4 in Table 2). (d) Same as (c) normalized at 0.56 μm . (e) Reflectance spectra of saw-cut fines from the Springwater pallasite. The lower two spectra are for samples with rough surfaces. The upper spectrum is an average of 5 individual spectra for a smooth surface; the individual spectra vary in absolute reflectance by <2%.

Reducing the pure olivine band depth by 50% requires \sim 15% metal versus \sim 80% metal for the <45 μm size intimate and areal mixtures, respectively (Table 2). Both types of mixtures show the band minimum moving to shorter wavelengths, and band depth and FWHM decreasing with increasing metal content (Table 2). These general trends apply to both <45 and 45–90 μm powders. All spectral changes associated with increasing amounts of metal proceed more rapidly in the intimate mixtures.

4.5. Olivine on a metal slab

Fine-grained (<45 μm) olivine was sprinkled on a roughened slab of the Odessa iron meteorite to assess the spectral properties of such an assemblage (series OM7: Table 2), which could plausibly exist for an asteroid where impacts may fracture olivine (brittle failure) while leaving metal largely intact (ductile deformation). With the exception of the lightest olivine coating, increasing olivine coverage results in less red-sloped and brighter spectra, and

an increasingly deep 1 μm olivine absorption band; FWHM is variable (Fig. 6).

4.6. Pallasite slab spectra

4.6.1. Imilac pallasite slab spectra

Spot spectra of pallasite slabs were measured after roughening their surfaces. The intent was to examine how a largely intact olivine + metal assemblage may appear spectrally. The Imilac spot spectra sampled regions with different coverage by olivine and metal (series OM8: Table 2). The spectra (Fig. 7a) show wide variations in brightness and slopes. A notable feature is that the presence of large (many mm diameter) olivine grains results in a broad absorption feature in the 1 μm region. The absorption bands for the most olivine-rich spots show a minimum near 1.3 μm , close to the position of the longest wavelength Fe^{2+} M1 olivine band, which is also the strongest olivine absorption band according to Sunshine and Pieters (1998). This is consistent with how olivine powder

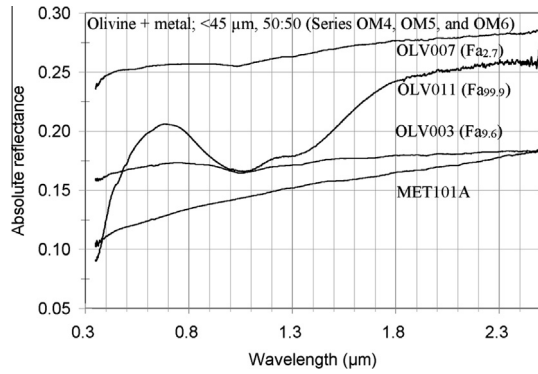


Fig. 4. Reflectance spectra of 50/50 wt.% intimate mixtures of <45 μm olivine and metal, and pure metal, for three compositionally different olivines (Fa contents indicated on the figure; series OM4, OM5, and OM6 in Table 2).

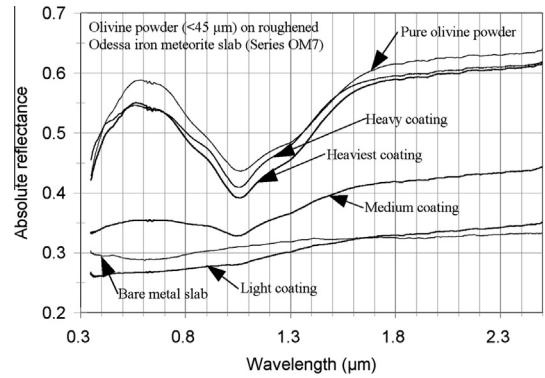


Fig. 6. <45 μm olivine powder sprinkled on a roughened slab of the Odessa iron meteorite (series OM7 in Table 2).

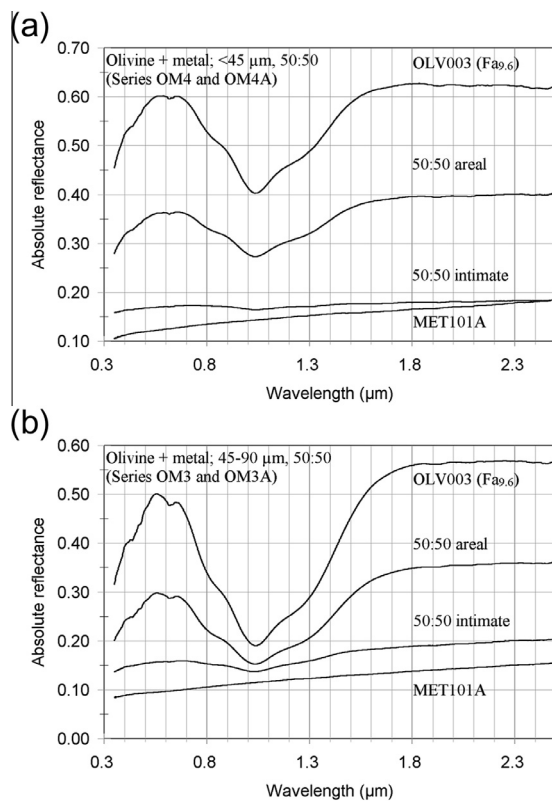


Fig. 5. (a) 50/50 wt.% areal and intimate spectra, and end members, for <45 μm size samples (series OM4 and OM4A in Table 2). (b) 50/50 wt.% areal and intimate mixture spectra, and end members for 45–90 μm size samples (series OM3 and OM3A in Table 2).

spectra vary with grain size (Craig et al., 2007; Clénet et al., 2011; Buz and Ehlmann, 2014), and with absorption band saturation (Pompilio et al., 2009). FWHM is also higher in the slab spectra than in any of the powders, regardless of Fa content. The shallow downturn in reflectance beyond ~2.2 μm and the weak absorption bands near 2.3 and 2.45 μm in the two olivine-rich spectra are due to the lacquer applied to samples to minimize oxidation, which could not be fully removed during sample preparation.

Hiroi et al. (1992) measured reflectance spectra of two pallasites chips, including both rough and smooth surfaces in both specular and diffuse mode (series OM8R1 and OM8R2: Table 2). They found that specular reflectance is much higher than diffuse reflectance, and specular spectra are red-sloped and featureless. Their

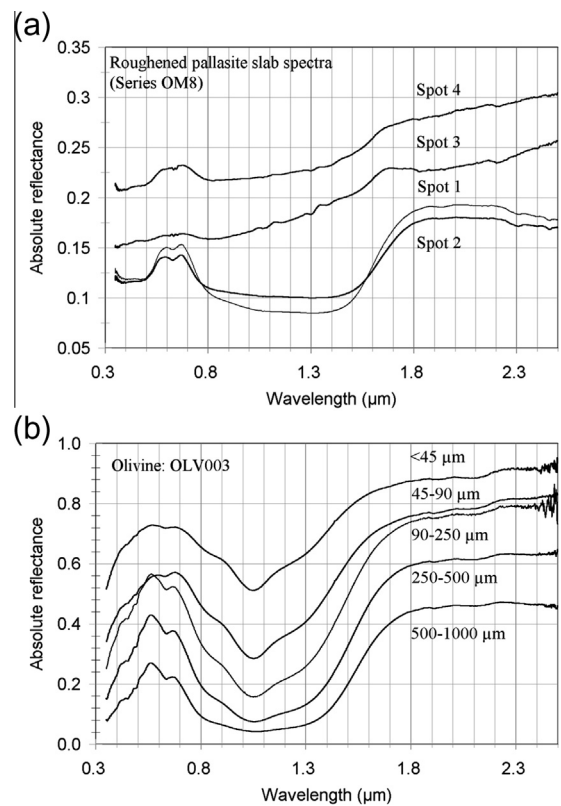


Fig. 7. (a) Spot spectra of a roughened slab of the Imilac pallasite (series OM8 in Table 2). (b) Pure olivine spectra as a function of grain size (series OL1 in Table 2).

diffuse non-specular spectra of rough versus smooth surfaces show little variability. In all cases, their spectra are dominated by olivine, have low reflectance (<20% at 0.56 μm), and exhibit a broad olivine band. Band minima are located near 1.05 μm, although reflectance is also low near 1.3 μm as expected for a saturated olivine absorption feature. The similarities between pallasite slab spectra, acquired largely over olivine grains and pure large olivine powder spectra can be seen by comparing the pallasite slab spectra (Fig. 7a) to large olivine powders (Fig. 7b; series OL1: Table 2).

4.6.2. Springwater pallasite slab spectra

As with Imilac, reflectance spectra were shot on a number of spots on the Springwater pallasite slab, including metal-rich, olivine-rich (of olivines both within and outside the phosphate-bearing enclave) and phosphate-rich spots. Spectra were acquired on

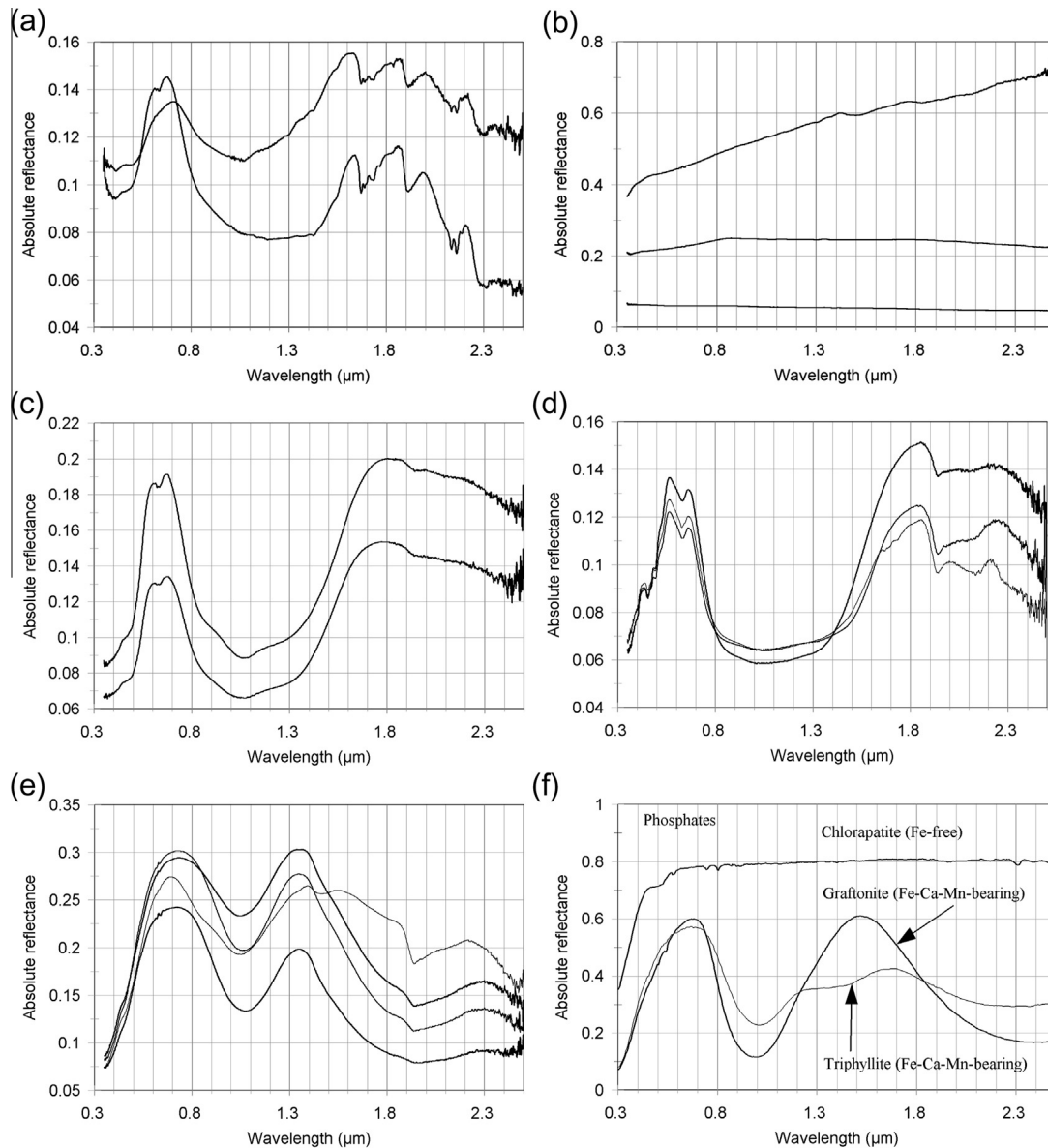


Fig. 8. Reflectance spectra of selected spots on a slab of the Springwater pallasite. (a) Spots on an epoxy-coated face acquired after attempting to remove the epoxy by sanding. Epoxy-related absorption bands are most evident in the $>1.65 \mu\text{m}$ region; both spectra are for olivine-rich spots. (b) Three metal-rich spots on epoxy-free face. (c) Iron oxyhydroxide-stained olivines outside a phosphate-rich enclave. (d) Unstained olivines inside a phosphate-rich enclave. (e) Phosphate-rich regions within a phosphate enclave. (f) Reflectance spectra (measured at RELAB) of various phosphates: chlorapatite (Fe-free), and graffonite and triphyllite (both are Fe^{2+} -Ca-Mn-bearing).

epoxy-covered and epoxy-free faces. Spectra of the epoxy-coated face were acquired after attempting to remove the epoxy by sanding. The reflectance spectra of this face still show clear evidence of the epoxy, in the form of organic-associated absorption bands in the $1.6\text{--}2.5 \mu\text{m}$ region (Fig. 8a). Reflectance spectra of the opposite face are largely free of any spectral signature of epoxy. Metal-rich area spectra show the expected variation in spectral slopes associated with metallic slabs (Britt and Pieters, 1988) and are otherwise largely featureless (Fig. 8b).

Reflectance spectra of olivine-rich areas on the epoxy-free face included olivines enclosed in the phosphate-rich enclave and outside of it. Interestingly, the olivines within the phosphate-rich enclave showed no visual evidence of iron oxyhydroxide staining, while those outside this region showed variable amounts of red staining. Spectra of the red-stained olivines (Fig. 8c) exhibit a deep $1 \mu\text{m}$ region absorption band, as well as a steep dropoff in reflectance below $\sim 0.58 \mu\text{m}$, which is characteristic of iron oxyhydroxides (Sherman and Waite, 1985). The reflectance spectra

of olivine-rich spots in the phosphate-bearing enclave (Fig. 8d) also show the broad $1 \mu\text{m}$ region olivine absorption band, but rather than a steep dropoff in the visible region toward shorter wavelengths, exhibit expected olivine-associated absorption bands in the $0.4\text{--}0.5 \mu\text{m}$ region (King and Ridley, 1987). They also all exhibit a complex absorption feature beyond $1.87 \mu\text{m}$ that is likely due to contributions from adjacent phosphates (discussed below).

A number of point spectra were acquired on phosphate-rich spots on the slab. The spectra of the phosphates are distinct from the other components in the meteorite. These spot spectra exhibit a number of absorption bands (Fig. 8e). These include two broad bands centered near 1.07 and $1.98 \mu\text{m}$, a possible band longward of $\sim 2.3 \mu\text{m}$, and a sharper band near $1.93 \mu\text{m}$. The bands near 1.07 , 1.98 and $\sim 2.3 \mu\text{m}$ are attributable to octahedrally-coordinated Fe^{2+} (Lane et al., 2007), and are consistent with the allowed substitution of Fe^{2+} for Mg in the various phosphates that are present in Springwater (DuFresne and Roy, 1961; Buseck and

Holdsworth, 1977): farringtonite ($\text{Mg}_3(\text{PO}_4)_2$), stanfieldite ($\text{Ca}_7\text{Ca}_2\text{Mg}_9(\text{PO}_4)_{12}$) or $\text{Ca}_4(\text{Mg}, \text{Fe}^{2+}, \text{Mn})_5(\text{PO}_4)_6$, merrillite ($\text{Ca}_9\text{NaMg}(\text{PO}_4)_7$), and whitlockite ($\text{Ca}_9(\text{Mg}, \text{Fe}^{2+})(\text{PO}_4)_6(\text{PO}_3\text{OH})$) (Buseck, 1977; Buseck and Holdsworth, 1977; Fowler-Gerace et al., 2013). The fact that the 1 and 1.93 μm region absorption features show some variation in their position and intensity suggests that multiple types of phosphates are likely present. The 1.93 μm feature is sharper than would be expected for adsorbed water, and is most consistent with a hydrated phosphate such as whitlockite. Similar spectral variability is seen in different Fe^{2+} -bearing phosphates (Fig. 8f). Fe^{2+} accounts for the bands in the 1 and 2.3 μm regions; Mn likely accounts for the band near 1.4 μm ; Fe-free phosphates (e.g., chlorapatite) do not show significant absorption bands. The phosphates shown in Fig. 8f are H_2O -free, consequently they do not show an absorption feature in the 1.9 μm region. H_2O -bearing phosphates do show an absorption band in this region (Lane et al., 2007). The presence of weak features beyond 1.65 μm in a few of the spectra collected on the epoxy-free face is likely due to a minor contribution from the epoxy, which is expected to seep into any cracks in the sample, and hence make a minor contribution to some of the reflectance spectra.

4.7. Effects of chromite

Chromite is a common accessory phase in olivine-rich lithologies (e.g., Evans and Frost, 1975; Irvine, 1975; Evans, 1980; Eckstrand, 1984). In meteorites, chromite is often the most common and abundant spinel-group mineral, usually present at the one to few percent level in brachinites (Prinz et al., 1986), pallasites (Buseck, 1977; Boesenberg et al., 1995), and chassignites (Mason et al., 1975; Floran et al., 1978; Smith et al., 1984). Two meteorites are notable for their chromite contents. EET 84302,

provisionally classified as an acapulcoite, contains 23 vol.% heterogeneously distributed chromite (Takeda et al., 1993; Yugami et al., 1996). LEW 88774 has been classified as a Cr-rich ureilite and contains 6 vol.% chromite (Mikouchi et al., 1995; Chikami et al., 1997). However, it should be noted that pyroxene is much more abundant than olivine in these two meteorites, and hence will dominate their spectra (Cloutis et al., 1986).

We measured two sets of intimate mixtures involving olivine + chromite \pm metal (series OM9 and OM10, Table 2). The addition of <45 μm chromite to <45 μm olivine (Fig. 9a) has a number of effects. It lowers reflectance, reduces 1 μm region band depth, broadens the visible region peak and shifts it to longer wavelengths, reddens the 0.7–1.5 μm interval, and also introduces an intense broad absorption band near 2.25 μm . The addition of metal further reduces reflectance, shifts the visible peak to even longer wavelengths, and reduces the 2.25 μm region chromite band depth. When the chromite is finer-grained than the olivine and metal (Fig. 9b), reflectance is lowered more by the addition of chromite, while the other spectral changes are similar. In both cases, the addition of chromite decreases the 1 μm region olivine band FWHM.

5. Discussion

The various olivine + metal mixture spectra allow us to examine whether and how different types of assemblages can be discriminated. We can use various spectral metrics in this regard. The trends exhibited by the various olivine/metal series are tabulated in Table 3. The major trends that we found and that enable the construction of spectral metrics for characterizing olivine + metal assemblages, include:

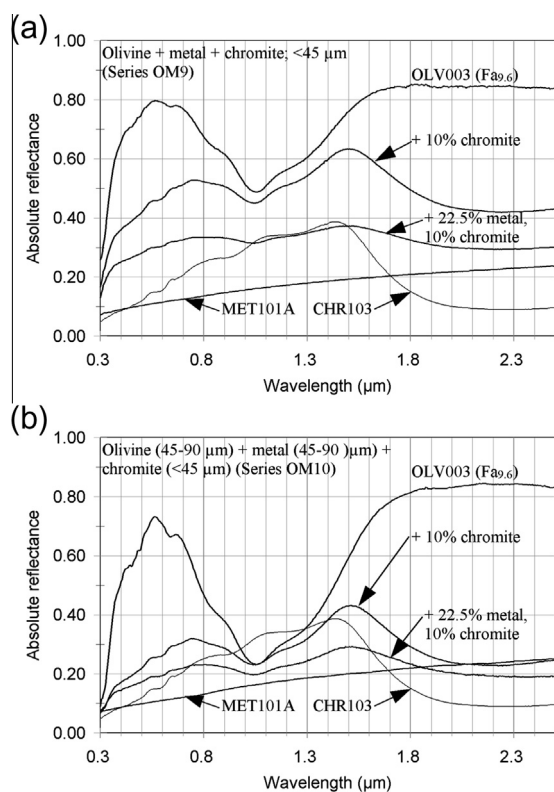


Fig. 9. (a) 90/10 wt.% olivine/chromite and 67.5/22.5/10 wt.% olivine/metal/chromite intimate mixtures and end member spectra (<45 μm grain size; series OM9 in Table 2). (b) Same as (a) but for 45–90 μm size olivine and metal (series OM10 in Table 2).

- Reflectance at 0.56 μm . It increases with increasing olivine abundance in powdered intimate mixtures and on a metal slab. It decreases with increasing olivine grain size, olivine Fa content, addition of chromite, and increasing spectral reddening that simulates the presence of npFe (Sasaki et al., 2001).
- The 1.8/0.56 μm reflectance ratio, used as a measure of overall spectral slope. It decreases with increasing olivine abundance in powdered mixtures and on a metal slab, and with increasing chromite content. It increases with increasing grain size and spectral reddening (Sasaki et al., 2001); it is largely insensitive to olivine composition.
- The 0.6/0.4 μm reflectance ratio, used as a measure of visible region slope. It shows complex behavior with olivine abundance, and increases with olivine Fa content and grain size, and addition of chromite.
- The 1 μm region absorption band minimum position. It increases with increasing olivine abundance and olivine Fa content, and may increase slightly with increasing olivine grain size. It decreases with the addition of chromite.
- The 1 μm region absorption band center position. It is largely insensitive to metal abundances <80%, grain size, and spectral reddening (Sasaki et al., 2001). It increases with increasing olivine Fa content at grain sizes larger than that required to saturate the 1.05 μm region band, and decreases with increasing chromite abundance.
- The 1 μm region absorption band depth. It increases with increasing olivine abundance, grain size, and Fa content, and decreases with the addition of chromite. It is largely insensitive to spectral reddening (Sasaki et al., 2001).
- The visible region peak position. It generally decreases with increasing olivine abundance, olivine Fa content, and spectral reddening (Sasaki et al., 2001). It increases with increasing chromite content.

Table 3
Change in spectral parameters for olivine + metal assemblages.

Metric	Intimate olv + metal: increasing olivine	Areal olv + metal: increasing olivine	Increasing olivine grain size ^a	Increasing olivine Fa content	Increasing olivine on metal slab	Pallasite slab versus powder	Addition of chromite
Reflectance at 0.56 μm	Increases rapidly above ~80% olivine	Increases linearly	Decreases	Decreases	Increases	Less than powders	Decreases
1.8/0.56 μm reflectance ratio	Decreases	Decreases	Increases	Variable	Decreases	Overlap	Increases
0.6/0.4 μm reflectance ratio	Decreases then increases	Decreases then increases	Increases	Increases	Increases	Overlap	Increases
1 μm band minimum position	Increases	Increases	Increases slightly	Increases	Increases	Highly variable	Decreases
1 μm band center position	Increases up to ~20% metal, then constant	Constant	Constant	Increases	Variable	Highly variable	Decreases
Band depth near 1 μm	Increases	Increases	Increases	Increases	Increases	Variable	Decreases
Visible region peak position	Decreases	Decreases	Variable	Decreases	Increases	Variable	Increases
Full width at half maximum	Increases	Increases	Increases	Increases	Variable	Greater than powders	Decreases

^a For <45 versus 45–90 μm size olivine and metal. olv: olivine.

- FWHM. It increases with increasing olivine abundance (much more rapidly in intimate versus areal mixtures), increasing grain size, and olivine Fa content, and is largest for pallasite slab spectra; its behavior for olivine sprinkled on metal is not systematic. It decreases with increasing chromite content.

These variable trends can be understood on the basis of the spectral properties of the end members. Olivine powder reflectance is higher than metal at all wavelengths for all but the largest grain sizes, and is less red-sloped as measured by the 1.8/0.56 μm reflectance ratio. This accounts for the decreases in absolute reflectance and increases in slope with increasing metal content. The lack of an absorption band in metal in the 1 μm region accounts for the decrease in band depth and FWHM with increasing metal abundance. The red slope of metal accounts for the shifts in band minima toward shorter wavelengths with increasing metal content. With increasing Fa content, olivine becomes darker and the 1 μm region absorption band becomes deeper and wider and moves to longer wavelengths, accounting for the trends seen as a function of olivine Fa content. With increasing grain size, up to the point of saturation, olivine becomes darker and the 1 μm region absorption band becomes deeper, accounting for the spectral trends seen for these parameters.

We can construct spectral metrics for discrimination of various olivine + metal assemblage properties using these observed spectral variations. We have focused this effort on spectral properties that are most readily obtainable and least subject to interference by other phases. We found that some parameters are more useful than others for deriving specific assemblage properties. Band center position is most useful for deriving olivine composition; spectral slope, band minimum, and 0.7 μm peak position are most useful for determining metal abundance; band depth, FWHM, and absolute reflectance are more complex functions of olivine abundance, olivine composition, and grain size. Reflectance at 1.8 μm and FWHM are largely insensitive to spectral reddening by npFe as discussed below, as are band depth and band center position.

For fine-grained olivine + metal mixtures, the addition of metal initially leads to large reductions in band depth, reflectance and FWHM, little change in band minimum or center or overall slope, and a flattening of slope in the visible region. As metal content increases above ~50 wt.%, further reductions in FWHM and band depth are seen, reflectance decreases more slowly or may actually increase, band minima move to progressively shorter wavelengths, band centers may move to shorter wavelengths, the 0.7 μm region peak moves to longer wavelengths, and overall slope and visible region slope start to increase.

Analysis of olivine + metal spectra to derive as unique an identification as possible is, and should be, a multi-step process. By relying on multiple spectral parameters, the robustness of the derived assemblage properties increases. The lack of significant movement in band center (< ± 3 nm) with the addition of metal up to ~75% is the best indicator of olivine Fa content as it is unaffected by grain size (King and Ridley, 1987), and provided that the olivine absorption band is not saturated or affected by other phases with absorption features in this region, such as pyroxene (Cloutis et al., 1986). The presence of pyroxene can be recognized by the appearance of an additional absorption band in the 2 μm region. More sophisticated techniques are also available to determine whether a 1 μm region absorption band is saturated (Pompilio et al., 2009).

By beginning analysis of olivine + metal assemblages using band center as an initial discriminator, many of the spectral “interferences” and overlaps in spectral parameters that occur between the different samples included in this study can be minimized. Because olivine band center varies by only a few tens of

nanometers as a function of Fa content, we decided to aggregate olivine by Fa content into three groups: low (Fa_{~1}–Fa_{~33}), medium (Fa_{~34}–Fa_{~67}), and high (Fa_{~68}–Fa₁₀₀). These ranges correspond to band centers of ~1.048–1.064 μm (low Fa), 1.065–1.081 μm (medium Fa), and 1.082–1.098 μm (high Fa). Band centers outside this range indicate very abundant metal and/or the presence of pyroxene (band center <1.048 μm), or large (spectrally saturated) olivine (band center >1.098 μm).

To determine whether metal content is high enough to lead to an erroneous (too low in wavelength) band center position, the position of the band minimum appears to be a reliable indicator of that. If band minimum is <~1.03 μm , then the derived band center has a high probability of being too low. A band minimum longward of ~1.1 μm and FWHM > ~580 nm could be indicative of a solid, regolith-free surface, by analogy with our pallasite slab spectra.

5.1. Spectral metrics

Our initial analysis is focused on fine-grained <45 μm intimate assemblages, as we have the most spectral data for them. We include coarser assemblages, slabs, and olivine on metal where appropriate. Of the various available spectral parameters, each is sensitive to different assemblage properties.

To aid in spectral analysis, the first step is to determine band center for an unknown assemblage and assign it to the low (1.048–1.064 μm), medium (1.065–1.081 μm), or high (1.082–1.098 μm) Fa group. This assists in application of subsequent metrics as they vary in different ways depending on Fa content. We have found that the depth of the olivine band in the 1 μm region is best suited for constraining olivine abundance, as it is largely insensitive to spectral reddening (Sasaki et al., 2001). We find that band depth increases with increasing Fa content for a constant grain size and decreases with increasing metal content. After determining band center position and depth, additional spectral metrics can be applied. Larger grain sizes or intact slabs will lead to larger uncertainties in olivine/metal abundances. In some cases, spectral metrics for such assemblages will plot outside the fine-grained field, and hence can be recognized in this way. The dashed contour lines in Fig. 10a–e are used to indicate wt.% metal for <45 μm size assemblages.

Absolute reflectance decreases with increasing metal content, and therefore is a useful spectral parameter. However, for many olivine- and metal-bearing asteroids (one of the intended applications of this study) absolute reflectance may not be known or only poorly constrained, but because it is a useful metric we include it in this discussion. We use reflectance at 1.8 μm as an initial spectral parameter because it falls outside the major olivine absorption band, is less sensitive than most other wavelength regions to the presence of pyroxene and chromite and spectral reddening, and olivine is much brighter than metal in this region. As expected, reflectance at 1.8 μm decreases with increasing metal content, most dramatically at low metal abundances and for more magnesian olivines (Fig. 10a). With increasing Fa content, absolute reflectance of pure olivine powders generally decreases and band depth increases, as shown.

Within each Fa grouping, metal content is probably accurate to within ± 10 wt.%, with uncertainties increasing for high metal content assemblages (>~60 wt.% metal). Such assemblages are discussed below. For larger grain size assemblages, reflectance at 1.8 μm is less than for an equivalent <45 μm size assemblage and band depths are higher. As a result, the parameter space for larger grain sizes shifts upward and to the left in Fig. 10a. The net result is that for larger assemblages (e.g., 45–90 μm), metal content will be underestimated by up to ~20 wt.%, but could be recognizable by falling in a higher Fa field than would be dictated

by band center. For areal assemblages, band depth and reflectance at 1.8 μm change more gradually, and as a result metal content would be underestimated. Pallasite slab spectra overlap the fayalitic fields: their band depths are highly variable, while reflectance at 1.8 μm is uniformly low. They can plot both within and outside of the powder field, and this is probably dependent on the ratio of olivine to metal.

Another useful metric for fine-grained olivine–metal intimate assemblages is FWHM of the 1 μm region olivine absorption band (Fig. 10b), as it is also largely insensitive to spectral reddening. We have found that this parameter decreases with increasing metal content, with the largest changes occurring in the 0 to ~20 and ~50 to ~70 wt.% metal content ranges, probably due to the olivine absorption band sidelobe(s) having depths in these ranges of metal abundance close to 50% of the main 1.05 μm region band. With increasing Fa content, FWHM increases by ~200 nm from Fa_{2,7} (~480 nm) to Fa_{99,9} (~680 nm). King and Ridley (1987) found that FWHM increases from ~640 to ~820 nm from Fa₉ to Fa₈₉, comparable to the overall range of our samples, but with higher absolute values (the King and Ridley (1987) samples were sieved to <60 μm). Mixtures with high Fa olivine are less sensitive to the addition of metal; as a result band depth and FWHM change more slowly and require higher abundances of metal to cause significant changes in FWHM. This figure is also useful for discriminating slab spectra, as they generally have much larger FWHM (due to olivine band saturation), regardless of band depth. Areal mixture spectra change more gradually; for example the 10/90 olivine/metal areal mixture spectrum has a band depth of 9% and FWHM of 410 nm, roughly equivalent to the 50/50 intimate mixture. Therefore, areal mixture spectra analyzed using these parameters would underestimate metal content. With increasing grain size, the field occupied by intimate mixtures would shift upward and to the right, as band depths are larger and FWHM is higher. This could result in larger grain size mixtures shifting into higher Fa regions or outside the <45 μm olivine field completely, and thereby leading to a possible underestimate of metal content.

We use reflectance at 0.56 μm as the next metric (Fig. 10c). This metric yields essentially the same relationships and uncertainties as for the 1.8 μm reflectance metric, but is sensitive to spectral reddening (Sasaki et al., 2001; Noble et al., 2007). However, this parameter may be more readily available for asteroids than longer wavelength data. Reflectance at 0.56 μm decreases with increasing olivine Fa content for a constant grain size, and both band depth and 0.56 μm reflectance decrease with increasing metal abundance. Pallasite slab spectra partially overlap the powdered mixtures, particularly the ~30–60 wt.% metal mixtures, but also extend well outside the powdered field, having low reflectance (<~23%) and very variable band depths.

When we examine band depth versus the 1.8/0.56 μm reflectance ratio (as a measure of spectral slope), increasing metal content causes spectral slopes to converge toward a value of between 1.35 and 1.92 (the range for our fine-grained metal) and a band depth of zero. These two parameters can be used to constrain metal abundances (Fig. 10d) after determination of olivine composition (low, medium, or high Fa). Within each Fa grouping, metal content is probably accurate to within ± 10 wt.%. Uncertainties increase for high metal content assemblages (>~70 wt.% metal), due in part to the range of 1.8/0.56 μm values for pure metals. However, it appears that this is still a good metric for constraining metal content.

The slab spectra plot at various points in this field and hence this combination of metrics cannot be used in isolation to distinguish them from powdered mixtures. For larger grain size assemblages (45–90 μm), olivine band depths are greater and metal is redder, and as a result, using this figure to estimate metal/olivine ratios would tend to underestimate actual metal content. For areal

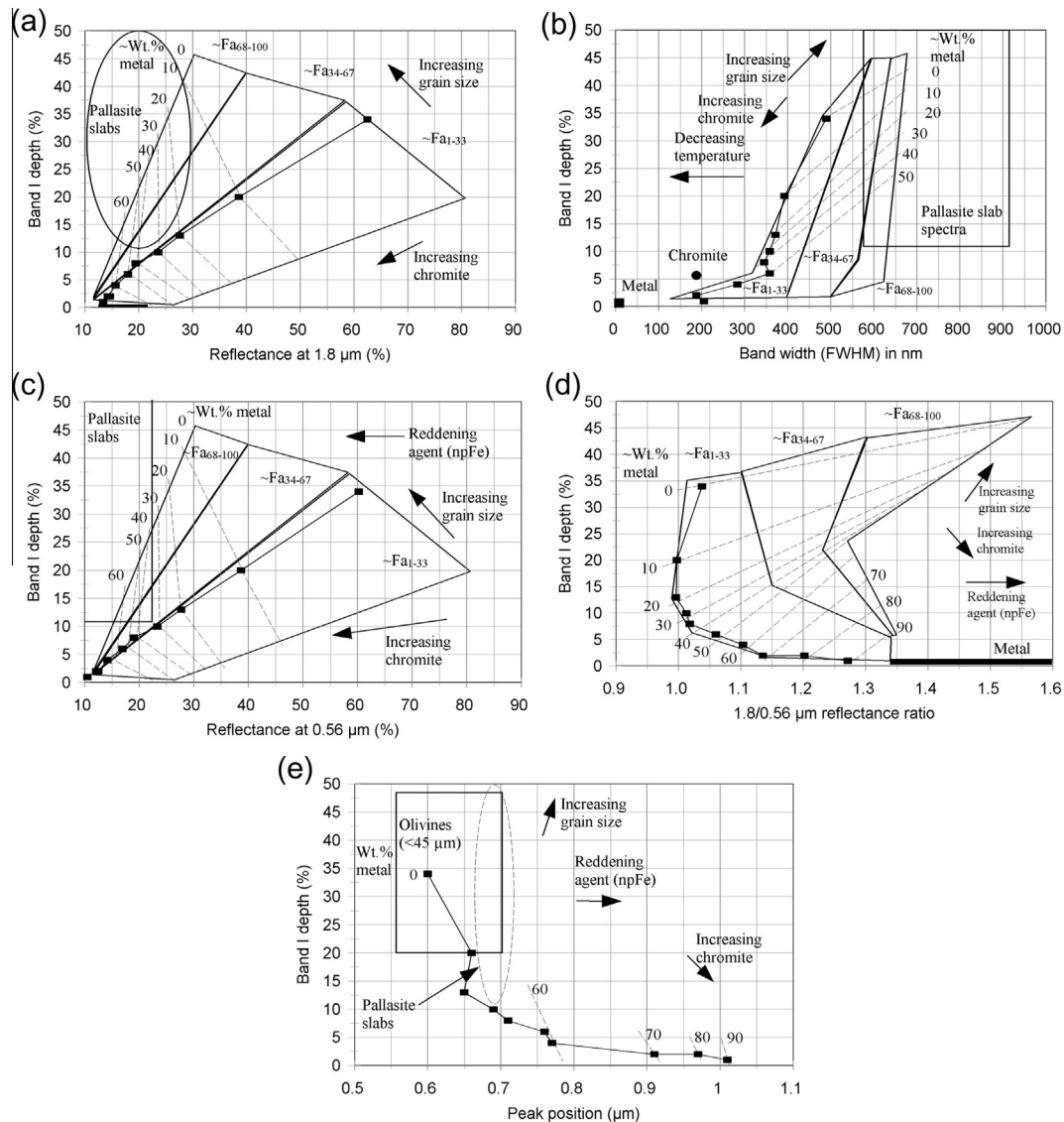


Fig. 10. Spectral metrics for olivine + metal assemblages. Filled squares: <45 μm intimate mixture series OM4 from Table 2. (a) Reflectance at 1.8 μm versus band I depth; ellipse indicates region occupied by pallasite slab spectra. Field has been subdivided into low (Fa₁₋₃₃), medium (Fa₃₄₋₆₇), and high (Fa₆₈₋₁₀₀) Fa olivines on the basis of band I center; this determination is an essential first step in interpreting olivine + metal spectra. Dashed lines are approximate contours as a function of wt.% metal (shown for 0–60 wt.%). Changes in these parameters as a function of increasing grain size and chromite content are shown; the addition of a reddening agent (nanophase iron (npFe)) has little to no effect on these parameters. Field occupied by pure metals, which have no 1 μm absorption band, are shown by the heavy horizontal line at the bottom left corner of the plot. (b) Same as (a) for full width at half maximum versus band I depth. Effect of decreasing temperature (below 300 K) from Hinrichs and Lucey (2002) are also indicated. Points for pure metal and chromite are shown. (c) Same as (a) for reflectance at 0.56 μm versus band I depth. In this case, the addition of a reddening agent causes a reduction in reflectance at 0.56 μm; direction of movement of parameter shown. (d) Same as (a) for 1.8/0.56 μm reflectance ratio versus band I depth. (e) Position of low wavelength reflectance peak (near 0.7 μm) versus band I depth. This parameter is most useful for recognizing and characterizing high metal abundance assemblages. There is no systematic difference as a function of olivine Fa content. Fields occupied by all <45 μm olivine and pallasite slab spectra are indicated.

mixtures, band depth decreases much more slowly with increasing metal content, and hence use of this parameter combination would again underestimate metal content.

Other spectral metrics are better suited for characterizing high metal-content assemblages. These include the position of the band minimum, which falls below the olivine range (i.e., <1.048 μm) at metal abundances of >~75 wt.%, and at even lower metal abundances (>~50 wt.% metal) for very magnesian olivines (Table 2). As olivine is progressively added to metal, a weak and narrow absorption band initially appears in the 1 μm region superimposed on the metal-dominated spectrum. As mentioned, the minimum of this band is initially located shortward of the olivine band center range (<~1.048 μm). This band is accompanied by a local reflectance maximum on the low wavelength side of the olivine band which initially appears near 1 μm, but rapidly moves to shorter

wavelengths as olivine abundance increases (Fig. 10e). The position of this peak is a good indicator of metal abundance for metal-rich (>~70 wt.% metal) assemblages; metal abundance is accurate to ±5–10 wt.% using this metric. This metric is largely insensitive to olivine Fa content.

5.2. Absorption band saturation

Absorption band saturation is expected for larger (few hundred micron size) olivine grains and pallasite slab spectra. We examined whether the long wavelength position of the straight line tangent used to isolate the 1 μm region olivine absorption band could be used as a spectral metric. We found that it occurs in the range of 1.65–2.00 μm for all of the olivines, regardless of grain size and space weathering (Hiroi and Sasaki, 2001). With increasing metal

content, it moves to shorter wavelengths. It is also very sensitive to the presence of even small amounts of phases with a 2 μm region absorption band, which cause it to shift to shorter wavelengths. Since it is not as robust as FWHM, we did not explicitly develop it as a spectral metric.

We also examined how band saturation relates to various spectral metrics. The pallasite slab spectra show a very broad 1 μm region absorption band of low reflectance, similar to pure olivine powders of larger grain sizes (Craig et al., 2007; Clénet et al., 2011; Buz and Ehlmann, 2014). We found that with increasing grain size, the ratio of band depth at 1.05 μm to that at 1.30 μm (after removal of a straight line continuum) is >1.15 for all <45 and 45–90 μm olivine–metal mixtures and pure olivines, and <1.15 for all the pallasite slab spectra and 250–500 μm and larger olivine powders. Craig et al. (2007) determined that this is the size range at which the 1 μm band of olivine saturates. For the pallasite slab spectra of Hiroi et al. (1992) we find that the 1.05/1.30 μm band depth ratio is <1.15 for 4 of the 5 spectra measured in diffuse geometry, 1.27 for the other diffuse measurement, and 1.18 and 1.47 for the two specularly measured spectra. Therefore, a 1.05/1.30 μm band depth ratio of <1.15 seems to be a fairly reliable indicator of a saturated olivine absorption band. Using band depth at 0.85 μm , which is the other olivine M1 band (Sunshine and Pieters, 1998), provides similar discrimination.

As an additional simple metric, FWHM >700 nm is associated with the pallasite slab spectra and 90–250 μm or coarser olivines. We found that the Hiroi et al. (1992) slab spectra have FWHM ranging from 600 to 740 nm. However, their pallasite spectra exhibit evidence of terrestrial weathering (band near 1.9 μm) and other features at longer wavelengths that likely affect the continuum and may skew FWHM. These results suggest that this metric is reasonably effective at discriminating slab and saturated olivine spectra from fine-grained (unsaturated) powders.

5.3. Coarse- and very fine-grained assemblages

To discriminate larger sized, but unsaturated, olivine–metal mixtures from fine-grained mixtures, we can rely on the fact that coarser-grained mixtures are darker and have a deeper 1 μm band than an equivalent fine-grained mixture; coarser-grained metal is also more red-sloped than finer-grained metal: its 1.8/0.56 μm ratio is in the range of 1.45–2.43. Therefore, coarser assemblages are more red-sloped than equivalent fine-grained mixtures. When coarser-grained assemblages are mapped onto the spectral parameters in Fig. 10 the regions they occupy are shifted relative to the fields occupied by the fine-grained mixtures, allowing for recognition of some coarse-grained samples, specifically those that fall outside the pertinent olivine Fa <45 μm field. As an additional check on the presence of coarser-grained assemblages, band center should be included in the analysis, as it can help determine whether a point is “anomalously” present in a low, medium, or high Fa content field. When coarser-grained samples are mapped onto band depth versus reflectance at 1.8 μm (Fig. 10a) or 0.56 μm (Fig. 10c), band depths are generally 10–20% (absolute) greater than <45 μm size samples, while reflectance at 0.56 or 1.8 μm is 20–50% lower. As a result, coarser-grained samples mapped into the parameter fields of Fig. 10a and c will have metal contents that are overestimated by ~ 10 –30 wt.%. Finally, with increasing grain size, both band depth and FWHM increase, and as a result coarse-grained samples may again plot outside the <45 μm field, enabling their recognition.

We can use the saw-cut fines from Springwater to assess how extremely fine-grained assemblages compare to coarser ones (<20 μm). Relative to <45 μm 50:50 olivine:metal, the saw cut fines have comparable reflectance at 0.56 μm (15–19% versus $\sim 17\%$) are generally brighter at 1.8 μm (16–23% versus 17%), have

a shallower and narrower 1 μm region absorption band (depth of 3–4% versus 6% and FWHM of ~ 250 nm versus 360 nm), are slightly more red-sloped (1.8/0.56 μm ratio of 1.07–1.15 versus 1.06), and have their local peak near 0.8 μm (versus 0.76 μm). As expected, most of these trends are opposite to the changes seen for coarser powdered samples. In addition, the ultra fine-grained samples show little or no evidence of the minor absorption bands in the 0.4–0.7 μm region (Fig. 3e).

5.4. Areal versus intimate mixtures

As discussed above, use of the various spectral metrics developed for intimate mixtures will tend to underestimate metal abundance, as areal mixture spectra, at least initially, change more slowly than intimate mixtures. Therefore, there is no good easily-applied metric to confidently discriminate areal mixtures with <50 wt.% metal from intimate mixtures containing much less metal. As an example, when we plot the 50/50 areal mixture for OLV003 (Fa_{9.6}), we find that apparent metal content is <10 wt.% using all the metrics discussed above. The only indication that this is not an intimate mixture is that the band depth versus 1.8 μm reflectance value plots within the medium Fa content field (Fig. 10a). These findings are not unexpected as metal is spectrally quite featureless and only causes subtle spectral changes at low abundances in areal mixtures. On asteroidal regoliths, the assumption of intimate mixing is probably valid.

5.5. Minor olivine absorption bands

In addition to the major 1 μm region absorption feature due to Fe²⁺ crystal field transitions, powdered olivine spectra also exhibit

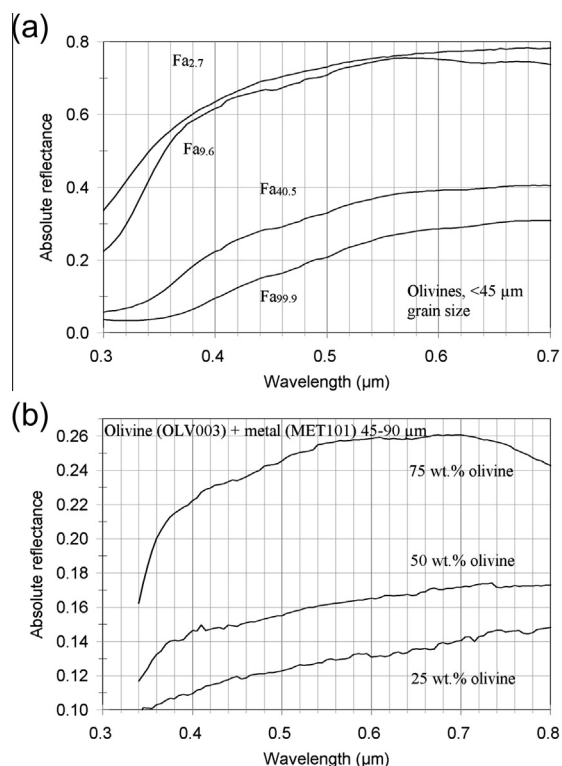


Fig. 11. Effects of composition and grain size on the short wavelength portion of olivine reflectance spectra. (a) <45 μm olivines of different Fa content; absorption features (near 0.400, 0.450, 0.495 (and ~ 0.63 μm) are most evident in the Fa_{9.6} spectrum, and to a lesser extent in the more Fa-rich spectra. (b) Appearance of these same absorption bands in <45 μm Fa_{9.6} olivine with increasing metal content; bands generally become less discernible.

a number of minor absorption bands in the 0.4–0.7 μm region (Fig. 11a). The nature of the band near 0.65 μm is uncertain but is present in nearly all fine-grained (<45 μm) olivine spectra (King and Ridley, 1987; Sunshine and Pieters, 1998; Sunshine et al., 2007). It is least apparent in the fayalitic and forsteritic end member spectra (Fig. 11a). Sunshine and Pieters (1998) noted that this feature is enhanced in fine-grained spectra. However, we find that this feature persists across a range of grain sizes, and is in fact most evident in coarser-grained spectra (Fig. 1c), as expected for weak absorption bands. The shorter wavelength bands, present near 0.400, 0.450, and 0.495 μm are attributed to spin forbidden transitions in Fe^{2+} (Burns et al., 1972) and also become more apparent with increasing grain size. It would appear that the presence of minor absorption bands could be used to recognize coarser-grained assemblages. These bands generally persist, albeit at reduced intensities, in olivine + metal mixtures (e.g., Fig. 11b). The absence of the minor olivine absorption bands would be indicative of: (1) very low Fa olivines ($\text{Fa}_{<5}$), (2) very fine-grained olivine ($\ll 45 \mu\text{m}$), or (3) abundant metal.

5.6. Temperature effects

The effects of temperature on olivine reflectance spectra have been examined by a number of investigators (e.g., Singer and Roush, 1985; Roush and Singer, 1987; Lucey et al., 1998; Hinrichs et al., 1999; Schade and Wäsch, 1999; Moroz et al., 2000; Hinrichs and Lucey, 2002). They found that the olivine 1 μm absorption feature narrows with decreasing temperature, but that band position is relatively unchanged (Sunshine et al., 2007). Spectral slope, band depth, and absolute reflectance are also largely unaffected by temperature variations (Hinrichs and Lucey, 2002). FWHM was found to vary from ~400 to ~680 nm over the temperature range from 83 K to 448 K. Therefore, temperature effects should be accounted for when using FWHM as a spectral metric. Our results show that a reduction in FWHM is also associated with a decrease in olivine grain size, a decrease in olivine Fa content, and increasing metal content. However, all of these variations are accompanied by other spectral changes that do not occur with temperature variations.

5.7. Nanophase versus larger iron

As part of a companion study of the effects of npFe on silicate spectra, we measured olivine + npFe intimate mixture spectra (Fig. 12). We examined three sizes of olivine (<45, 45–90, and <250 μm) intimately mixed with two different sizes of synthetic npFe powders (50 nm and 10 μm average grain size). The npFe powders are of a size expected to be close to the size that should lead to reddening plus darkening (50 nm) and darkening without reddening (10 μm) (Lucey and Riner, 2011). However, it appears that both of our iron powders caused darkening but little or no reddening.

Band depths do not appreciably decrease until ~0.5 wt.% 50 nm-size Fe or ~2 wt.% 10 μm -size Fe is present (Table 2). Spectral slope (1.8/0.56 μm reflectance ratio) does not redden appreciably or systematically for the 50 nm-size Fe, but does redden for the 10 μm -size Fe. This is contrary to the results of Noble et al. (2007) and Lucey and Riner (2011) who found that finer-grained Fe reddens and darkens, while coarser Fe darkens but does not redden. We suspect that these discrepant results may arise from differences between naturally-occurring npFe and our experiments. Naturally occurring npFe is normally present in a well-dispersed form in a silica-rich matrix, either in the outermost rind of mineral grains or in agglutinitic glass, whereas our experiments involve npFe mixed with mineral grains, where the npFe resides on, not in, the mineral grains, and also likely forms clumped aggregates

which will behave optically like larger particles. Also the average size of our finer-grained npFe (50 nm) is close to the boundary between particles that redden and those that darken.

A number of investigators have used various approaches to examine the spectrum-altering effects of space weathering in the context of olivine. Yamada et al. (1999) presented reflectance spectra of pressed pellets of olivine powder (Fa_9) subjected to pulse laser irradiation (1064 nm), proton implantation, and a combination of both to simulate both solar wind implantation and micro-meteorite bombardment. Pulse laser irradiation led to overall darkening and reddening, which was most pronounced at shorter wavelengths. The lowest energy (1 mJ) caused no discernible change in reflectance. Higher energy pulses (15 and 30 mJ) resulted in overall darkening and reddening, which was most pronounced at shorter wavelengths, but extended to 2.5 μm . Band depth showed a slight reduction, from 35% to 29%, while FWHM appeared to be unaffected. High-energy (1 MeV) proton irradiation (total doses of $4.9 \times 10^{15}/\text{cm}^2$ and $1.4 \times 10^{16}/\text{cm}^2$) had very little effect on the olivine spectra; spectra were slightly reddened below ~1.8 μm (1.8/0.56 μm ratio increasing from 1.11 to 1.20), while the 2.4/1.8 μm ratio and band depth were unaffected. When proton implantation and laser irradiation were combined, the spectra behaved much like the laser irradiated samples. Yamada et al. (1999) did not detect the formation of npFe in their experiments. They were unable to suggest a robust explanation for the reddening and darkening that was most evident in the laser irradiation results.

Sasaki et al. (2001, 2002, 2003) and Hiroi and Sasaki (2001) used laser irradiation of olivine to simulate the spectrum-altering effects of space weathering, specifically high-velocity dust impacts. They found that this type of laser irradiation resulted in the production of npFe particles, with several up to 30 nm in size, embedded within the outer rind of the grains (Sasaki et al., 2003). Increasing amounts of irradiation resulted in increasingly red-sloped spectra; the reddening extended to progressively longer wavelengths with increasing irradiation dose. However, olivine band depth was largely unaffected by the treatment, varying between 29% and 35% for all of the samples (Sasaki et al., 2001); FWHM also appeared to be unaffected by the laser irradiation. Overall reflectance decreased more in the visible than the longer wavelength regions. These results are in contrast to those of Kohout et al. (2014) who found that increasing amounts of ~7–20 nm size npFe resulted in decreases in band depth and increasingly red slopes across the entire 0.35–2.5 μm range. However, it should be noted that the npFe in their samples were produced in a different way than the procedure used by Sasaki et al. (2001).

Sasaki et al. used these data to model some asteroid spectra. Sasaki et al. (2003) were able to match albedo, overall shape and band position of Asteroid 446 Aeternitas using a combination of the spectra of the unirradiated olivine (2.0%), the different laser-irradiated olivines (93.1%), minor pyroxene (irradiated and unirradiated; 0.9%), and chromite (4.0%). A simple comparison of the spectrum of 863 Benkoela (Sasaki et al., 2001) to the laboratory spectra was able to bracket its spectrum between the unirradiated and least irradiated olivine spectra.

Brunetto and Strazzulla (2005) performed irradiation experiments on a solid sample of a coarse-grained peridotite that consists largely of olivine, using different ions (H^+ , He^+ , Ar^+ , and Ar^{2+}) and fluences to simulate solar wind irradiation, with irradiation under vacuum and with both in situ and ex situ spectral measurements made. After irradiation, the ex situ sample spectra were darker, and redder, as measured by both the 1.8/0.56 and 2.4/1.8 μm reflectance ratios. Band depths were slightly reduced after irradiation, decreasing from 26% to between ~20% and 24%, and FWHM was also reduced. As this sample is not pure olivine, it is less reliable for isolating the spectrum-altering effects of irradiation on

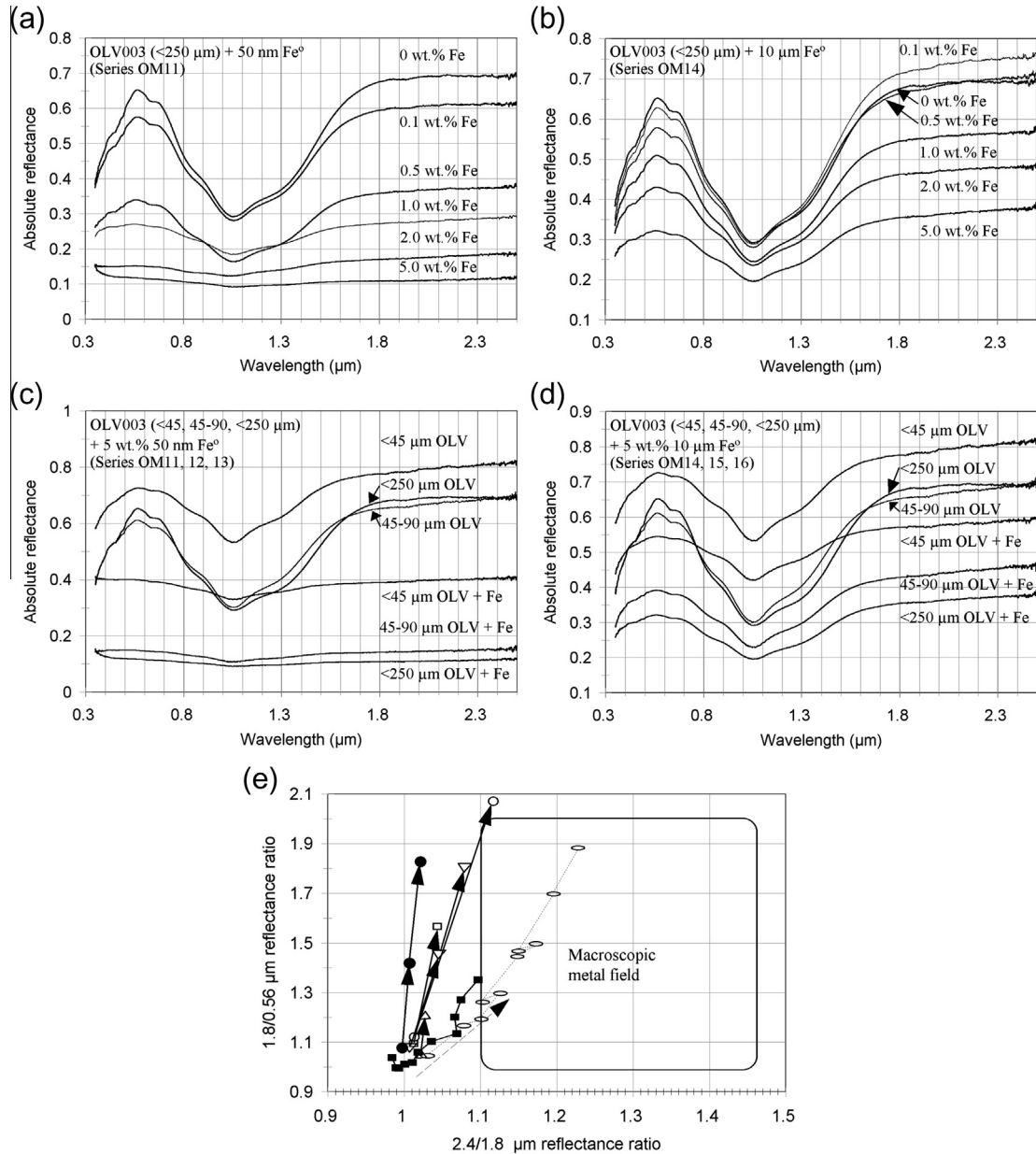


Fig. 12. Reflectance spectra of intimate mixtures of olivine + nanophase iron (series OM11 to OM16 in Table 2). (a) <250 μm olivine + 50 nm size iron. (b) <250 μm olivine + 10 μm size iron. (c) Three different sizes of olivine + 5 wt.% 50 nm size iron. (d) Three different sizes of olivine + 5 wt.% 10 μm size iron. (e) 2.4/1.8 μm versus 1.8/0.56 μm reflectance ratios for <45 μm olivine + metal mixtures (squares – series OM4 in Table 2). The diagonal dashed arrow near the bottom of the figure shows the direction of movement with increasing macroscopic iron abundance). Laser-treated olivines from Hiroi and Sasaki (2001): filled circles; the arrows joining the circles show the change in these ratios from unirradiated to 2 J/cm² and 27 J/cm² dose and to 1.9 J/cm² and 52 J/cm² dose. Ar⁺-irradiated olivine from Brunetto et al. (2006a): open circles; the arrow joining these circles shows the change in these ratios from unirradiated to 7 × 10¹⁵ Ar⁺/cm², 200 keV. He⁺ irradiated olivines from Brunetto et al. (2006b) and Marchi et al. (2005): open rectangles; the arrow joining these rectangles shows the change in these ratios from unirradiated to after 7 × 10¹⁵ Ar⁺/cm², 200 keV. He⁺ irradiated olivines from Loeffler et al. (2009): open upright triangles; the arrow joining these triangles shows the change in these ratios from unirradiated to 25 × 10¹⁷ ions/cm² of 4 keV He⁺ ions. Because of the limited spectral range, we used the 1.8/0.66 μm ratio instead of 1.8/0.56 μm. Laser-irradiated (1064 nm) olivine powder from Yamada et al. (1999): open inverted triangles; the arrows joining these triangles show the change in these ratios from unirradiated to 15 mJ to 30 mJ. Heat-treated olivines from Kohout et al. (2014): open ellipses. Increasing metal causes the spectral ratios to generally shift from lower left to upper right; data points with increasing npFe are connected with dashed lines. The large rounded rectangle shows the field occupied by the various macroscopic metal powders used in this study.

olivine. They determined that heavier ions darken and redden the spectra more efficiently than light ones.

Marchi et al. (2005) and Brunetto et al. (2006b) presented results of ion irradiation of olivine, designed to simulate solar wind irradiation, using different fluences of Ar⁺. They used 100–200 μm pressed powders of an iron-poor olivine (San Carlos, ~Fa₉) irradiated in vacuum and measured both in situ and ex situ reflectance spectra. They found that irradiation led to an overall darkening and reddening of spectral slope across the entire 0.3–2.5 μm interval; FWHM was relatively unchanged. Band depth for the after

7 × 10¹⁵ Ar⁺/cm², 200 keV irradiation was largely unaffected (44% versus 42%). As with other experimental results, reddening was more pronounced at shorter wavelengths.

Brunetto et al. (2006a, 2007) used a nanopulsed UV excimer laser (193 and 248 nm wavelengths) to simulate micrometeorite bombardment of various silicates, including olivine, in high vacuum conditions. The olivine used (~Fa₉) had a grain size of ~200 μm in a pressed pellet. They used different fluences, both above and below the ablation threshold. They found that all the irradiated materials (including olivine) showed both reddening

and darkening. In the case of the olivine, the reddening and darkening extended across the full 0.3–2.5 μm range. Band depth is slightly reduced by irradiation, decreasing from $\sim 46\%$ to 40–42%, and reflectance at 1.8 μm is also slightly reduced, from 85% to 68–74%; FWHM is also reduced. Larger changes are seen in the visible region, with reflectance at 0.56 μm reduced from 75% to 31–35%. They determined that the experimental conditions resulted in the formation of amorphous rinds and npFe.

Loeffler et al. (2009) examined the spectrum-altering effects of irradiation of olivine by 4 keV He^+ ions on pressed powders ($<45 \mu\text{m}$) and solid olivine, designed to investigate the effects of solar wind implantation. They found that He^+ irradiation led to overall spectral reddening due to metallization of iron in the olivine (Fe_9), with reddening increasing most strongly in the early stages of irradiation, and a concomitant production of metallic iron. The reddening was more pronounced at shorter wavelengths, and they observed little darkening. The area of the 1 μm band, due to Fe^{2+} in olivine also decreased with increasing fluence, while optical depth increased across the full 0.66–2.5 μm region. FWHM appears to have been unchanged. They concluded that the formation of npFe is more important than amorphization in changing the optical properties of olivine (Carrez et al., 2002).

More recently, Kohout et al. (2014) produced olivine with surficial npFe by thermal treatment of olivine. They were able to produce higher npFe concentrations than other experimental approaches, and thus were able to investigate the spectrum-altering effects of npFe over a wide range of abundances. Their technique also allowed for production of a more uniform npFe size range. Their sample spectra exhibit increasing spectral reddening with increasing amounts of npFe. Increasing npFe also correlated with a decrease in band minimum, band depth (at the higher npFe concentrations), overall reflectance, and band width; band centers were largely unaffected. They suggested that the spectrum-altering effects of npFe did not depend on whether or not the npFe was embedded in a silica-rich amorphous coating. Kohout et al. (2014) also confirmed that the spectrum-altering effects of npFe do not scale linearly with npFe concentration – the greatest changes are found at low npFe concentrations. In contrast to laser-irradiation and particle implantation experiments, the reddening caused by their npFe was more similar to macroscopic metal (Fig. 12e). The fact that the trajectories of their samples differs from the other experimental results may be due to the formation of iron oxide coatings on the npFe grains (which reside on the surface of the olivine grains) when the samples were exposed to the atmosphere for spectral measurements, a possibility noted by Kohout et al. (2014), or differences in npFe grain size and/or abundances. However, we are unable at present, to assign a precise mechanism to the spectral differences. Kohout et al. (2014) concluded that whether nanophase iron is located on the surfaces of olivine grains or in an amorphous silica-rich coating does not seem to appreciably affect whether this material will induce spectral reddening. However, some of the spectral metrics used in our analysis (e.g., Fig. 12e), and other experimental data (e.g., Loeffler et al., 2009) suggest that this may not be the case.

The experiments described above suggest a number of things. It appears that the presence of npFe mimics many of the spectral changes associated with macroscopic metal: decreasing band minimum position, band width, overall darkening, and reddening of spectral slope. However, other parameters are less sensitive to the addition of npFe in amounts consistent with moderate space weathering than macroscopic metal, in particular band depth. One key difference that appears to exist between npFe and macroscopic metal is that macroscopic metal imparts a flatter red spectral slope than npFe, whose spectral slope is concave downwards; in other words it decreases reflectance more towards shorter wavelengths. As a result, the ability to discriminate npFe

from macroscopic metal is best achieved by either focusing on longer wavelength regions or comparing short to long wavelength regions. One additional observation is suggested by the laboratory experiments. While amorphization of olivine rims has a smaller effect on olivine spectra than the presence of npFe (e.g., Yamada et al., 1999; Loeffler et al., 2009), npFe embedded in a silica-rich amorphous rind should have different spectral properties than npFe on the surfaces of olivine grains. However, the extent to which this affects olivine reflectance spectra has not been fully quantified. We note that a pure sample of 50 nm-size npFe is characterized by $<3\%$ reflectance and a broad concave shape over the 0.4–2.5 μm range, while 50 nm-size npFe embedded in silica gel shows more complex optical behavior, which varies from blue to red-sloped, with the highest 50 nm npFe in silica gel concentration measured by Noble et al. (2007) showing the same concave shape as the pure 50 nm npFe, but with higher overall reflectance.

Given all of this, it appears that space weathering which results in the production of npFe, versus the presence of macroscopic iron can be at least partially discriminated. One approach is to focus on longer wavelength regions (e.g., reflectance at 1.8 μm) which are more affected by macroscopic metal than by npFe. Another is to use reflectance ratios that sample different wavelength regions. The spectral reddening associated with space weathering simulations in the laboratory is often confined to, or most pronounced in, shorter wavelength regions ($<\sim 1.8 \mu\text{m}$), while the spectral reddening associated with the presence of metal with grain sizes larger than a few tens of nanometers causes reddening across the entire 0.3–2.5 μm range. As an example, the results of Yamada et al. (1999) show that for olivine irradiated with 30 mJ laser pulses, reflectance at 0.56 and 1.8 μm decrease by 45% and 10%, respectively, relative to the unirradiated olivine. The 2.4/1.8 versus 1.8/0.56 μm reflectance ratios show that for the laboratory simulated space weathering, the 2.4/1.8 μm ratio is less affected than the 1.8/0.56 μm ratio, with the latter changing more rapidly. In addition, the trajectory of changes in these spectral ratios differs. The olivine + macroscopic iron mixtures generally show a more symmetric change in both the 1.8/0.56 and 2.4/1.8 μm ratios, and the trend is largely insensitive to grain size. This suggests that these two spectral ratios may be able to partially discriminate the production of npFe produced during space weathering from “native” (macroscopic) metal in olivine + metal assemblages (Fig. 12e).

Some additional speculations are also warranted. If space weathering of olivine + metal asteroid surfaces leads to the production of “large” npFe, then it is possible that this space weathering-produced metal will be spectrally more similar to the meteoritic metal used in our mixtures. The results of Noble et al. (2007) strongly suggest that the degree of reddening and wavelength range over which this occurs is dependent on both npFe grain size and abundance. The most effective grain size range for inducing spectral reddening is between ~ 2 and 20 nm.

5.8. Recommended analytical procedure

Based on our analysis, we can suggest a procedure for systematic analysis of suspected olivine–metal assemblages. The first step is to examine the spectra for evidence of a 2 μm region absorption band that may indicate the presence of pyroxene (or chromite). Pyroxene is known to strongly modify olivine spectral properties such as band centers at low (down to $\sim 15 \text{ wt.}\%$) abundances (Cloutis et al., 1986). If this is the case, spectral metrics specific to olivine + metal assemblages are not robust.

If a spectrum appears reasonably free of these interfering phases, the next step is to determine band minimum and divide out a straight line continuum across the 1 μm region. Comparison of band minimum to center can help determine if an assemblage is

extremely metal-rich (>75 wt.%); band minima shorter than the olivine range (<~1.048 μm) are characteristic of such metal-rich samples. If this is the case, visible region peak position should also occur longward of ~0.75 μm (Fig. 10e). The presence of olivine coarse enough to have appreciable band saturation (such as a pallasite slab) can be recognized by a 1.05/1.30 μm band depth ratio <1.15 and a FWHM of >700 nm.

Once metal-rich and/or spectrally-saturated assemblages have been recognized, the various metrics show in Fig. 10 can be applied. The first step is to use the band center to determine whether the spectrum falls (roughly) into the low, medium, or high Fa regions. The Fa content fields have been defined to help ensure that internally consistent results are obtained. If the various spectral metrics occupy different Fa content fields, a coarser assemblage or an areal assemblage may be indicated, although we have not rigorously defined such deviations. By plotting the various spectral metrics, the probable olivine/metal ratio, and approximate olivine composition can be retrieved. As mentioned, for intimate fine-grained mixtures, metal abundance to ± 10 wt.% is probably attainable.

6. Olivine + metal-rich asteroids

As discussed above, a number of olivine and olivine + metal-rich asteroids are known. They reside among a few different taxonomic classes (Table 4) and many have been investigated by multiple groups (Table 5). Their presence among different taxonomic classes may be attributed to differences in olivine composition, grain size, metal abundance, or accessory phases. We have re-analyzed available spectra of such bodies on the basis of our derived spectral metrics. In a companion study we applied different types of metrics to a number of olivine-bearing asteroid spectra (Sanchez et al., 2014).

6.1. Previous analyses

Of the various taxonomic asteroid classes, the likeliest olivine-metal asteroids are contained in the traditional A and S(I) taxonomic classes (Cruikshank and Hartmann, 1984; Gaffey et al., 1993). Asteroids in these groups have been spectrally characterized by a number of investigators (e.g., Bell et al., 1984; Cruikshank and Hartmann, 1984; Cloutis et al., 1990; Hiroi et al., 1992; Gaffey et al., 1993; Lucey et al., 1998; Sunshine and Pieters, 1998; Sunshine et al., 1998, 2007; Mothé-Diniz et al., 2000; Burbine and Binzel, 2002; Bus and Binzel, 2002; de León et al., 2004; Reddy et al., 2005; Birlan et al., 2007; Hardersen et al., 2011). Previous investigators suggested that metal may be present on a number of A-asteroids, as their spectra are substantially redder than pure olivine (e.g., Bell et al., 1984; Cruikshank and Hartmann, 1984). Below we summarize some past multi-body spectral studies.

Hiroi et al. (1992) used diffuse and specular reflectance spectra of two pallasite slabs to analyze telescopic spectra of four A-asteroids. They were able to fit the spectrum of 113 Amalthea

with a linear combination of their pallasite spectra, but were unable to produce good fits for the spectra of 246 Asporina, 354 Eleonora, and 446 Aeternitas. They found that they were unable to reconcile the need for abundant metal to produce the red slopes of the asteroids with the need for abundant olivine to produce a deep band. They were also unable to reproduce the steep linear slopes in the visible region. It should be noted that their pallasite spectra show variable evidence of terrestrial weathering (absorption band near 1.9 μm , reflectance dropoff to longer wavelengths in the Y-8451 spectra, an absorption edge near 0.5 μm and numerous bands in the 1.6–2.5 μm region; some of the latter features may be attributable to lacquer used to protect the samples from oxidation). Their results suggest the presence of a material that can redden the spectra at shorter wavelengths, unlike macroscopic metallic iron, whose reddening effect is much more linear with wavelength.

Gaffey et al. (1993) conducted a comprehensive analysis of S-class asteroids and defined a number of groups based on a variety of spectral parameters. Of most interest here is the S(I) class. This class likely represents the most olivine-rich asteroids, having Band I centers within the olivine field, and no discernible absorption band in the 2 μm region. Their S(I) group includes 42 Isis, 113 Amalthea, and 354 Eleonora. The S(II) group has band centers within or just short of the olivine band center field, as well as a weak 2 μm region absorption feature; overall they were interpreted as consisting predominantly of olivine with subordinate low-calcium pyroxene.

Lucey et al. (1998) examined four A-asteroid reflectance spectra (246 Asporina, 289 Nenetta, 446 Aeternitas, and 863 Benkoela) in the context of how temperature variations could affect their interpretation. They focused on continuum-removed band width, which is very sensitive to temperature, and concluded that all four asteroids are dominated by low-iron (Fa_{5–15}) olivine.

Bus and Binzel (2002) defined the A-class as having a very steep red slope shortward of 0.75 μm and a moderately deep absorption longward of 0.75 μm . This definition seems appropriate for olivine-rich asteroids, but in the case of olivine + metal assemblages, metal tends to reduce the red slope and depth of absorption longward of 0.75 μm . Hence, metal-rich olivine-bearing asteroids may not be fully captured using these criteria, and may reside within the L, Q, R, S, and Sa classes (Table 4). However, we have restricted our analysis to asteroids that have been identified as belonging to the canonical A and S1 classes.

Burbine and Binzel (2002) analyzed reflectance spectra of ten A-asteroids and divided them into two groups on the basis of 1 μm band depth. The asteroids with the deeper bands (35–54% deep) are confined to the larger asteroids, while the smaller ones have shallower bands (11–22%). All the asteroid spectra are redder than olivine-rich meteorites and all but the most fayalitic (Fa_{>90}) olivines. They also found that pulse laser irradiation of olivine, meant to simulate micrometeorite impacts, could simulate the reddening seen in the A-asteroids, while preserving the strong UV dropoff and olivine absorption feature. They also suggested that the A-asteroids with shallower absorption bands could be explained as olivine + metal assemblages that have been more heavily altered in some way.

Sunshine et al. (2007) analyzed a number of A-asteroid spectra using previously acquired and new telescopic data. Their analysis included application of MGM analysis (Sunshine and Pieters, 1998) as well as corrections for temperature-induced variations in olivine absorption bands (Lucey et al., 1998) in order to derive olivine compositions. They determined olivine compositions as follows: ~Fa₁₀ for 354 Eleonora, ~Fa₂₀ for 1951 Lick, ~Fa₄₀ for 246 Asporina and 289 Nenetta, and magnesian olivine for 446 Aeternitas, 863 Benkoela, 984 Gretia, 2501 Lohja, and 3819 Robinson.

In an analysis of spectra of M-/X-asteroids, Hardersen et al. (2011) identified three asteroids that exhibit a weak absorption

Table 4
Spectral characteristics of some of the Bus and Binzel (2002) asteroid taxonomic classes.

Class	Description
A	Very steep red slope shortward of 0.75 μm and a moderately deep absorption longward of 0.75 μm
L	Very steep red slope shortward of 0.75 μm and then becoming approximately flat
S	Steep, reddish slope shortward of 0.7 μm and a moderate to deep absorption longward of 0.75 μm
S1	Spectrum intermediate between S and L types
Sq	Spectrum intermediate between S and Q types
Sr	Spectrum intermediate between S and R types

Table 5
Selected spectral parameters for presumed olivine-rich asteroids. Sources of data: [1] Burbine and Binzel (2002). [2] Cruikshank and Hartmann (1984). [3] Bell et al. (1984). [4] Birlan et al. (2007). [5] Gaffey et al. (1993). [6] Hardersen et al. (2011). [7] Mothé-Diniz et al. (2008). [8] Reddy et al. (2005). [9] Sunshine et al. (2007). [10] Spectral parameters from this study; band minima, centers and depths calculated using different approaches; see text for sources of spectral data. [11] de León et al. (2004). [12] Sawyer (1991). [13] Kelley and Gaffey (2000). [14] Reddy et al. (2011a, 2011b).

Asteroid	Geometric albedo ^a	Reflectance ratios		1 μm region absorption band			0.7 μm peak position (nm)	1 μm region band		Source of data	
		2.4/1.8 μm	1.8/0.56 μm	Band depth (%)	Band minim. (μm)	Band center (μm)		FWHM ^d (nm)	FWHM ^l		
9 Metis	0.213 \pm 0.007	1.03	1.47	7	\sim 1.04	\sim 1.075	\sim 0.88	470	510	[3, 12]	
		0.99	1.42	9	\sim 1.02	1.062	\sim 0.88	320	360	[13]	
				7		1.075					[10]
42 Isis ^c	0.16 \pm 0.005		1.28	8		1.080				[10]	
			1.56	11	1.04	1.05	0.74	440	480	[1]	
			1.35 ^h	9	1.01	1.03	0.71	400	440	[5]	
			1.50 ⁱ	15	\sim 1.05	1.06	0.73	450	490	[10]	
		0.98	1.50 ^j	14	\sim 0.97	\sim 1.03	0.74	350	390	[10]	
113 Amalthea	0.22 \pm 0.03		1.50	13	1.000	0.997				[10]	
			1.42 ^j	21	1.05	1.05	0.74	430	470	[5]	
		1.06	1.42 ^j	30	\sim 1.04	1.042	0.75	470	510	[10]	
		0.96	1.30 ⁱ	28	\sim 1.02	\sim 1.037	0.75	510	550	[10]	
				28	1.049	1.058					[10]
246 Asporina ^c	0.20 \pm 0.03		1.45	35	1.07	1.10	0.74	570, 440 ^g	620, 490 ^g	[1]	
			1.76	31		1.01	0.75	400	450	[2]	
		1.05	1.84 ^j	32	\sim 1.04	1.060	0.74	450	500	[10]	
		0.94	1.60 ⁱ	24	\sim 1.02	\sim 1.04	0.74	480	530	[10]	
		1.00	1.61 ^k	24	\sim 1.06	1.065	0.74	500	550	[10]	
				24	1.049	1.058					[10]
289 Nenetta ^c	0.29 \pm 0.03		1.68	54	1.07	1.09	0.71	700, 480 ^g	760, 540 ^g	[1]	
				41	1.09						[5]
			2.5	46	\sim 1.07		0.72	550	610	[9]	
			2.2 ^h	44	\sim 1.05	1.085	0.72	610	670	[10]	
		1.03	1.95 ⁱ	46	\sim 1.06	\sim 1.07	0.72	500	560	[10]	
354 Eleonora ^f	0.211 \pm 0.007		1.51	43	1.074	1.083				[10]	
			1.53	19	\sim 1.04	\sim 1.06	0.71	520	575	[1]	
			2.00	24	1.05	1.10	0.72	440	495	[5]	
			1.72 ^j	29	\sim 1.05		0.72	430	485	[9]	
		1.05	1.65 ⁱ	27	\sim 1.05	1.060	0.73	400	455	[10]	
		1.03		25	\sim 1.05	\sim 1.06	\sim 0.85	\sim 350	\sim 405	[10]	
446 Aeternitas ^c	0.222 \pm 0.006		1.26	22	1.049	1.049				[10]	
			2.17	48	1.08	1.09	0.73	550, 490 ^g	605, 545 ^g	[1]	
			2.17	35	\sim 1.05	\sim 1.09	0.70	580	635	[3]	
			1.78 ^e	35	\sim 1.05	1.07	0.70	580	635	[5]	
		0.97	1.98 ⁱ	39 ^e	\sim 1.05	1.07	$<$ 0.75	470	525	[8]	
			2.08 ^h	37	\sim 1.05	1.065	0.73	500	555	[10]	
766 Moguntia ^{e,f}	0.124 \pm 0.007	1.00	2.42 ^k	40	\sim 1.07	\sim 1.08	0.73	500	555	[10]	
				40	1.055	1.064	0.74	480	535	[10]	
				40	1.069	1.093					[10]
			1.02	7	\sim 1.05	1.051		350	410	[4]	
		1.00	1.02 ^e	\sim 10	1.06	1.068	$<$ 0.81	375 ^e	435 ^e	[6]	
798 Ruth	0.148 \pm 0.005		1.02 ^e	10	1.04	1.068	$<$ 0.8	290 ^e	350 ^e	[7]	
			1.05 ^e	9	1.045	1.060					[10]
		1.03	0.94 ^e	\sim 4–5	1.06	1.056	$<$ 0.78	220 ^e	280 ^e	[6]	
				5	\sim 1.05		$<$ 0.8	240 ^e	300 ^e	[7]	
863 Benkoela ^c	0.44 \pm 0.027		1.066	5		1.069				[10]	
			1.66	54	1.07	1.08	0.73	560, 460 ^g	640, 540 ^g	[1]	
		1.08	2.35 ^j	38	\sim 1.03	\sim 1.05	0.72	500	580	[10]	
		1.06	\sim 2.1	40	\sim 1.03	\sim 1.07	0.72	480	560	[10]	
984 Gretia	0.36 \pm 0.012			39		1.068				[10]	
		1.00	1.55 ^j	34	\sim 1.04	\sim 1.05	0.72	500	560	[10]	
1126 Otero ^c	0.1786 \pm 0.033			34	1.055	1.054				[10]	
			1.29	17	0.94	1.07	0.74	470	500	[1]	
			1.48 ^h	18	\sim 1.01	\sim 1.07	0.75	450	480	[10]	
1210 Morosovia 1600 Vyssotsky ^c	0.127 \pm 0.007 0.547 \pm 0.076	1.01	1.32	10	0.93	\sim 0.98		260	290	[10]	
						\sim 1.05				[10]	
		0.99	0.92 ^e	\sim 8–9	1.06	1.047	$<$ 0.73	\sim 350	\sim 410	[6]	
1951 Lick	0.0895 \pm 0.020		1.30	16	0.91	1.04	0.74	\sim 400	\sim 400	[1]	
			1.55 ^h	16	\sim 1.03	\sim 1.06	0.73	\sim 320	\sim 320	[10]	
2501 Lohja	0.275 \pm 0.020	1.06	1.032		1.032	1.083				[11]	
		0.96	2.62 ^j	42	\sim 1.04	1.065	0.72	540	505	[10]	
2715 Mielikki ^c	0.136 \pm 0.017		2.17	42	1.044	1.061		470	445	[9]	
							\sim 0.72			[10]	
2732 Witt ^c	0.30 \pm 0.03		1.38	18	1.02	1.06	0.75	\sim 420	\sim 475	[1]	
			1.70 ^h	\sim 15	\sim 1.04	\sim 1.06	\sim 0.72	\sim 450	\sim 505	[10]	
3819 Robinson	0.36 \pm 0.298		1.29	11	0.89	(0.90) ^b	0.74	\sim 340	\sim 390	[1]	
			1.60 ^h	\sim 7	\sim 1.03	\sim 1.03	\sim 0.75	\sim 350	\sim 400	[10]	
	1.02	1.65 ^j	39	\sim 1.04	\sim 1.06	\sim 0.74	540	590	[10]		
	1.01	1.55 ^j	38	\sim 1.05	1.055	\sim 0.74	540	590	[10]		

Table 5 (continued)

Asteroid	Geometric albedo ^a	Reflectance ratios		1 μm region absorption band			0.7 μm peak position (nm)	1 μm region band		Source of data
		2.4/1.8 μm	1.8/0.56 μm	Band depth (%)	Band minim. (μm)	Band center (μm)		FWHM ^d (nm)	FWHM ^f	
4142 Dersu-Uzala ^c	0.164 \pm 0.011		1.46 ^h	39	\sim 1.06	\sim 1.07	\sim 0.74	540	590	[10]
			1.49	22	0.90	1.05	0.74	\sim 530	\sim 535	[1]
		1.13	2.15 ^j	\sim 22	\sim 1.00	\sim 0.98	\sim 0.76	\sim 380	\sim 385	[10]
4713 Steel ^c	0.424 \pm 0.082		1.78 ^h	\sim 23	\sim 0.98	\sim 1.03	\sim 0.75	\sim 380	\sim 385	[10]
			1.42	14	0.92	0.92	0.74	\sim 320	\sim 330	[1]
136617	0.42 \pm 0.10		1.71 ^h	\sim 12	\sim 1.00	\sim 0.94	\sim 0.72	\sim 250	\sim 260	[10]
		\sim 1	1.05	\sim 40	\sim 1.05	\sim 1.05	n.a.	\sim 520	\sim 500	[10]
					1.045				\sim 500	[14]

^a See text for details on source of geometric albedos.

^b Position uncertain due to discrepancies in overlapping spectra.

^c For spectra available only to 1.65 μm , the 1.8/0.56 μm reflectance ratio is calculated using reflectance at 1.65 μm ; band depth, FWHM, and band centers are likely minimum values due to lack of longer wavelength data; 0.7 μm peak position, band minimum, and center taken from tabulation by Burbine and Binzel (2002).

^d FWHM = full width at half maximum.

^e Data only available down to 0.8 μm , therefore 0.7 μm peak position is uncertain; band depth, FWHM, and band minima are likely maximum values due to lack of shorter wavelength data; reflectance at 0.8 μm used in place of unavailable 0.56 μm data for 1.8/0.56 μm reflectance ratio.

^f Values calculated from published spectra.

^g FWHM from Lucey et al. (1998).

^h Reflectance at 1.65 μm used for ratio and continuum for band depth, as longer wavelength data unavailable (SMASIR data).

ⁱ SMASIR plus 52 color survey (Bell et al., 1984) spectrum.

^j SMASIR plus SMASIR spectra to 2.5 μm .

^k SMASIR plus IRTF SPEX data.

^l FWHM after correction for temperature shown in italics (see text for details).

band in the 1 μm region and no 2 μm band, 766 Moguntia, 798 Ruth, and 1210 Morosovia. Their spectral properties suggest metal-dominated, olivine-bearing assemblages.

Reddy et al. (2011a) obtained reflectance spectra for a number of near-Earth asteroids (NEAs) that could serve as potential targets of a NEA spacecraft mission. Included in their targets was 1994CC (136617) which is an A-type triplet. Analysis of the spectra of this target indicated an olivine-rich object.

Sanchez et al. (2014) examined new and previously acquired reflectance spectra of 18 olivine-dominated asteroids. They distinguished two spectral classes – monomineralic olivine types (showing no absorption feature in the 2 μm region), and olivine-rich asteroids that exhibit a weak 2 μm feature. The monomineralic olivine asteroids had olivine composition ranging from \sim Fa₃₀ to Fa₅₁, consistent with brachinites and R chondrites. For the olivine-dominated asteroids they found olivine abundances ranging from 68% to 93%.

6.2. Approach to asteroid spectral analysis

A number of the spectral metrics discussed above for analysis of olivine + metal assemblages rely on the use of reflectance at certain wavelengths. However, for many asteroids, absolute reflectance may not be well known, and hence reliance on other metrics, such as reflectance ratios and band widths, is required. Where possible we applied all the available spectral metrics shown in Fig. 10 to help constrain individual asteroid surface properties (Fig. 13).

A potentially complicating factor in analysis of asteroid spectra is that other opaques, besides metal, could be present that would modify their spectra. This may include reddening npFe produced through space weathering. Our analysis of olivine + nanophase iron mixtures found darkening was more prevalent than reddening for the sizes of nanophase iron that we used (50 nm and 10 μm), as expected (Noble et al. (2007)). We analyze relevant asteroid spectra below to determine whether reddening beyond that associated with larger metal grains may be present, as well as whether reddening is more strongly present in shorter wavelength regions. Chromite is also a common and plausible accessory phase and we found that even a few percent of chromite will cause darkening and reddening, but also contribute an absorption band in the 2.2 μm region. Where available, we also look for evidence of minor

olivine absorption bands in the 0.4–0.7 μm region; these would be consistent with larger olivines (>45 μm). However, we note that the presence of metal will reduce the intensity of these bands.

The wavelength of the reflectance peak in the visible region was found to occur longward of 0.75 μm for very metal-rich assemblages, and we use this as an indicator of such assemblages in our asteroid spectral analysis. We use the absence of minor absorption bands in the 0.4–0.65 μm region as being indicative of either a very low Fa olivine, a substantial very fine-grained component (\ll 45 μm), or abundant metal. These options can be narrowed down by combining the lack of bands with derived olivine Fa content, reflectance, and metal abundance from the other spectral metrics. Finally, we also include the 1.3/1.05 μm band depth ratio of the asteroid spectra as a possible indicator of very large olivine grains or intact pallasite-like surfaces.

The fact that Fe²⁺-bearing phosphates are locally abundant in the Springwater pallasite, and that they exhibit a diagnostic absorption band near 2.3 μm , as well as an absorption feature near 1.9 μm if they are hydrated, opens the possibility of detecting phosphates on olivine \pm metal-rich asteroids. The 1 μm band of Fe²⁺-bearing phosphates overlaps that of olivine, and hence would be difficult to detect. An examination of the asteroid spectra included in this study failed to detect any unambiguous Fe²⁺-bearing phosphate-associated absorption features (i.e., feature near 2.3 μm). The lack of a 2.3 μm absorption band also argues for the absence of spectrally significant amounts of chromite (Cloutis et al., 2004).

6.3. Individual asteroids

The overall set of spectral metrics is useful for unraveling the relative contributions of grain size, reddening npFe, and macroscopic metal. We can use multiple metrics to assess asteroid spectra to determine their properties relative to our laboratory data, and constrain surface properties. In this section we examine individual asteroids that have been suggested as being olivine-rich. In the ensuing discussion, definitions of the relevant spectral asteroid taxonomic classes are presented in Table 4, while selected spectral properties of the individual asteroids are presented in Table 5. Selected orbital and derived surface assemblage properties are presented in Table 6. Possible meteorite analogues for individ-

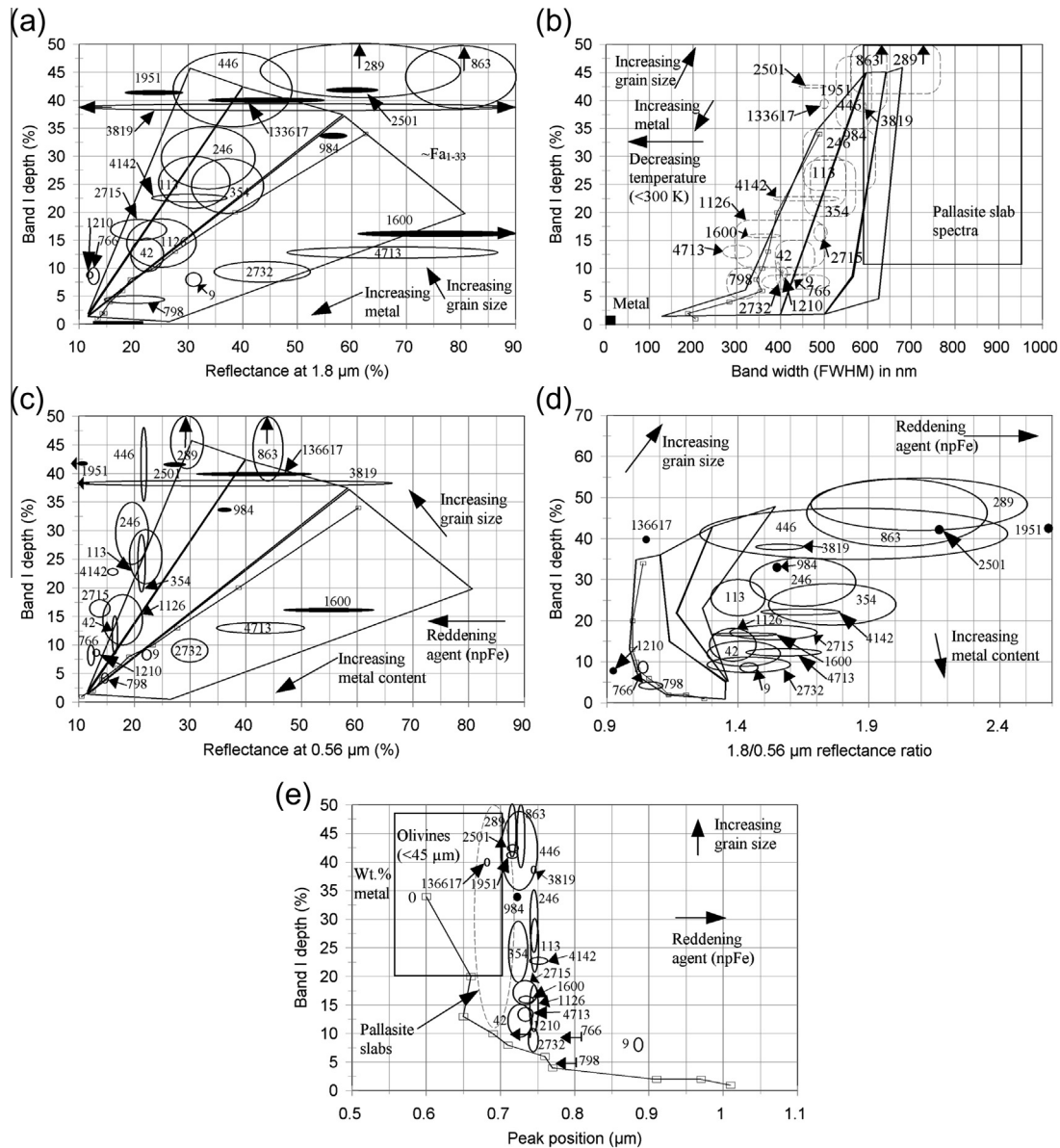


Fig. 13. Spectral parameters from Fig. 10 with superimposed points or fields for selected asteroids. (a) Reflectance at 1.8 μm versus band I depth. Reddening agents such as npFe cause little to no change in these parameters, as their effects are largely confined to reducing reflectance at shorter wavelengths and have little effect on band depth (Sasaki et al., 2001). Horizontal line at the bottom left corner of the plot represents reflectance range at 1.8 μm for metal powders. Uncertainties in geometric albedo and full range of determined values of reflectance at 1.8 μm were used to define the ellipses for the asteroids. Asteroids with a single value for 1.8 μm reflectance are indicated with filled ellipses. Asteroids with values that extend beyond the range of the plot (289 Nenetta, 863 Benkoela, 1600 Vyssotsky, and 3819 Robinson) are indicated with arrows at the edges of the plots. (b) Same as (a) for full width at half maximum for band I versus band I depth. Asteroids with multiple data points are shown with dashed line ellipses; 984 Gretia and 1951 Lick are indicated only by their numbers (single data point). Metal powders have a band depth and FWHM of zero. (c) Same as (a) for reflectance at 0.56 μm versus band I depth (using geometric albedo as a proxy for reflectance at 0.56 μm). Asteroids with multiple values are shown with ellipses. Asteroids with single values for band depth are shown with filled ellipses. Asteroids for which some data values extend outside the plotted range (289 Nenetta, 863 Benkoela, 1951 Lick, and 3819 Robinson) are indicated with arrows. (d) 1.8/0.56 μm reflectance ratio versus band I depth. Asteroids points or fields are indicated by their number; for asteroid spectra with limited data (<1.65 μm), band depth, 1.8/0.56 μm reflectance ratio, reflectance at 1.8 μm and FWHM likely represent lower limits; for asteroid spectra with no data available below \sim 0.8 μm , band depth, 1.8/0.56 μm reflectance ratio and FWHM likely represent lower limits. Change in these parameters as a function of grain size, increasing metal content, and reddening agent (nanophase iron) are indicated by arrows. (e) Same as (a) for visible region peak position versus band I depth. Data fields for asteroids are indicated by open ellipses; where lower wavelength spectral data are unavailable, upper limits on parameter values are indicated by a short vertical line and arrow pointing to the left (Asteroids 766 Moguntia, 798 Ruth, and 1210 Morosovia).

ual asteroids are presented in Table 7. Available individual asteroid spectra are provided in Fig. 14, continuum-removed spectra in Fig. 15, and visible region spectra in Fig. 16. For the visible region spectra, we searched specifically for absorption features at 0.4, 0.45, 0.495 and 0.63 μm (provided spectral coverage was available in these regions), as evidence of the presence of coarser-grained olivine. Asteroid albedos were acquired from the JPL Small-Body Database (JPL) (<http://ssd.jpl.nasa.gov/sbdb.cgi>) and other sources. In our analysis we used the most up-to-date albedos available.

6.3.1. 9 Metis (S1)

9 Metis has a geometric albedo of 0.213 ± 0.007 (Usui et al., 2011) and was classified as an S-type asteroid by Tholen (1984). It was included in the SMASSII survey (0.435–0.925 μm) of Bus and Binzel (2002) and the MIT-UH-IRTF Joint Campaign for NEO Spectral Reconnaissance (<http://smass.mit.edu/minus.html>), hereafter MINUS survey. In their spectroscopic survey of S-asteroids, Gaffey et al. (1993) did not classify Metis into an S-subtype because its 1 μm region absorption band plotted outside the S(II)

Table 6

Selected orbital and physical properties and derived compositional information for the asteroids included in this study. Orbital data, diameters, rotation periods, and geometric albedos are from the JPL Small Bodies Node (<http://ssd.jpl.nasa.gov/sbdb.cgi>; accessed February 20, 2014).

Asteroid	Eccentricity (e)	Semi-major axis (AU)	Inclination (°)	Diameter (km)	Rotation period (h)	Metal content (wt.%)	Fa content ^a	Evidence of larger olivine ^b	Evidence of accessory phases ^c
9 Metis	0.122	2.39	5.6	190	5.1	50 ± 10	Low–medium	n.a.	No?
42 Isis	0.222	2.44	8.5	100.2	13.6	30 ± 10	Low	Yes	No
113 Amalthea	0.086	2.36	5.0	46.1	9.9	20 ± 10	Low–medium	Yes	Yes
246 Asporina	0.110	2.69	15.6	60.1	16.2	20 ± 10	Low–medium	Yes	No
289 Nenetta	0.205	2.87	6.7	33.7	6.9	15 ± 10	Medium–high	Yes	No
354 Eleonora	0.115	2.80	18.4	155.2	4.3	20 ± 10	Low	Yes	Yes?
446 Aeternitas	0.127	2.79	10.6	45.4	15.7	10 ± 10	Low–high	Yes	Yes
766 Moguntia	0.095	3.02	10.1	31.3	4.8	40 ± 20	Low–medium	No	Yes?
798 Ruth	0.039	3.01	9.2	43.2	8.5	60 ± 15	Medium	n.a.	Yes
863 Benkoela	0.031	3.21	25.4	27.1	7.0	5 ± 5	Low–medium	No?	Yes
984 Gretia	0.198	2.8	9.1	31.9	5.8	5 ± 5	Low	Yes?	Yes
1126 Otero	0.147	2.27	6.5	12.0	3.6	20 ± 10	n.a.	Yes?	Yes
1210 Morosovia	0.060	3.01	11.3	33.6	15.3	40 ± 10	Low	n.a.	Yes?
1600 Vyssotsky	0.037	1.85	21.2		3.2	15 ± 10	Low	No?	n.a.
1951 Lick	0.061	1.39	39.1	5.6	5.3	5 ± 5	High	No?	No
2501 Lohja	0.196	2.42	3.3		3.8	5 ± 5	Low–medium	Yes?	Yes
2715 Mielikki	0.153	2.74	6.7	13.1	33.6	20 ± 10	Low	Yes?	n.a.
2732 Witt	0.024	2.76	6.5			20 ± 15	n.a.	No	Yes
3819 Robinson	0.136	2.77	11.1			5 ± 5	Low	Yes?	Yes
4142 Dersu-Uzala	0.151	1.91	26.5		140	20 ± 15	Low	No?	Yes
4713 Steel	0.074	1.93	22.7		5.2	n.a.	n.a.	No?	Yes
133617	0.417	1.64	4.7	~0.65	2.3	10 ± 10	Low	n.a.	n.a.

n.a.: data not available or too noisy to make a determination.

^a Fa content assigned as low (~Fa_{0–33}), medium (~Fa_{34–67}), or high (~Fa_{68–100}).

^b Evidence of larger olivine (<45 μm versus <<45 μm) largely based on presence or absence of minor olivine absorption bands in the 0.4–0.5 μm region and near 0.63 μm and location of appropriate spectral parameters in Fig. 13.

^c Evidence of accessory phases largely based on presence or absence of an absorption feature in the 2 μm region and/or a band minimum or band center outside of the range expected for olivine + metal assemblages.

region, suggestive of some calcic pyroxene. It was included in the SMASSIR survey of Burbine and Binzel (2002), visible region spectra were measured by Sawyer (1991) and 52 color spectra were acquired by Bell et al. (1988) and Kelley and Gaffey (2000), who proposed a genetic link with 113 Amalthea on the basis of nearly identical silicate compositions. The Bell et al. (1988) spectrum shows a possible 1.9 μm region absorption band, which is not seen in the spectrum of Kelley and Gaffey (2000), who suggested that this feature may be due to telluric water. Both sets of 52 color spectra show a modestly red-sloped spectrum below ~1.6 μm and an olivine-like absorption band in the 1 μm region. The band center for Metis ranges between 1.062 and 1.085 μm in these spectra (Kelley and Gaffey, 2000). The low intensity of the 1 μm absorption band led Kelley and Gaffey (2000) to suggest an assemblage of 40–50% FeNi metal and 50–60% olivine, with little or no (<5%) pyroxene. Clark (1995) modeled the reflectance spectrum of Metis as 47–56% metal + sulfide, 41–47% olivine, and 3–5% clinopyroxene.

Two merged spectra and continuum-removed spectra are shown in Figs. 14a, b and 15a, b, respectively SMASS + 52 color survey and SMASS + SMASSIR. The spectra are characterized by a broad olivine-like absorption band. The spectral properties of Metis are most consistent with a low to medium-Fa olivine with abundant macroscopic metal (50 ± 10 wt.%), mostly on the basis of 0.7 μm peak position, band depth, and 1.8–2.4 μm slope, and significant spectral reddening due to npFe, in agreement with previous interpretations. Wavelength coverage in the visible region is not available for detecting Fe spin-forbidden bands. On this basis, Metis is most closely related to pallasites.

6.3.2. 42 Isis (S1)

Isis has a geometric albedo of 0.16 ± 0.005 (Usui et al., 2011). It was classified as an S(I) asteroid by Gaffey et al. (1993) on the basis of having a 1 μm band center consistent with olivine. It was included in the SMASSII survey (0.435–0.925 μm) of Bus and Binzel (2002), and the SMASSIR survey (0.9–1.65 μm) of Burbine and Binzel (2002) and was assigned to their L class (Table 4). The

Table 7

Possible meteorite analogues to asteroids included in this study.

Asteroid	Plausible meteorite analogues
9 Metis	Pallasites
42 Isis	Olivine-rich pallasites
113 Amalthea	Olivine-rich, pyroxene-bearing pallasites
246 Asporina	Olivine-rich pallasites
289 Nenetta	Brachinites, LEW/MIL/NWA meteorites
354 Eleonora	Olivine-rich pallasites
446 Aeternitas	R chondrites, olivine-diogenites
766 Moguntia	Pallasites, olivine diogenites, ureilites, R chondrites, H6, CV3, CM2, R chondrite
798 Ruth	Pallasites, CB chondrites, CV3
863 Benkoela	Olivine diogenites, LEW/MIL/NWA meteorites
984 Gretia	Olivine diogenites, LEW/MIL/NWA meteorites
1126 Otero	Angrites?
1210 Morosovia	Pallasites
1600 Vyssotsky	Olivine-rich pallasites
1951 Lick	R chondrites, brachinites, LEW/MIL/NWA meteorites
2501 Lohja	R chondrites, olivine diogenites
2715 Mielikki	Olivine-rich pallasites
2732 Witt	Pallasites, lodranites?
3819 Robinson	R chondrites, brachinites, LEW/MIL/NWA meteorites
4142 Dersu-Uzala	R chondrites
4713 Steel	n.a.
136617	Brachinites, LEW/MIL/NWA meteorites

Notes: pallasites are assumed to have metal abundances of ~25–75 wt.%; IAB and IIIICD irons are assumed to have metal abundances >70%.

Meteorite groups in italics are assignments made in previous studies – see text for details.

n.a.: insufficient data available to assign a meteorite class.

published spectrum shows a broad band near 1.05 μm and gradually rising reflectance to at least 1.65 μm. The spectrum of Isis presented by Gaffey et al. (1993) shows a red-sloped spectrum below ~1.5 μm, and a broad olivine-like absorption feature in the 1 μm region.

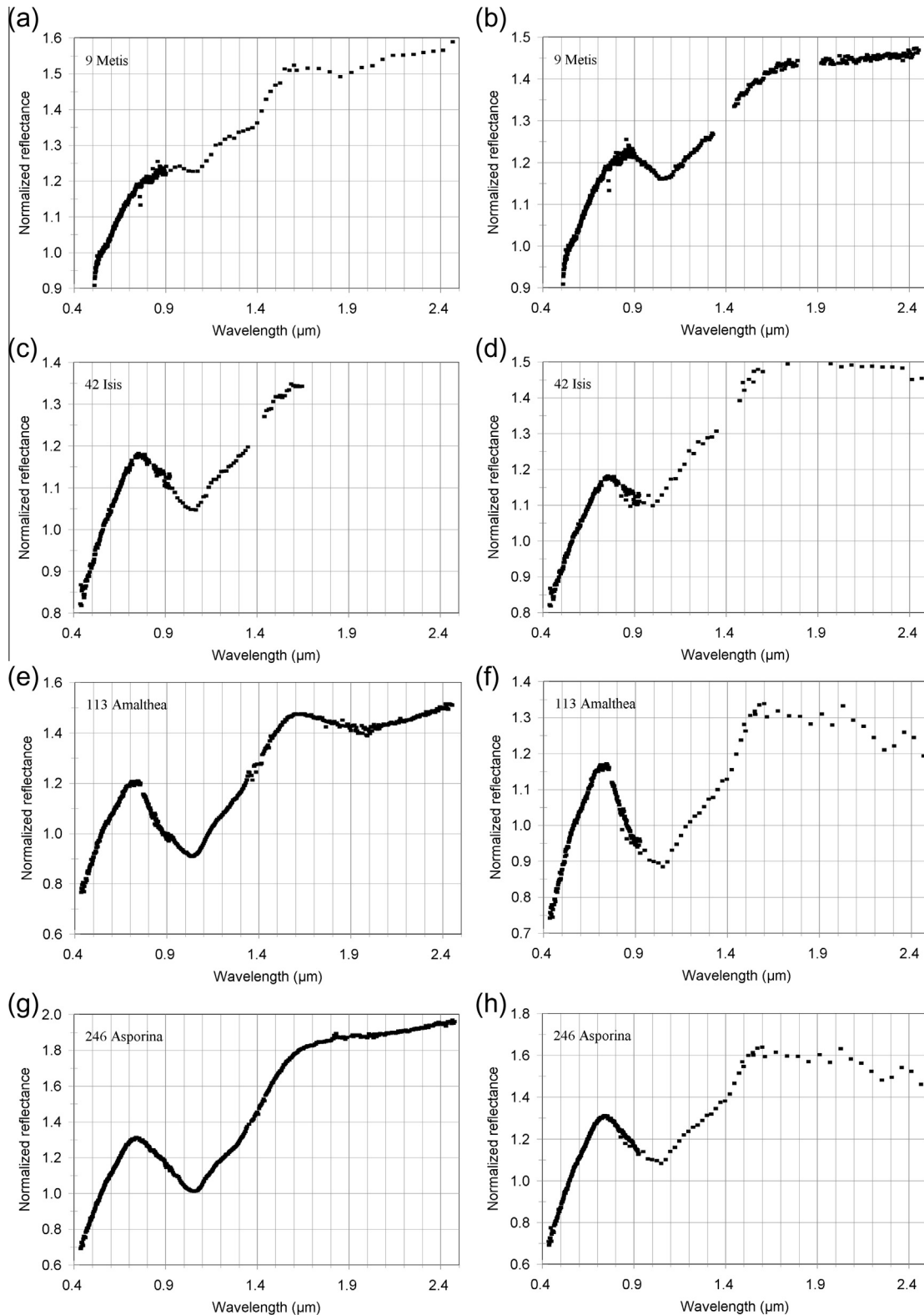


Fig. 14. Normalized reflectance spectra of olivine-rich asteroids from the literature. See text for details. (a and b) 9 Metis. (c and d) 42 Isis. (e and f) 113 Amalthea. (g and h) 246 Asporina. (i and j) 289 Nenetta. (k and l) 354 Eleonora. (m and n) 446 Aeternitas. (o) 766 Moguntia. (p) 789 Ruth. (q and r) 863 Benkoela. (s) 984 Gretia. (t and u) 1126 Otero. (v and w) 1210 Morosovia. (x) 1600 Vyssotsky. (y) 1951 Lick. (z) 2501 Lohja. (aa) 2715 Mielikki. (ab) 2732 Witt. (ac, ad and ae) 3819 Robinson. (af and ag) 4142 Dersu-Uzala. (ah) 4713 Steel. (ai) 136617 (1994CC).

Two merged spectra (SMASS + SMASSIR and SMASS + 52 color data) and continuum-removed spectra are shown in Figs. 14c, d and 15c, d, respectively. The spectra are characterized by a broad

absorption band with a minimum near 1.05 μm , and flat reflectance beyond $\sim 1.65 \mu\text{m}$. The long wavelength wing of the olivine absorption is apparent near 1.3 μm in the continuum-removed

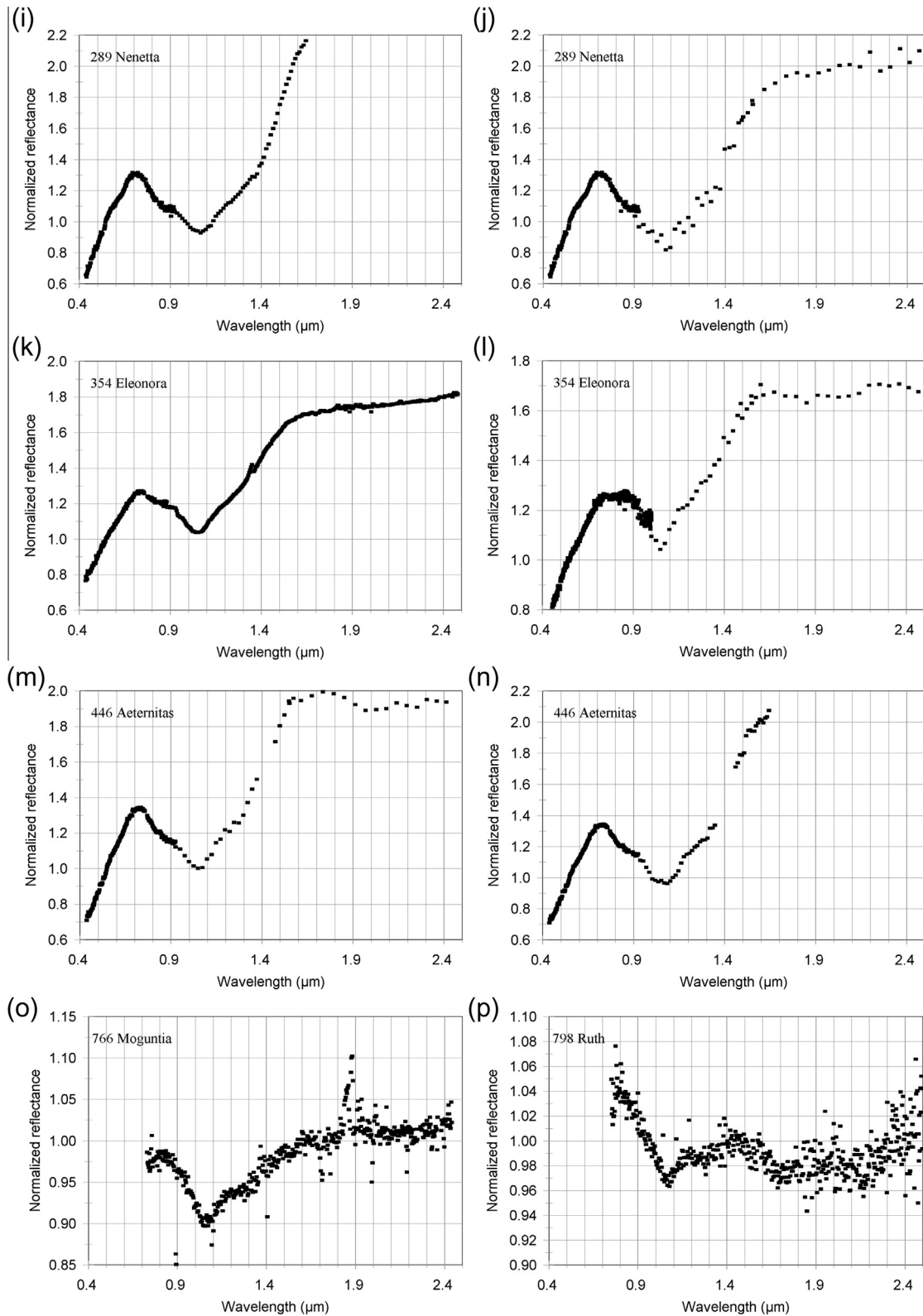


Fig. 14 (continued)

spectra. There are suggestions of minor olivine Fe^{2+} spin forbidden bands near 0.450 and 0.495 μm , and a possible additional band near 0.63 μm (Fig. 16a), suggesting that the surface is not composed exclusively of ultra fine-grained ($\ll 45 \mu m$) olivine. There is

no evidence of a pyroxene band in the 2 μm region. The spectral properties of Isis (Table 5) are most consistent with a low-Fa olivine (band center), some larger grain-size fraction (presence of absorption bands near 0.450 and 0.495 μm), $\sim 30 \pm 10$ wt.% macro-

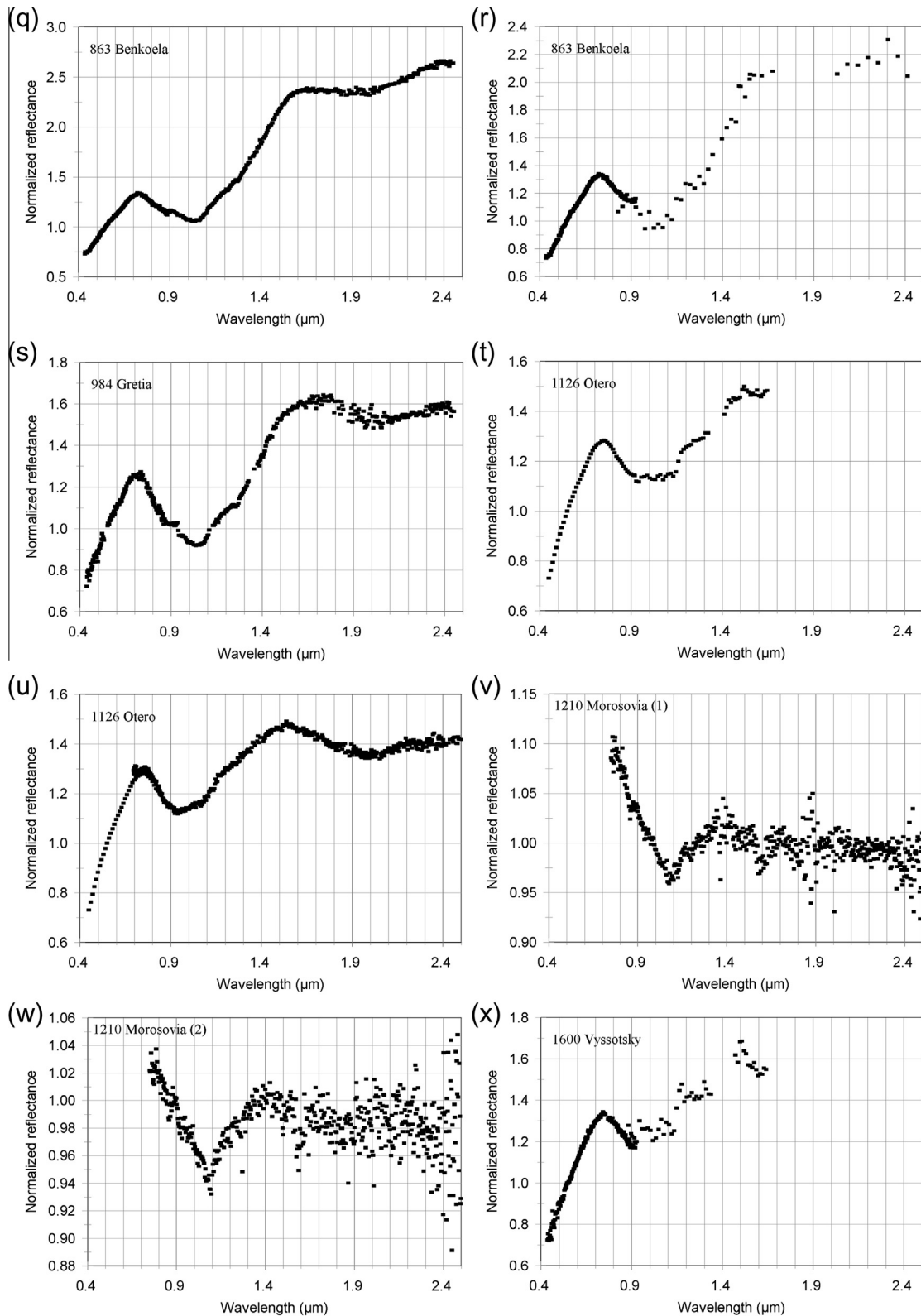


Fig. 14 (continued)

scopic metal (band depth, 1.8 μm reflectance, and low 2.4/1.8 μm ratio), and some reddening npFe (0.56 μm reflectance, 1.8/0.56 μm reflectance ratio, 0.7 μm peak position, and 2.4/1.8 versus 1.8/0.56 μm reflectance ratio: Fig. 12e). On this basis, Isis is most closely related to olivine-rich pallasites.

6.3.3. 113 Amalthea (S1)

Amalthea has a geometric albedo of 0.22 ± 0.03 (Masiero et al., 2011a, 2011b). It was included in the SMASSII survey (0.435–0.925 μm) of Bus and Binzel (2002) and the MINUS survey, and assigned to the S class (Table 4). Both Amalthea spectra (Fig. 14e

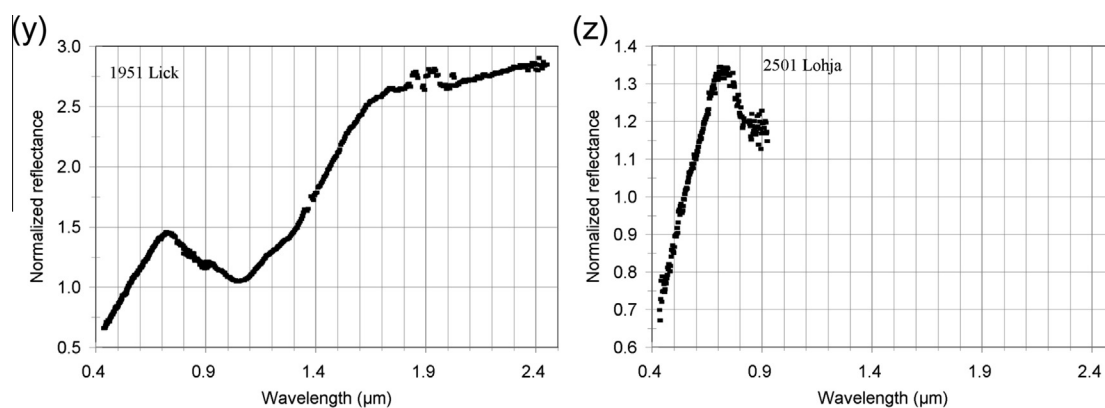


Fig. 14 (continued)

and f) show a well-defined olivine absorption band in the 1 μm region and an additional absorption feature in the 2 μm region. The Amalthea spectrum presented in Gaffey et al. (1993) shows a red-sloped spectrum below $\sim 1.6 \mu\text{m}$, a well-defined olivine absorption feature and a possible weak pyroxene band ($\sim 4\%$ deep) centered near 1.97 μm (Fig. 14e and f). The influence of pyroxene probably also accounts for the center of the 1 μm region absorption band being located just shortward of the olivine field ($\sim 1.04 \mu\text{m}$; Fig. 15e and f). Weak bands near 0.450 and 0.495 μm , and possibly 0.63 μm , indicative of coarser olivine, may be present (Fig. 16b).

The presence of pyroxene impacts our ability to constraint olivine Fa content, but is likely low Fa on the basis of its 1.8 μm reflectance. Its spectral properties suggest a lower macroscopic metal content than Isis ($\sim 20 \pm 10 \text{ wt.}\%$; based largely on band depth and absolute reflectance), some portion of a coarser size fraction ($>45 \mu\text{m}$, based on the presence of minor absorption bands), and reddening npFe (based on 1.8/0.56 μm versus 2.4/1.8 μm reflectance ratio). Hiroi et al. (1992) modeled the spectrum of Amalthea as a mixture of specular (2.9%) and diffuse (76.4%) spectra of a slab of the Y-8451 pallasite and olivine grains in a slab of Imilac (20.6%). The higher olivine content suggested by the spectral matching versus a “regular” pallasite is broadly consistent with the low metal content from our analysis and is plausibly related to an olivine-rich (pyroxene-bearing) pallasite (Table 7). Its band area ratio suggests $<10 \text{ wt.}\%$ pyroxene. We infer that the olivine is likely low to medium Fa.

6.3.4. 246 Asporina (A)

Asporina has a geometric albedo of 0.20 ± 0.03 (Masiero et al., 2011a, 2011b). It was included in the SMASSII survey (0.435–0.925 μm) of Bus and Binzel (2002) and the MINUS survey and assigned to the A class (Table 4). Cruikshank and Hartmann (1984) acquired a 0.75–2.6 μm spectrum of Asporina and merged it with a 0.3–0.97 μm spectrum from Chapman and Gaffey (1979). Their combined spectrum shows a broad 1 μm absorption feature and no apparent absorption in the 2 μm region. They interpreted the spectrum as indicating $<10\%$ pyroxene and plagioclase, and a mix of coarse and fine-grained olivine. They infer the presence of metal from the strength of the olivine absorption and red spectral slope, and derive an areal abundance of one-third metal and two-thirds olivine, with a composition of Fa₁₀ to Fa₄₀. In contrast, the 52 color spectrum of Asporina (Bell et al., 1988) shows a possible absorption band in the 2 μm region, but its shape is not fully consistent with a single pyroxene. The lower signal to noise ratio of the MINUS data suggests that the 2 μm region features in the 52 color data are likely attributable to noise.

Sunshine and Pieters (1998) applied MGM analysis to Asporina to obtain an olivine composition of Fa₂₀. Lucey et al. (1998) analyzed a spectrum of Asporina and derived an olivine composition

of Fa_{0–10}. Asporina was observed by Reddy et al. (2005) who determined that the temperature corrected olivine composition was Fa_{20–60}. Sunshine et al. (2007) derived an olivine composition of \sim Fa₄₀. This spectrum also shows a possible weak pyroxene absorption feature in the 2 μm region. Hiroi et al. (1992) modeled the spectrum of Asporina as a mixture of a specular spectrum of a slab of the Y-8451 pallasite (15.7%) and olivine grains in a slab of Imilac (84.3%), and also suggested the presence of reddening npFe.

The SMASS + MINUS and SMASS + 52 color spectra are shown in Fig. 14g and h, and are similar to the spectrum of Cruikshank and Hartmann (1984), exhibiting a broad olivine-like absorption band on a red-sloped spectrum and no clear evidence of a 2 μm region pyroxene absorption band. Coarser olivine-associated absorption bands may be present near 0.45, 0.495 and 0.63 μm (Fig. 16c). Our interpretation of the Asporina spectra suggest a medium Fa content olivine (based on band center; Fig. 15g and h), $\sim 20 \pm 10 \text{ wt.}\%$ macroscopic metal, some reddening npFe, and some portion of a coarser-grained fraction. The olivine compositional determination is consistent with the results of Sunshine et al. (2007) and Sanchez et al. (2014). The assemblage derived by Hiroi et al. (1992) suggests a lower metal content than our analysis, although the relevance of a specular slab measurement to a powdered sample is uncertain. The 2.4/1.8 μm versus 1.8/0.56 μm reflectance ratios and 0.7 μm peak position all suggest npFe-associated spectral reddening. Its derived mineralogy is broadly consistent with pallasites (Table 7).

6.3.5. 289 Nenetta (A)

Cruikshank and Hartmann (1984) acquired 0.75–2.6 μm spectra of Nenetta. While their shorter wavelength data were noisy and incomplete, there seemed to be a broad absorption band centered near 1.05 μm , and no strong absorption features in the 2 μm region. They interpreted the spectrum as indicating $<10\%$ pyroxene and plagioclase, with the olivine being coarser than on Aeternitas. They also inferred that Nenetta has a higher olivine/metal ratio than Aeternitas, for which they had derived an abundance of one-third metal and two-thirds olivine, with a composition of Fa₂₀ to Fa₆₀. Sunshine et al. (1998, 2007) applied MGM analysis to a spectrum of Nenetta and derived an olivine composition of Fa_{30–40}. Lucey et al. (1998) analyzed a spectrum of Nenetta and derived an olivine composition of Fa_{0–10}.

Nenetta has a geometric albedo of 0.29 ± 0.03 (Usui et al., 2011). It was included in the SMASSII survey (0.435–0.925 μm) of Bus and Binzel (2002) and the SMASSIR survey (0.9–1.65 μm) of Burbine and Binzel (2002) and assigned to the A class (Table 4). The SMASS + SMASSIR and SMASS + 52 color spectra (Fig. 14i and j) both exhibit an olivine-like absorption band with a minimum near 1.05 μm and a red-sloped spectrum up to 2.5 μm . There is good evidence of olivine-associated absorptions near 0.450, 0.495 and

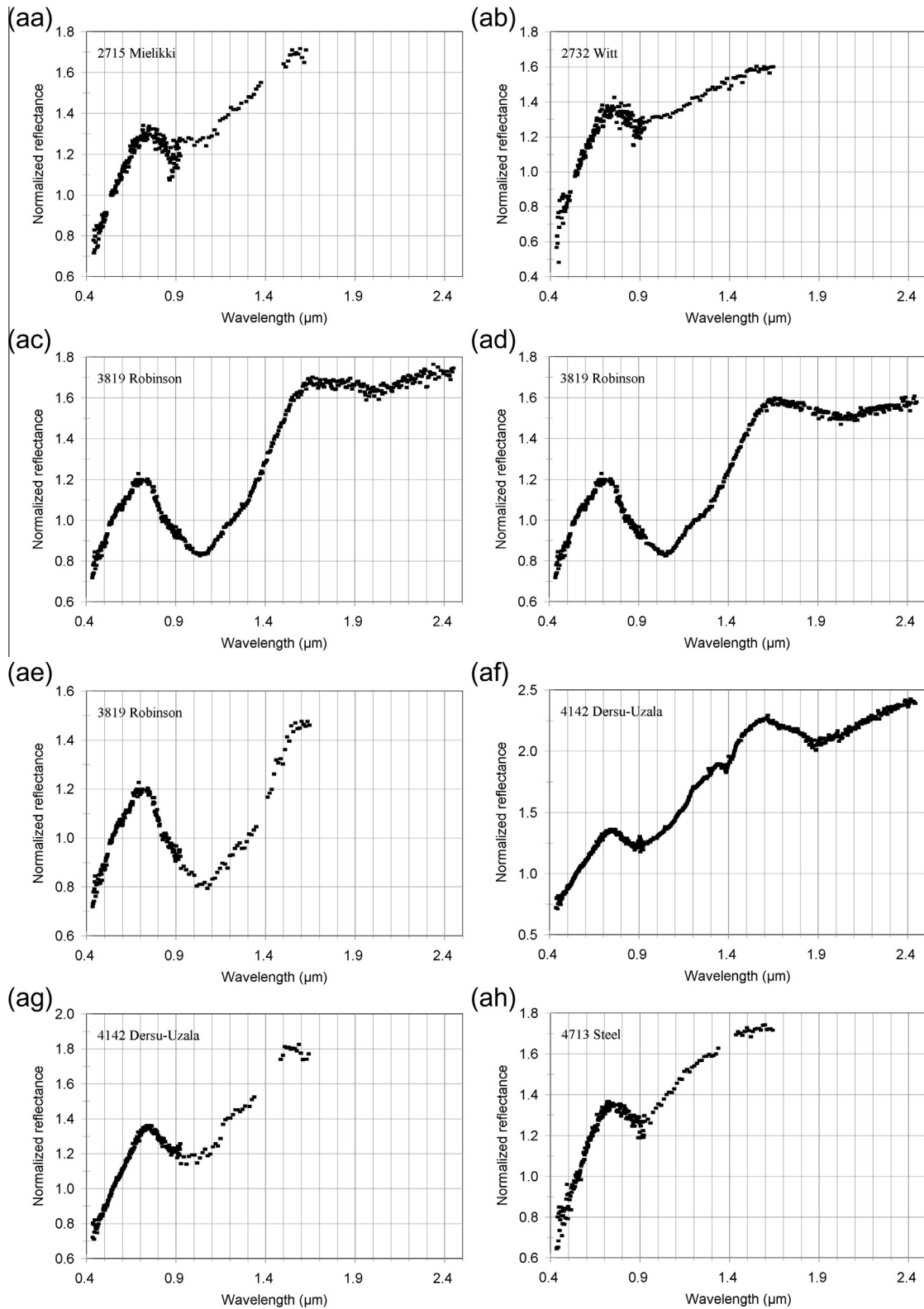


Fig. 14 (continued)

0.65 μm (Fig. 16d), suggesting a coarser fraction, and no clear evidence of a pyroxene band in the 2 μm region. The presence of visible region absorption bands and band depths versus geometric albedo are consistent with a medium to high Fa olivine, and somewhat coarser-grained assemblage than many of the other asteroid spectra. The albedo of Nenetta, coupled to high band depth, sug-

gests medium to high Fa content olivine and low macroscopic metal content ($< \sim 15 \pm 10$ wt.%). Its band center ($\sim 1.07\text{--}1.09$ μm) is consistent with medium to high Fa content (in agreement with the results of Sunshine et al. (2007) and Sanchez et al. (2014)), and a low macroscopic metal content (Fig. 15i and j). Its spectral slope suggests the presence of appreciable reddening npFe. Plausi-

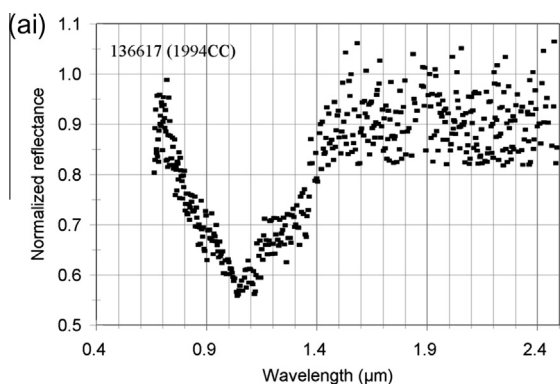


Fig. 14 (continued)

ble spectral matches include brachinites and various ungrouped LEW, MIL and NWA meteorites (Table 7).

6.3.6. 354 Eleonora (S1)

Eleonora has a geometric albedo of 0.211 ± 0.007 (Usui et al., 2011). It was included in the SMASSII survey (0.435–0.925 μm) of Bus and Binzel (2002) and the MINUS survey and assigned to the S1 class (Table 4). The Eleonora spectrum presented in Gaffey et al. (1993) shows a red-sloped spectrum below $\sim 1.6 \mu\text{m}$, a well-defined olivine absorption feature and a possible weak 2 μm region band. Mothé-Diniz et al. (2000) acquired 0.49–0.92 μm spectra of 354 Eleonora. These spectra do not show clear evidence of visible region absorption bands. The spectra do show a possible broad weak band near 0.83 μm which is likely attributable to the short wavelength olivine absorption band (Sunshine and Pieters, 1998).

The combined SMASS + MINUS and SMASS + 52 color spectra are both red-sloped below $\sim 1.6 \mu\text{m}$ and close to flat beyond that, and dominated by the 1 μm region olivine absorption feature (Fig. 14k and l). Any 2 μm pyroxene band, if present, is weak. It appears to have weak 0.450 and 0.495 μm possible olivine absorption bands, but no band near 0.63 μm (Fig. 16e). Eleonora's spectra are consistent with some reddening npFe (1.8/0.56 μm versus 2.4/1.8 μm reflectance ratios), as also suggested by Hiroi et al. (1992), and a coarser size fraction (not all $< 45 \mu\text{m}$) being present (visible region absorption bands). Previous band center determinations are variable, but most are consistent with a low to medium Fa olivine (Sunshine et al., 2007; Sanchez et al., 2014) (Fig. 15k and l). Metal content is on the order of $20 \pm 10 \text{ wt.}\%$ on the basis of band depth, albedo, and 2.4/1.8 μm ratio. Hiroi et al. (1992) modeled the spectrum of Eleonora as a mixture of specular (8.0%) and diffuse (47.1%) spectra of a slab of the Y-8451 pallasite and olivine grains in a slab of Imilac (45.0%). Gaffey et al. (2014) modeled reflectance spectra of Eleonora as an intimate mixture of fine-grained olivine ($\sim 60\text{--}70\%$, $\sim \text{Fa}_{30 \pm 11}$), and low nickel metal, with a small component ($\sim 8\text{--}10\%$) of igneous pyroxene (weakly constrained at $\sim \text{Fs}_{50}\text{Wo}_{10}$). The higher olivine content based on the spectral matching versus a “regular” pallasite is broadly consistent with the low metal content of our analysis. The best meteorite analogue for Eleonora is an olivine-rich pallasite.

6.3.7. 446 Aeternitas (A)

Aeternitas has a geometric albedo of 0.222 ± 0.006 (Usui et al., 2011). It was included in the SMASSII survey (0.435–0.925 μm) of Bus and Binzel (2002) and the SMASSIR survey (0.9–1.65 μm) of Burbine and Binzel (2002) and assigned to the A class (Table 4). Bell et al. (1984) determined that this asteroid is dominated by olivine with a minor ($\sim 5\%$) pyroxene component on the basis of a weak 2 μm region absorption band. They noted that the spectrum is redder than for pure forsteritic olivine, indicating either a more

fayalitic olivine or the presence of metal. Cloutis et al. (1990) attempted to fit the 52 color survey spectrum of Aeternitas (Bell et al., 1988) using a number of possible end member spectra and linear mixing. The best fit consisted of 35% metal, 55% olivine ($\text{Fa}_{10\text{--}30}$), 7% high-calcium pyroxene, and 3% low-calcium pyroxene, with a substantial fine-grained component. Hiroi and Sasaki (2001) modeled the spectrum of Aeternitas as a mixture of 2% fresh olivine, 93% space-weathered olivine, 1% space-weathered orthopyroxene, and 4% chromite. Hiroi et al. (1992) modeled the spectrum of Aeternitas using a mixture of a specular spectrum of a slab of the Y-8451 pallasite (8.7%) and olivine embedded in a slab of the Imilac pallasite (91.3%); the relevance of these slab measurements to what is likely a powdered asteroid surface is uncertain, but suggests an olivine-rich body. They also suggested that some reddening npFe was required to improve the spectral match. Lucey et al. (1998) analyzed a spectrum of Aeternitas and derived an olivine composition of $\text{Fa}_{0\text{--}10}$. Sasaki et al. (2002) were able to provide an excellent fit to Aeternitas using a mixture of $< 75 \mu\text{m}$ size unirradiated and laser irradiated olivine, plus minor pyroxene and chromite. Reddy et al. (2005) presented new spectra (0.8–2.5 μm) of Aeternitas and found a weak ($\sim 5\%$ deep) band near 2 μm in one of their spectra, suggesting the presence of minor pyroxene. After correcting for temperature, they determined olivine composition to be $\text{Fa}_{10\text{--}50}$. Sunshine et al. (2007) determined that the olivine on Aeternitas is magnesian.

The two reflectance spectra of Aeternitas (Fig. 14m and n) are broadly similar, being dominated by olivine, red-sloped below $\sim 1.8 \mu\text{m}$, flat beyond $\sim 1.8 \mu\text{m}$, and with a possible weak pyroxene band in the 2 μm region in the 52 color spectrum. Any visible region absorption bands, if present, are weak, and may possibly be present near 0.455, 0.500, and 0.63 μm , the former two bands being somewhat offset from the expected positions for olivine (Fig. 16f). A surface dominated by fine-grained material ($< 45 \mu\text{m}$ but not $\ll 45 \mu\text{m}$) is suggested by the weakness of any visible region absorption bands and relatively high albedo (0.22), but some fraction of coarser material is suggested by its band depth versus 0.56 μm reflectance. The amount of pyroxene that has been inferred to be present ($\sim 8\%$, Sanchez et al., 2014), has little effect on olivine absorption band position (Cloutis et al., 1986). Derived band centers are variable, spanning the range from low to high Fa content olivine (Fig. 15m and n). Reddening npFe is suggested by its very red spectral slope. Multiple spectral parameters suggest a low macroscopic metal content ($10 \pm 10 \text{ wt.}\%$). A number of plausible meteorites can be suggested if a 2 μm region absorption band is present (Table 7). The best meteorite analogues would be olivine-rich, low-metal or metal-free meteorites with minor pyroxene, such as R chondrites, olivine-diogenites, and pyroxene-bearing pallasites.

6.3.8. 766 Moguntia (MU)

Moguntia has a geometric albedo of 0.124 ± 0.007 (Usui et al., 2011). Birlan et al. (2007) obtained 0.8–2.5 μm spectra of Moguntia and found that it has a slightly positive slope with a shallow large band around 1 μm and no discernible band in the 2 μm region. They found best spectral matches to various mafic silicate-bearing meteorites, such as H6, CV3 and CM2 chondrites. However, only a CV3 chondrite is plausibly consistent with the apparent spectral dominance of olivine in Moguntia's spectrum. Their spectral modeling suggests a surface of pure olivine of composition between Fa_{21} and Fa_{33} or $\text{Fa}_{50\text{--}60}$. They noted that a neutral phase is probably present to account for reduced band depth. They also note that the 1 μm region absorption band is similar to that of Asteroid 221 Eos, but with slope differences that they suggest may be due to space weathering.

The published spectrum shows that the 1 μm feature has a depth of $\sim 7\%$ and a FWHM of $\sim 300 \text{ nm}$. Birlan et al. (2007) determined that the main olivine absorption band is centered at

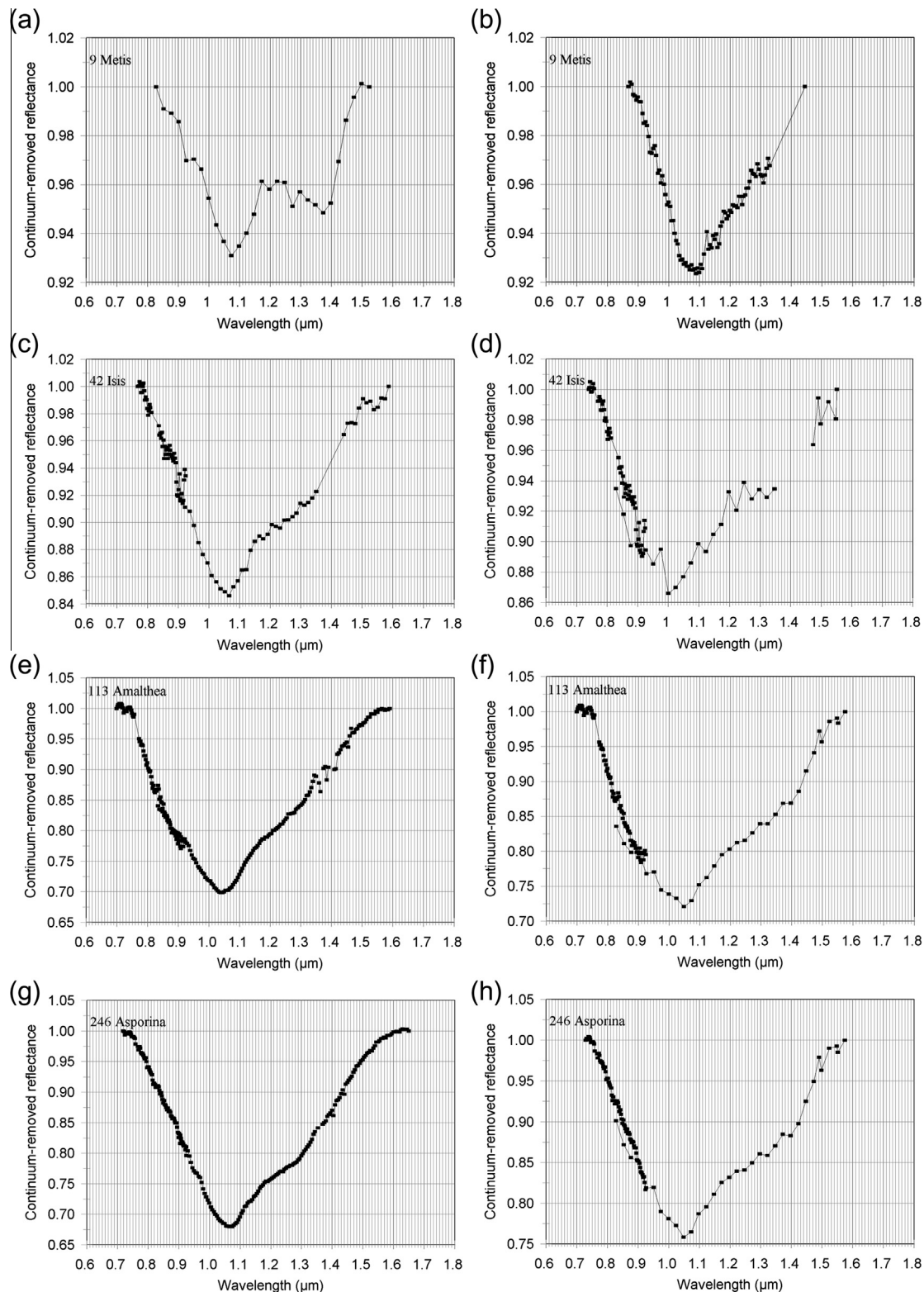


Fig. 15. Straight line continuum-removed reflectance spectra of some of the asteroid spectra shown in Fig. 14. (a and b) 9 Metis. (c and d) 42 Isis. (e and f) 113 Amalthea. (g and h) 246 Asporina. (i and j) 289 Nenetta. (k and l) 354 Eleonora. (m and n) 446 Aeternitas. (o and p) 863 Benkoela. (q) 984 Gretia. (r and s) 1126 Otero. (t) 1600 Vyssotsky. (u) 1951 Lick. (v) 2715 Mielikki. (w) 2732 Witt. (x, y and z) 3819 Robinson. (aa and ab) 4142 Dersu-Uzala. (ac) 4713 Steel. (ad) 136617 (1994CC).

1.051 μm . [Mothé-Diniz et al. \(2008\)](#) acquired 0.8–2.5 μm spectra of Moguntia, and their published spectrum shows an olivine-like absorption feature near 1.05 μm , a peak near 1.55 μm , and a slightly blue-sloped, featureless spectrum toward longer wavelengths. Their closest spectral match was to an R chondrite.

[Hardersen et al. \(2011\)](#) also acquired reflectance spectra of Moguntia, and determined that it has a band center of 1.068 μm , a depth of $\sim 10\%$ and olivine composition of $\text{Fa}_{\sim 40}$. The available spectra (Fig. 14o) suggest a band minimum of $\sim 1.08 \mu\text{m}$ and a peak near 0.8 μm . The continuum removed band center is near 1.07 μm ;

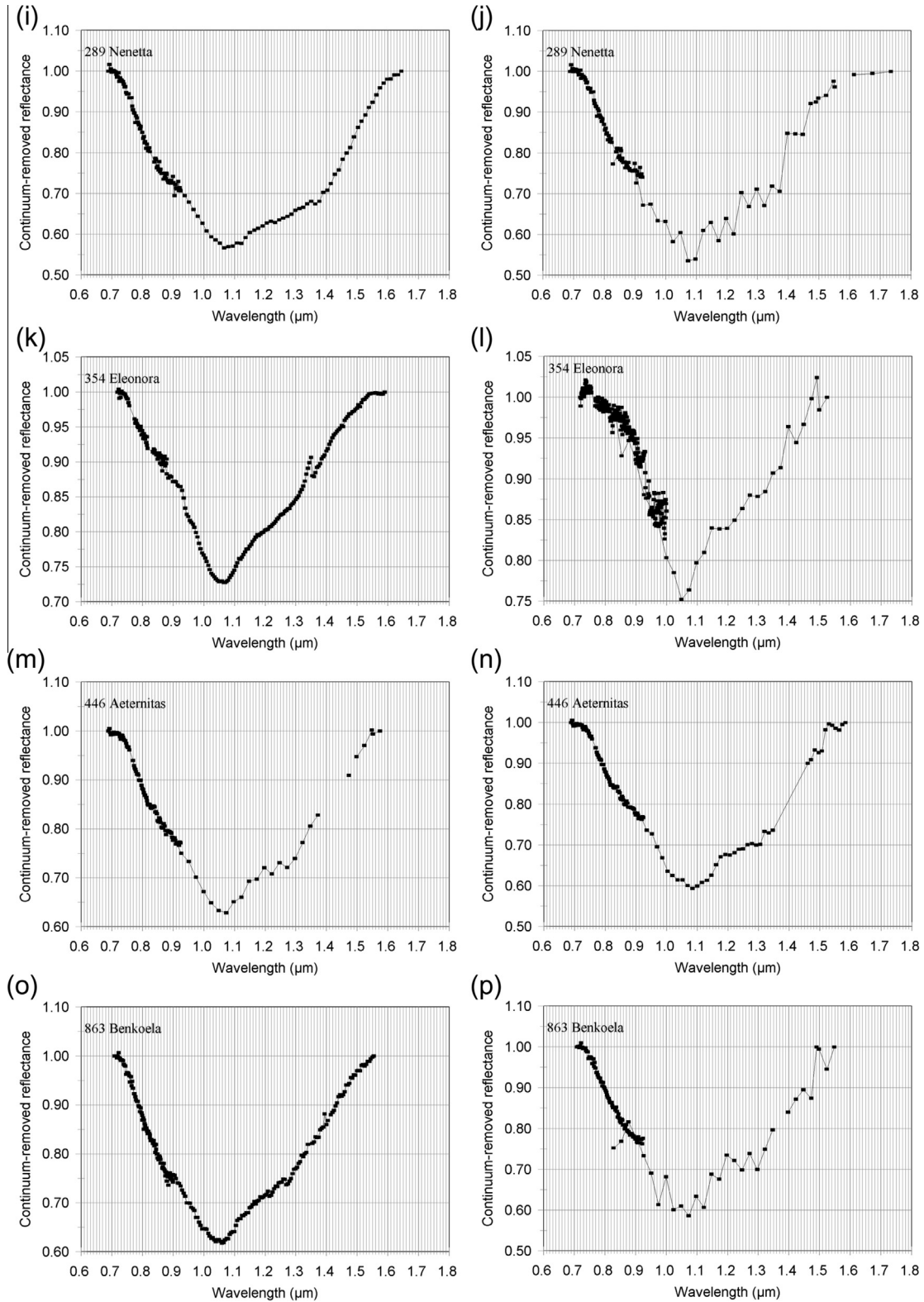


Fig. 15 (continued)

this is consistent with olivine, and the dominance of olivine is also indicated by the presence of an inflection near 1.25 μm. There may be a slight pyroxene band in the 2 μm region. The band center of Moguntia is somewhat uncertain but suggests low or medium Fa olivine (Table 5). Its low albedo is consistent with some darkening metal. There is no evidence of significant npFe-associated reddening, and macroscopic metal content is consistently 40 ± 20 wt.%. Its

low albedo, poorly constrained olivine composition, and possible 2 μm region absorption band open the possibility of multiple plausible meteorite analogues (Table 7).

6.3.9. 798 Ruth (MU)

Ruth has a geometric albedo of 0.148 ± 0.005 (Usui et al., 2011). Mothé-Diniz et al. (2008) acquired 0.8–2.5 μm spectra of Ruth, and

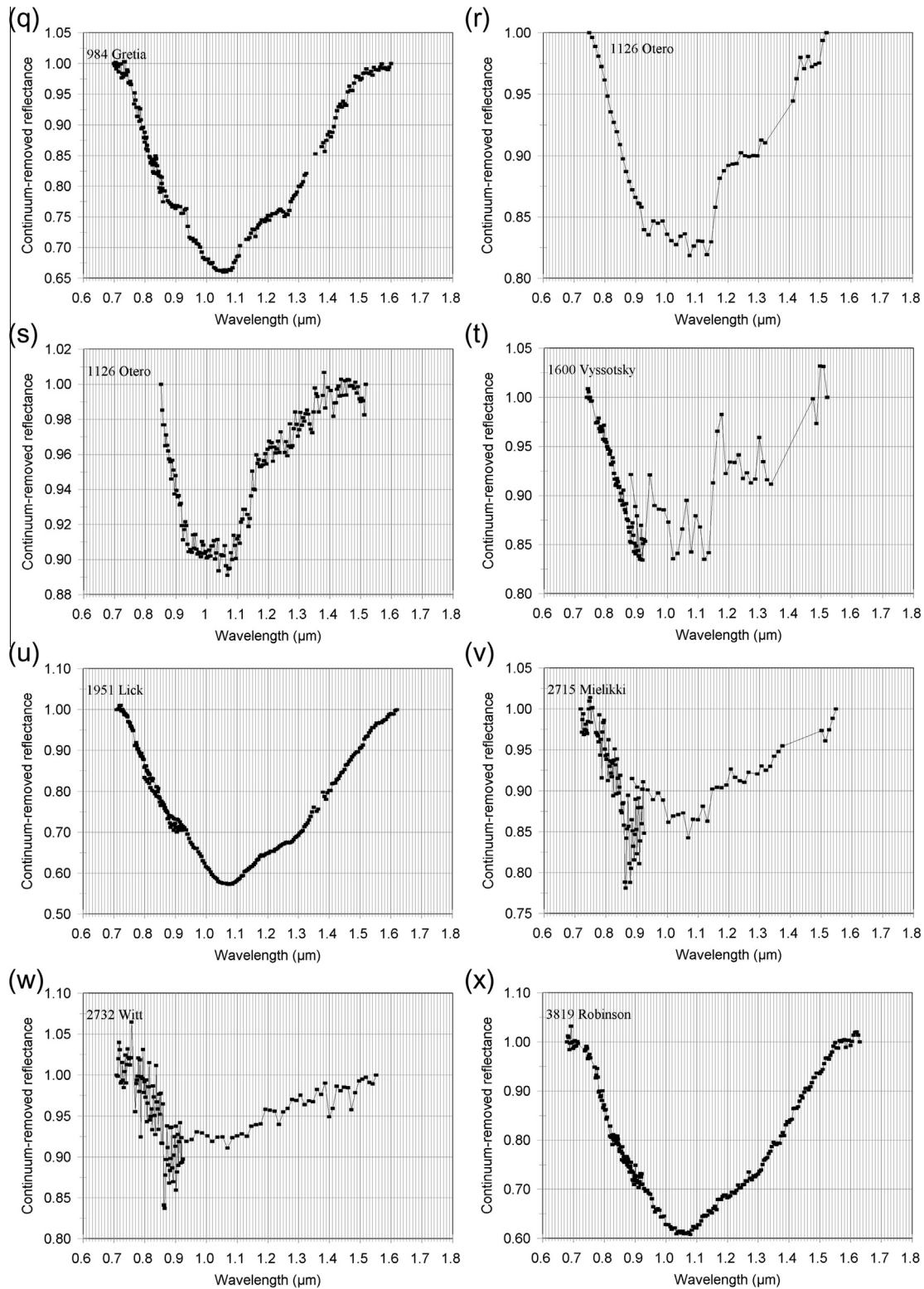


Fig. 15 (continued)

their published spectrum shows a broad flat absorption band to $\sim 1.1 \mu\text{m}$ followed by increasing reflectance to $\sim 1.6 \mu\text{m}$, and a flat, featureless spectrum beyond this. Their closest determined spectral match to a meteorite was a CV3 chondrite (an olivine-rich carbonaceous chondrite).

Hardersen et al. (2011) acquired 0.8–2.5 μm reflectance spectra of Ruth (Fig. 14p). They found that it has a band center of 1.056 μm , a depth of ~ 4 –5% and olivine composition of Fa_{-16} (Table 5). It shows a blue slope from 0.8 to $\sim 1.4 \mu\text{m}$, and flat or slightly red beyond this value. The presence of an inflection near 1.25 μm is

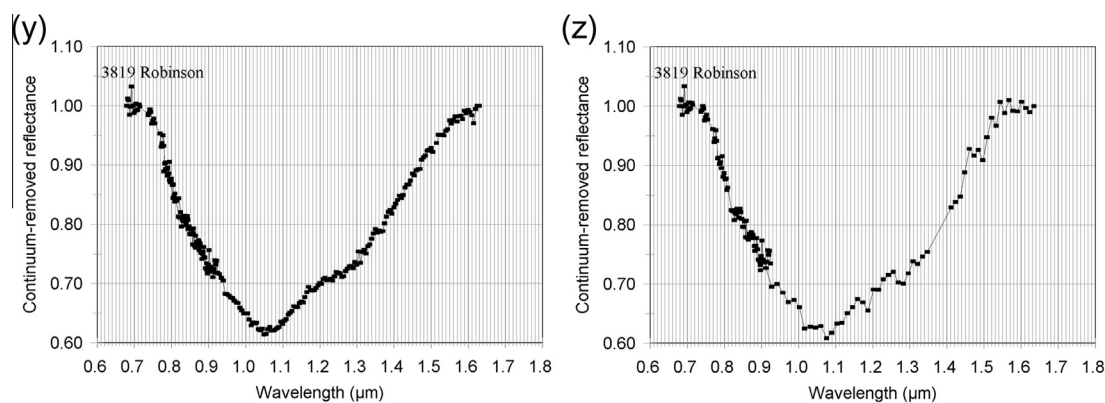


Fig. 15 (continued)

also consistent with an olivine-dominated spectrum. The spectrum of 798 Ruth is unlike most of the other asteroid spectra we examined in terms of its overall blue slope.

The spectra of Ruth suggest a low Fa olivine. Its position in the various spectral metrics space suggests a higher macroscopic iron content than Moguntia (above); the most consistent estimate is 60 ± 15 wt.%. There is no evidence of spectral reddening by npFe. In comparison to Moguntia, Ruth's olivine may be coarser grained, as this would be more consistent with its overall blue spectral slope. The most plausible meteorite analogue is the pallasites or CB chondrites (or a CV3 chondrite: Mothé-Diniz et al., 2008).

6.3.10. 863 Benkoela (A)

Benkoela's geometric albedo is variously given as 0.60 (JPL), ~ 0.11 (Masiero et al., 2011a, 2011b), or 0.44 ± 0.027 (Usui et al., 2011). We use the value of Usui et al. (2011) in our subsequent analysis. It was included in the SMASSII survey (0.435–0.925 μm) of Bus and Binzel (2002) and the MINUS survey and assigned to the A class (Table 4). Lucey et al. (1998) analyzed a spectrum of Benkoela and derived an olivine composition of Fa_{0-10} . SMASS + MINUS and SMASS + 52 color spectra of Benkoela are shown in Fig. 14q and r. The spectra are dominated by olivine, red-sloped, and with a weak pyroxene band near 1.9 μm . No visible region absorption bands are apparent (Fig. 16g).

The high albedo of Benkoela, and lack of well-resolved visible region absorption bands are strongly suggestive of fine-grained low-Fa olivine, consistent with the interpretation of Sunshine et al. (2007), and this is supported by band center determinations, which are however wide-ranging between different investigators (Fig. 15o and p). However, its high band depth is more suggestive of a coarser-grained assemblage. The spectral metrics are not fully consistent with a fine or coarse-grained assemblage, suggesting that it may be composed of coarser olivine plus a brighter, spectrally-neutral component, such as plagioclase feldspar.

If the albedo reported by Masiero et al. (2011a, 2011b) is correct, then a wider range of meteorite analogues are possible. Sanchez et al. (2014) determined that Benkoela has $\sim 32\%$ pyroxene. This abundance is in the region where band I center changes rapidly (Cloutis et al., 1986). If this abundance of pyroxene is present, it changes the possible meteorite analogues and introduces greater uncertainties in our interpretation. Low or no metal (<10 wt.%) is indicated by band depth–reflectance relationships. Some reddening npFe is suggested by spectral slope and peak position. The most plausible meteorite analogue is an olivine diogenite based on the requirement for low-Fa olivine, low metal content, and a modest pyroxene component. However, we reiterate that its spectral metrics do not allow for a robust assignment or interpretation.

6.3.11. 984 Gretia (A)

Gretia has a geometric albedo of 0.360 ± 0.012 (Usui et al., 2011). It was included in the SMASSII survey (0.435–0.925 μm) of Bus and Binzel (2002). The combined SMASS + MINUS spectrum (Fig. 14s) shows a strong 1 μm region olivine-like absorption feature and a probable pyroxene band near 2.0 μm . The data are noisier than many of the other asteroid spectra, but a broad absorption band may be present near 0.63 μm , consistent with olivine, and there may also be a narrow band near 0.45 μm ; a band near 0.495 μm cannot be confidently identified given noise in the spectrum (Fig. 16h). Band center, high albedo and band depth (Fig. 15q) are most consistent with low Fa, fine-grained olivine, and low macroscopic metal content (<10 wt.%). A magnesian olivine is consistent with the results of Sunshine et al. (2007). Some spectral reddening is suggested by spectral slope. The most plausible meteorite analogue is an olivine diogenite (assuming a spectrally significant amount of pyroxene is present: ~ 10 – 15 wt.%), or the LEW/MIL/NWA olivine-rich meteorites (Table 1).

6.3.12. 1126 Otero (A)

Otero has a geometric albedo of 0.1786 ± 0.033 (JPL). It was included in the SMASSII survey (0.435–0.925 μm) of Bus and Binzel (2002), the SMASSIR survey (0.9–1.65 μm) of Burbine and Binzel (2002) and the MINUS survey and assigned to the A class (Table 4). Its spectrum shows a broad absorption feature that is nearly flat across the 0.9–1.1 μm interval (Fig. 14t). This is consistent with either an olivine + low-calcium pyroxene assemblage, a spectral type A high-calcium pyroxene (Adams, 1974), or some combination of these mafic silicates. The presence of olivine is best indicated by the prominent inflection near 1.25 μm (Fig. 15r). The band center is located between 1.03 and 1.08 μm , depending on choice of continuum. The spectrum is strongly suggestive of olivine, likely modified by the presence of a few tens of wt.% spectral type A high-calcium pyroxene, perhaps similar to some angrites and asteroid Boznemcova (Cloutis et al., 2006b). There is a suggestion of a broad, weak 0.6–0.7 μm absorption feature, consistent with olivine; narrow shorter wavelength bands, if present, cannot be identified, likely due to the lower spectral resolution of the data (Fig. 16i).

The extended wavelength spectrum (SMASS + MINUS) shows the presence of a broad pyroxene-like absorption band centered near 2.0 μm (Fig. 14u). The broadness of this feature and possible inflections suggests the presence of at least two types of pyroxenes. The continuum-removed 1 μm region (Fig. 15s) is suggestive of the presence of olivine (band minimum near 1.05 μm , inflection near 1.25 μm), low-calcium pyroxene (inflections near 0.92 and 1.9 μm), high-calcium spectral type B pyroxene (band minimum near 2.0 μm), and high-calcium spectral type A pyroxene (inflec-

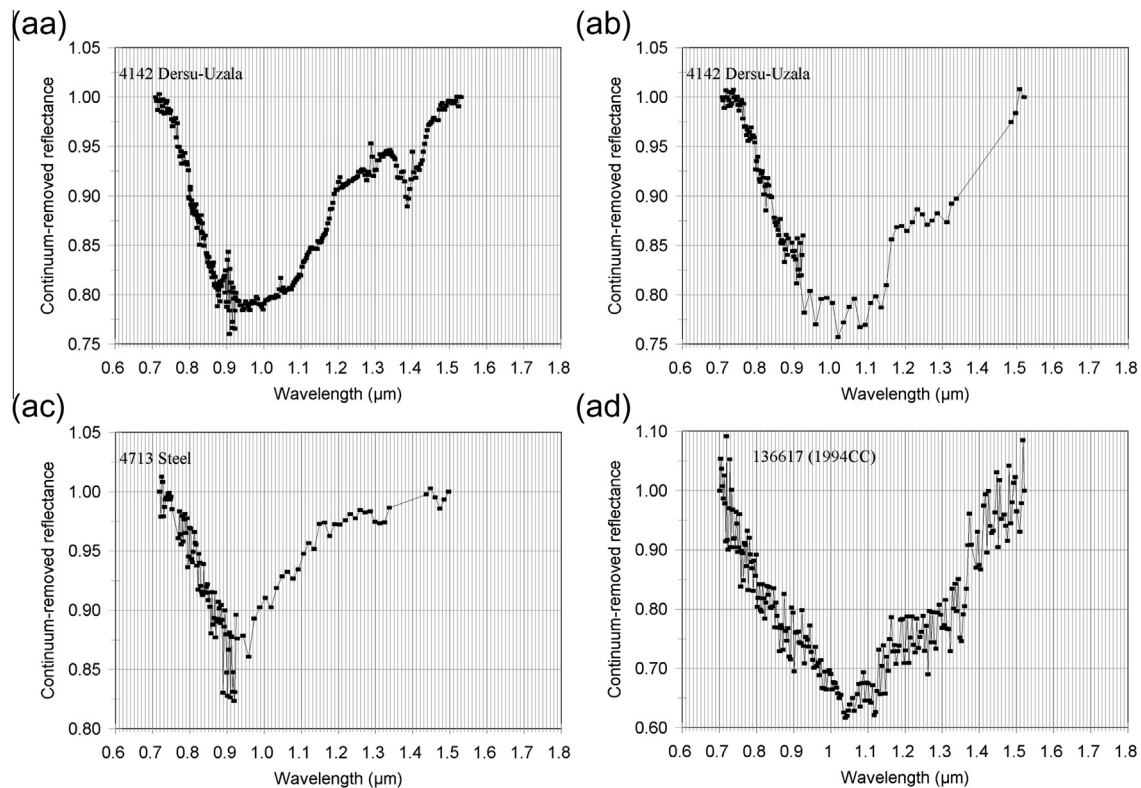


Fig. 15 (continued)

tions near 0.9 and 1.13 μm). The band area ratio (0.4) is consistent with an olivine + pyroxene assemblage. This asteroid was included in a study of the Baptistina asteroid family by Reddy et al. (2011b) who determined an olivine:pyroxene ratio of 68:32, and an olivine composition of Fa₂₇.

The spectral metrics for Otero are broadly consistent with an assemblage of 20 ± 10 wt.% macroscopic metal, and little or no spectral reddening. This interpretation is useful for demonstrating the fact that many spectral metrics are unable to capture “subtle” spectral differences that may indicate an assemblage outside the range for which they were intended. The 1 μm region absorption feature of Otero has a broader base than fine-grained olivines, but this is not captured by parameters such as FWHM. Thus, our interpretation of Otero is very tentative. There is no good plausible meteorite analogue for Otero, given the uncertainties in its composition, although an angrite-like composition is suggested by the characteristics of the 1 μm region absorption feature.

6.3.13. 1210 Morosovia (MU)

Morosovia has a geometric albedo of 0.127 ± 0.007 (Usui et al., 2011). Reflectance spectra of Morosovia acquired by Hardersen et al. (2011) showed a band center of 1.047 μm , and a depth of ~8–9% (Fig. 14v and w). This spectrum is unlike most of the other asteroid spectra we examined in terms of its overall blue slope. This asteroid may have a minor pyroxene component which moves the 1 μm band to the lower edge of the olivine field (1.047 μm). The data are too noisy to confidently identify a pyroxene absorption band in the 2 μm region. The expected 1.25 μm olivine-associated inflection is not evident. The spectral parameters for Morosovia tentatively suggest a low Fa olivine with 40 ± 10 wt.% metal (or less if the assemblage is coarse-grained) and an additional component to impart a blue slope. Pallasites are a plausible meteorite analogue.

6.3.14. 1600 Vyssotsky (A)

The geometric albedo of Vyssotsky is 0.547 ± 0.076 (Usui et al., 2011). It was included in the SMASSII survey (0.435–0.925 μm) of Bus and Binzel (2002) and the SMASSIR survey (0.9–1.65 μm) of Burbine and Binzel (2002) and assigned to the A class (Table 4). Its spectrum is somewhat noisy, but is broadly consistent with olivine in terms of overall band minimum position, possible inflection near 1.25 μm (Fig. 15t) and peak near 0.73 μm (Fig. 14x). There do not appear to be any well-defined visible region olivine absorption bands, although the data are somewhat noisy (Fig. 16j). The lack of longer wavelength data (>1.6 μm) for Vyssotsky loosens constraints on its composition. The available data suggest a low Fa olivine, some spectral reddening, and 15 ± 10 wt.% macroscopic metal (or less for a coarser assemblage). A metal-poor pallasite is the best analogues assuming little or no pyroxene is present. Its high albedo is consistent with little or no metal, a low-Fa olivine and a fine-grained assemblage.

6.3.15. 1951 Lick (A)

Lick has a geometric albedo of 0.0895 ± 0.020 (JPL). It was included in the SMASSII survey (0.435–0.925 μm) of Bus and Binzel (2002) and MINUS survey and classified as an A-type asteroid (Table 4). de León et al. (2004) acquired a 0.32–2.4 μm spectrum of Lick and found a steep red slope in the visible region, a broad olivine absorption band with a minimum at 1.032 μm and a center at 1.087 μm (± 0.022 μm), and no appreciable 2 μm absorption, which they interpret as indicating a very olivine-rich object. Its continuum-removed spectrum is similar to Brachina, a nearly-pure olivine meteorite. However, Lick has a redder overall slope than Brachina beyond 1.5 μm .

The SMASS + MINUS spectrum of Lick (Fig. 14y) is dominated by olivine and red-sloped, with no evidence of a pyroxene absorption band in the 2 μm region, but a red-sloped 1.8–2.4 μm inter-

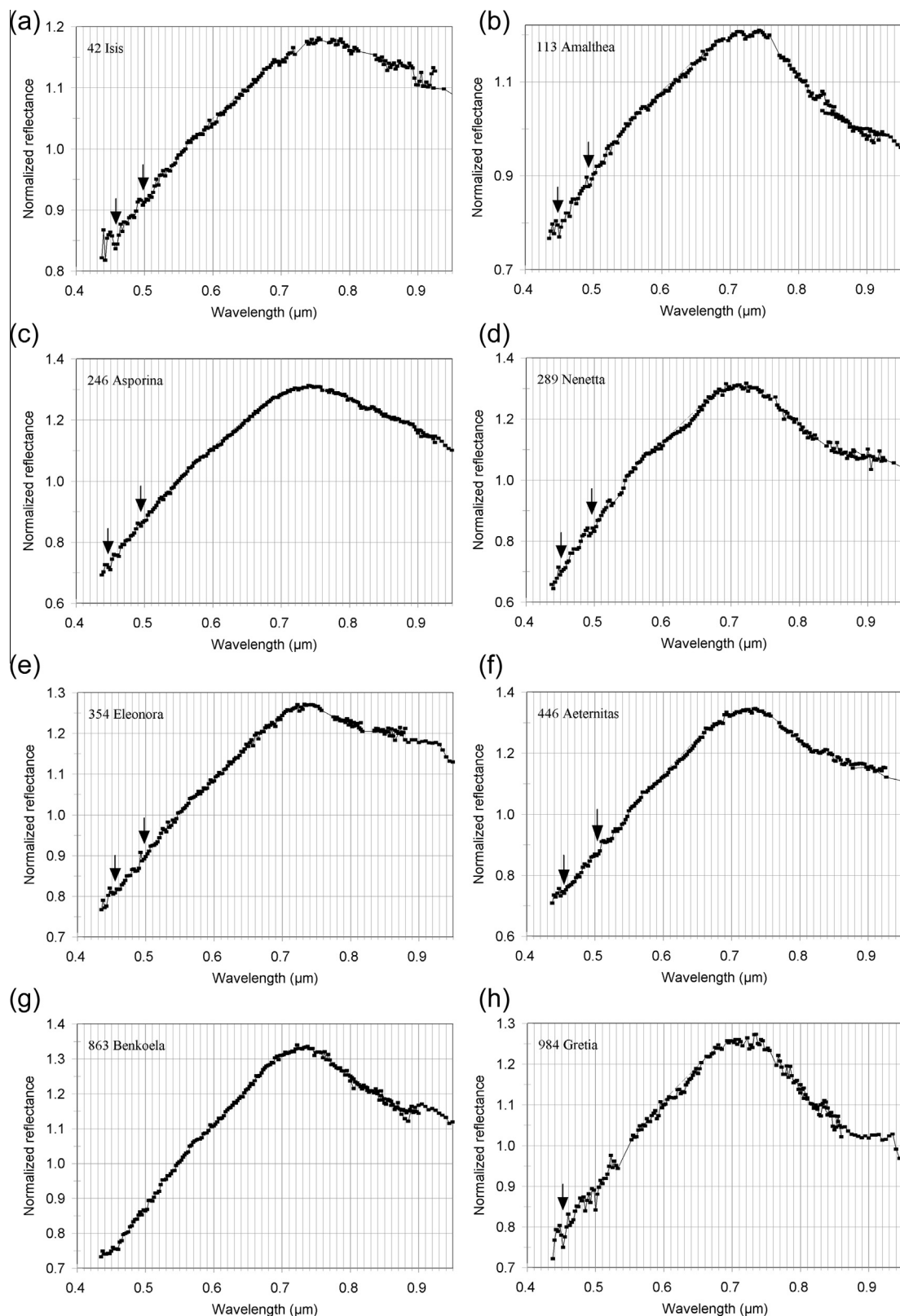


Fig. 16. Visible region spectra of some of the asteroid spectra shown in Fig. 7, showing details (if any) of minor visible region absorption bands. Putative absorption bands mentioned in the text for some of the asteroids are indicated by arrows. A possible broader absorption feature in the 0.63 μm region is highlighted by the addition of a straight line continuum across any putative feature. (a) 42 Isis. (b) 113 Amalthea. (c) 246 Asporina. (d) 289 Nenetta. (e) 354 Eleonora. (f) 446 Aeternitas. (g) 863 Benkoela. (h) 984 Gretia. (i) 1126 Otero. (j) 1600 Vyssotsky. (k) 1951 Lick. (l) 2501 Lohja. (m) 2715 Mielikki. (n) 2732 Witt. (o) 3819 Robinson. (p) 4142 Dersu-Uzala. (q) 4713 Steel.

val. No visible region absorption bands are readily apparent, with the possible exception of a band near 0.50 μm (Fig. 16k). The band center of Lick that we found (1.065 μm) is suggestive of a low to

medium (or medium to high Fa olivine if the band center value of de León et al. (2004) is correct) (Fig. 15u). Sanchez et al. (2014) determined an olivine composition of Fa₃₀, while

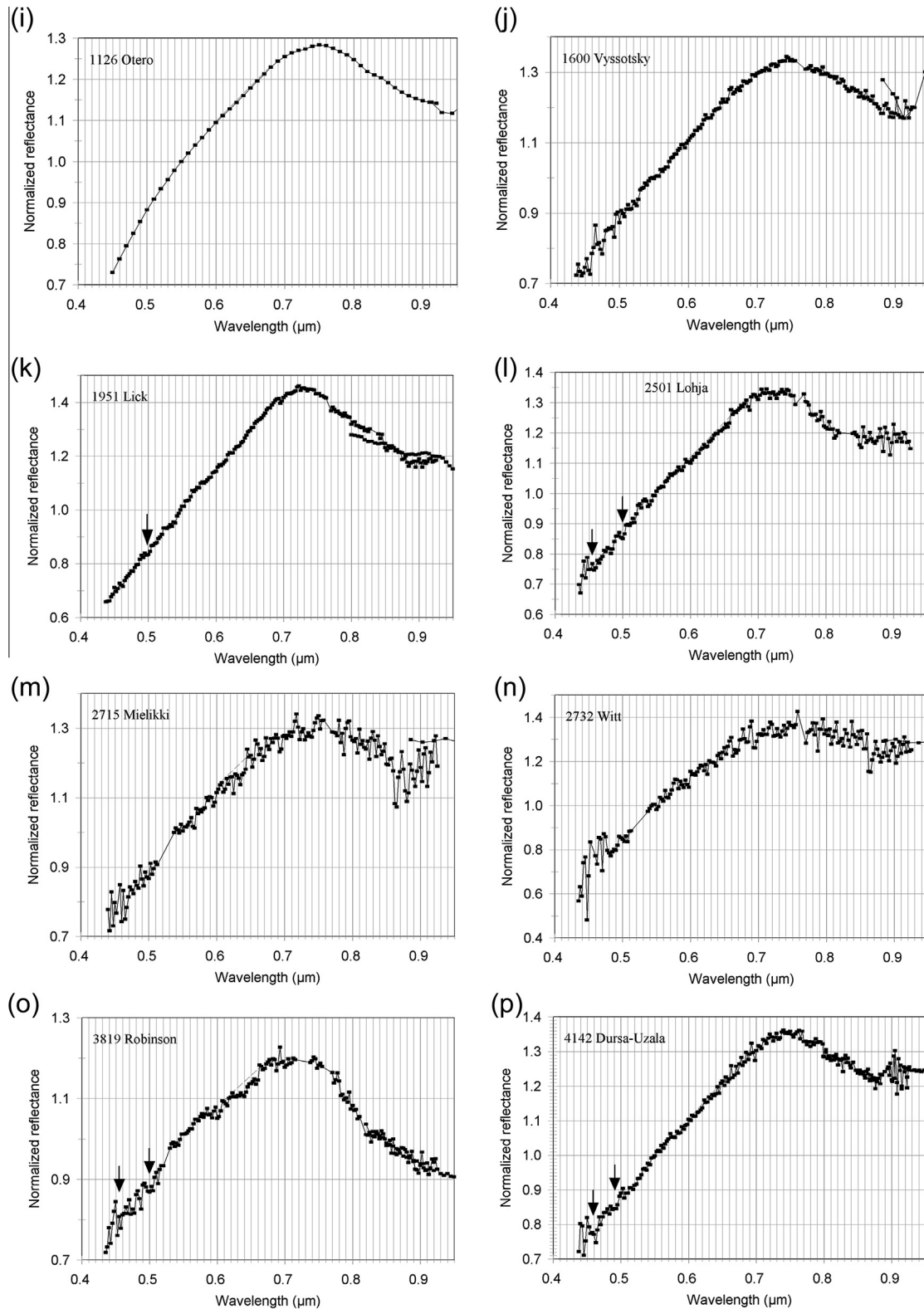


Fig. 16 (continued)

Sunshine et al. (2007) determined an olivine composition of $\sim\text{Fa}_{20}$, low macroscopic metal content (<10 wt.%), some coarser size fraction, and extensive reddening npFe. Our interpretation suggests a low-Fa, olivine-dominated object (<10% metal) with extensive npFe and perhaps an additional darkening, spectrally

neutral phase (possibly darkening but not reddening npFe). Brunetto et al. (2007) also invoked the presence of reddening npFe due to extensive space weathering to match the spectral properties of Lick, however, they did not consider macroscopic iron as a possible additional contributor to the red slope. Plausible mete-

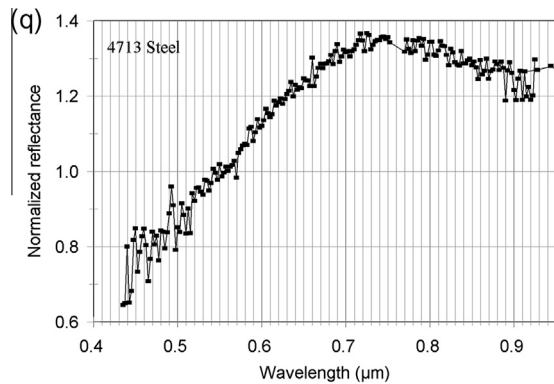


Fig. 16 (continued)

orite analogues include various fayalitic olivine-dominated, low macroscopic metal content meteorites (brachinites, R chondrites and the LEW/MIL/NWA meteorites in Table 1).

Lick has the reddest spectrum (1.8/0.56 μm ratio) of all the asteroids examined. This reddening extends beyond 1.8 μm , suggesting that it is more extensively space-weathered than the other asteroids in this study. The strong reddening coupled with a deep 1 μm band suggests reddening npFe rather than macroscopic metal is spectrally dominant.

6.3.16. 2501 Lohja (A)

The geometric albedo of Lohja is 0.275 ± 0.020 (Usui et al., 2011). It was included in the SMASSII survey (0.435–0.925 μm) of Bus and Binzel (2002). Its visible region spectrum shows a strong red slope below $\sim 0.7 \mu\text{m}$, a peak near 0.72 μm and a band minimum that is likely longer than 0.9 μm (Fig. 14z). Absorption bands may be present near 0.45, 0.50 and in the 0.63 μm region (Fig. 16l). This suggests that it may possess some coarser-grained fraction on its surface; the visible region peak position suggests $< \sim 50$ wt.% macroscopic metal. The spectrum of Lohja presented in Sunshine et al. (2007) shows a weak 2 μm absorption band, a 1 μm band minimum of 1.044 μm , a 1 μm band center of 1.061 μm (consistent with magnesium olivine), a 1 μm band depth of 42%, and a red-sloped spectrum. The spectral data are consistent with a low Fa olivine, little or no metal (< 10 wt.%), and the presence of reddening npFe. Possible meteorite analogues include R chondrites and olivine diogenites.

6.3.17. 2715 Mielikki (A)

It has a geometric albedo of 0.136 ± 0.017 (Usui et al., 2011). It was included in the SMASSII survey (0.435–0.925 μm) of Bus and Binzel (2002) and the SMASSIR survey (0.9–1.65 μm) of Burbine and Binzel (2002) and assigned to the A class (Table 4). It has an olivine-like spectrum with a band center near 1.06 μm and a prominent long wavelength shoulder near 1.25 μm (Figs. 14aa and 15v). The visible region spectrum is somewhat noisy but a broad 0.63 μm region absorption band may be present (Fig. 16m). The lack of spectral data beyond 1.6 μm hampers interpretation. Its spectrum is most consistent with a low Fa olivine, reddening npFe, 20 ± 10 wt.% macroscopic metal, and presence of a coarser-grained fraction. The best meteorite analogue is the pallasites, assuming little or no pyroxene is present.

6.3.18. 2732 Witt (A)

The geometric albedo of this asteroid is 0.30 ± 0.03 (Masiero et al., 2011a, 2011b). It was included in the SMASSII survey (0.435–0.925 μm) of Bus and Binzel (2002) and the SMASSIR survey (0.9–1.65 μm) of Burbine and Binzel (2002) and assigned to the A class (Table 4). Its spectrum (Fig. 14ab) is not fully consistent with olivine as its band center is near 1.03 μm (Fig. 15w), although

position is somewhat uncertain due to noisy data. None of the expected visible region olivine absorption bands are readily apparent (Fig. 16n), although the data are again somewhat noisy. The available data suggest that this asteroid may be an olivine + pyroxene \pm metal assemblage. The presence of pyroxene is inferred from discrepant results derived from the various spectral metrics. If olivine is assumed to be the only or major silicate, and the assemblage is fine-grained, it appears to contain $\sim 20 \pm 15$ wt.% macroscopic metal, and some reddening npFe, consistent with pallasites. The presence of a 2 μm region absorption feature, if present, would allow other meteorite analogues such as lodranites.

6.3.19. 3819 Robinson (A)

The geometric albedo of 3819 Robinson is 0.36 ± 0.298 (Masiero et al., 2011a, 2011b). It was included in the SMASSII survey (0.435–0.925 μm) of Bus and Binzel (2002) and the SMASSIR survey (0.9–1.65 μm) of Burbine and Binzel (2002) and assigned to the Sr class (Table 4). The available spectra are all consistent with an olivine-dominated assemblage (band center near 1.06 μm , a prominent inflection near 1.25 μm (Figs. 14ac–ae and 15x–z), and a broad band in the 0.6–0.7 μm region). Minor pyroxene is indicated by the broad, weak absorption band near 2.0 μm (Fig. 14ac–ad). Visible region spectra are somewhat noisy but it appears that olivine-associated absorption bands may be present near 0.455 and 0.500 μm and in the 0.63 μm region (Fig. 16o). Its band center is consistent with low Fa olivine, and with the results of Sunshine et al. (2007). Low metal content ($< \sim 10$ wt.%) is suggested by its band depth, although a somewhat higher metal content could be accommodated by a coarser assemblage. Some npFe-type reddening is suggested by its spectral slope. R chondrites, brachinites and the LEW/MIL/NWA olivine-rich meteorites in Table 1 are plausible meteorite analogues.

6.3.20. 4142 Dersu-Uzala (A)

The geometric albedo of Dersu-Uzala is 0.164 ± 0.011 (Usui et al., 2011). It was included in the SMASSII survey (0.435–0.925 μm) of Bus and Binzel (2002) and the SMASSIR survey (0.9–1.65 μm) of Burbine and Binzel (2002) and assigned to the A class (Table 4), grouped with A asteroids that have a “weaker” 1 μm band (22% deep; band center at 1.05 μm). Binzel et al. (2004) acquired visible and near-infrared spectra of this asteroid (Fig. 14af). They found a band position of $\sim 0.97 \mu\text{m}$, and an absorption band in the 2 μm region, indicative of pyroxene. The band position supports the presence of an olivine + pyroxene assemblage, or a two-pyroxene (low- and high-Ca) assemblage.

Band position is uncertain in the available spectra (Fig. 14af and ag), with estimates ranging from ~ 0.98 to $\sim 1.05 \mu\text{m}$ (Fig. 15aa and ab). This is consistent with an olivine + low-calcium pyroxene assemblage, with pyroxene abundance on the order of 10–20 wt.% (Cloutis et al., 1986). There are possible olivine bands near 0.46 and 0.49 μm (although they are shifted from the expected positions), but a 0.63 μm band is not evident (Fig. 16p). The presence of spectrally significant amounts of pyroxene complicates assemblage determinations using olivine + metal metrics. Assuming a fine-grained, low Fa olivine + metal assemblage, macroscopic metal is constrained to 20 ± 15 wt.%, and there is npFe-type spectral reddening. Plausible meteorite analogues include olivine + pyroxene-bearing, low metal content meteorites such as R chondrites.

6.3.21. 4713 Steel (A)

The geometric albedo of this object is 0.424 ± 0.082 (Usui et al., 2011). It was included in the SMASSII survey (0.435–0.925 μm) of Bus and Binzel (2002) and the SMASSIR survey (0.9–1.65 μm) of Burbine and Binzel (2002) and assigned to the A class (Table 4). Its spectrum (Fig. 14ah) is not consistent with olivine. Band center

is located between 0.92 and 0.98 μm (Fig. 15ac), indicating low-calcium pyroxene or a possible olivine + pyroxene assemblage. The data are too noisy to confidently identify visible region olivine absorption bands (Fig. 16q). Pyroxene is also suggested by a possible absorption feature in the 0.50–0.52 and 0.56 μm regions. No meteorite analogues have been assigned because of the limited spectral data.

6.3.22. 136617 (1994CC) (Sq)

Asteroid 136617 (1994CC) is a triplet system that was observed as part of the ASTEX NEA lander mission concept study by Reddy et al. (2011b). It has an estimated optical albedo of $\sim 0.42 \pm 0.10$ (Brozović et al., 2011). Its longer wavelength reflectance spectrum (Fig. 14ai) is somewhat noisy, but broadly consistent with an olivine-rich assemblage. The continuum-removed spectrum (Fig. 15aa) has a band center in the position expected for low-Fa olivine, as well as the expected olivine inflection in the 1.25 μm region. The FWHM and band depth of the 1 μm region feature suggest a low metal content (10 ± 10 wt.%). It was interpreted as being olivine-bearing and pyroxene-free with a low Fa olivine ($\sim\text{Fa}_{10}$) by Reddy et al. (2011b), consistent with the current interpretation. Its visible region spectrum does not exhibit any clearly resolvable olivine-associated absorption bands in the 0.4–0.5 μm region, although the data are somewhat noisy. The visible region data of Brozović et al. (2011) suggest an absorption band near 0.85 μm which is inconsistent with olivine. It can be plausibly linked to the brachinites and LEW/MIL/NWA achondrites.

6.4. Summary of asteroid spectra

Spectral metrics (Fig. 10) derived from available asteroid spectral data are shown in Fig. 13 and were discussed above for each individual asteroid. Here we make some general observations. It can be seen that the asteroid spectral metrics are wide ranging, implying that these olivine-rich asteroids are compositionally diverse.

Reflectance at 1.8 μm is less affected by the presence of reddening nanophase iron than shorter wavelengths. The bulk of the asteroid points fall within the 1.8 μm reflectance versus band depth field occupied by the fine-grained (<45 μm) olivine + macroscopic metal mixtures (Fig. 13a) suggesting that the bulk of these asteroids have fine-grained (<45 μm) or slightly coarser surface assemblages. The few that fall above this field likely possess a coarser grained component. Reducing uncertainties in geometric albedo would reduce the horizontal spread for many of these asteroids.

FWHM is reduced by the addition of macroscopic metal, but largely unaffected by reddening npFe. It also increases with increasing grain size. Most of the asteroid spectra plot inside the fine-grained olivine + metal field, consistent with assemblages optically dominated by a fine-grained (<45 μm) olivine component (Fig. 13b). They also generally plot outside the field occupied by pallasite slab spectra. The spectral metric best suited to recognizing intact (solid) olivine + metal assemblages is arguably FWHM. As shown in Fig. 13b, while some individual asteroid spectra have FWHM close to or just within the pallasite slab field (e.g., 289 Nenetta, 863 Benkoela), their collective spectral parameters fail to consistently overlap with the pallasite slab field. Also, as mentioned, if these asteroids possess a coarser-grained component, this would shift the data points up and out of the fine-grained field.

Reflectance at 0.56 μm is largely a function of grain size and metal content, as well as npFe. Spectral reddening due to npFe will reduce 0.56 μm reflectance and leave band depth largely unaffected. We see that many of the asteroids plot outside the field occupied by low and moderate Fa content olivines (Fig. 13c). The direction of movement is consistent with how reddening npFe is

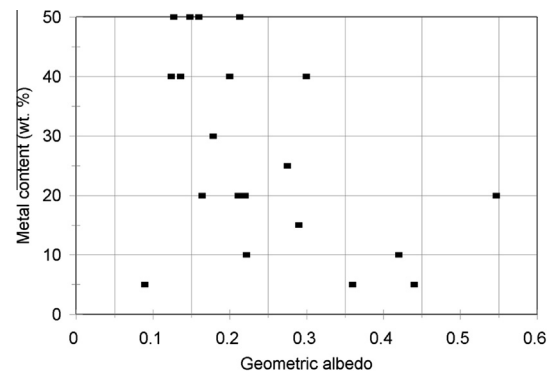


Fig. 17. Relationship between geometric albedo and derived metal content for the asteroids included in this study. Asteroid 1951 Lick is the point in the lower left corner. Error bars have been omitted for clarity.

expected to shift this parameter. While a few asteroids (9 Metis, 1600 Vyssotsky, 2732 Witt, and 4713 Steel) appear to be largely unaffected by npFe based on this metric, it should be noted that this metric alone is not sufficient to determine the presence of reddening npFe.

A number of studies, described above, have found that the presence of nanophase iron introduces a red slope (with the reddening increasing toward shorter wavelengths), and also reduces overall reflectance, but does not appreciably affect band depth except at high npFe abundances (Kohout et al., 2014). Our mixture spectra indicate that the introduction of larger metal grains reduces overall reflectance, induces a modestly red slope across all wavelengths, and reduces band depths. This difference potentially allow for discrimination of nanophase from macroscopic iron. The 1.8/0.56 μm metric is a measure of red slope. It can be seen that many of the asteroids are more red-sloped than our fine-grained mineral mixtures, with many plotting well outside the field occupied by the fine-grained mixtures, suggestive of reddening npFe. A number also appear to have deeper absorption bands than the pure fine-grained olivine (Fig. 13d), suggesting contributions from a coarser-grained component. This is confirmed by the apparent presence of visible region olivine-associated absorption bands in the 0.4–0.5 μm and 0.6 μm regions in many of the asteroid spectra and which become apparent in larger (<45 but not $\ll 45$ μm) size assemblages. Using the 1.8/0.56 μm metric, the asteroid spectra that appear to be unaffected by npFe on the basis of 0.56 μm reflectance alone do, in fact, show red-sloped spectra, indicative of reddening npFe.

When visible region peak position is used as a metric (Fig. 13e), the asteroid points are generally shifted in a direction consistent with the presence of a reddening agent, or if macroscopic metal is present, with the presence of a larger grain size fraction. The most metal-rich asteroids (e.g., 9 Metis, 766 Moguntia, and 798 Ruth) also have the longest wavelength 0.7 μm region peak positions, further confirming their metal-rich nature.

Table 6 shows a summary of the compositions determined for the asteroids discussed above, as well as data on some of their orbital and physical properties. We performed paired comparisons of various asteroidal properties for these objects: semi-major axis, eccentricity, orbital inclination, diameter, rotation period, geometric albedo, metal content, and olivine Fa content. The only plausible correlation that was found was a negative correlation between inferred macroscopic metal content and geometric albedo (Fig. 17); however its statistical significance was low ($R^2 = 0.27$). The asteroid that fall furthest off the trend was 1951 Lick, which has the reddest-sloped spectrum. The found trend was not unexpected, as increasing metal content should reduce albedo, but nev-

ertheless provides evidence that the albedo-reducing effects of metal seem to be operating on asteroids.

We also made some tentative meteoritic assignments for the various asteroids (Table 7). These assignments were based on the derived asteroid mineralogies and the mineralogies and available spectroscopic data for the olivine-bearing meteorites described in Table 1. We found that pallasites were the most abundant plausible meteorite analogues, although a number of other meteorite groups could also be plausibly assigned to some asteroids. Most of the asteroids could be reasonably assigned to at least one of the olivine-bearing meteorites included in the analysis. Perhaps not surprisingly, the asteroids included in our analysis span a range of olivine compositions and olivine/metal ratios, as we have included asteroids from different taxonomic classes. The largest uncertainties exist for those asteroids with limited spectral coverage.

A notable result of our analysis is that modest space weathering seems to have affected most of the asteroid spectra. This evidence is based largely on the wavelength position of the 0.7 μm peak, the 1.8/0.56 μm reflectance ratio, and the 2.4/1.8 μm versus 1.8/0.56 μm reflectance ratios. The form of space weathering that is inferred is reddening of spectral slopes with increasing reddening toward shorter wavelengths, a process that has been simulated in the laboratory (e.g., Hiroi and Sasaki, 2001; Sasaki et al., 2001, 2002, 2003) and has been shown to operate on asteroid Itokawa (Binzel et al., 2001; Noguchi et al., 2011).

7. Summary and conclusions

Olivine + metal assemblages are expected to be represented by a number of asteroids based on the occurrence of multiple meteorite classes that are dominated by these two materials (Table 1). Reflectance spectra of these types of assemblages vary in largely expected ways. Increasing metal content correlates with decreases in reflectance, olivine absorption band depth, width and minimum, and with increases in overall spectral slope and position of the 0.7 μm region local reflectance peak. Band centers can be recovered to within $\sim\pm 3$ nm for all but the most metal-rich assemblages. Spectral reddening caused by npFe most strongly affects lower wavelength regions (reducing reflectance) and long/short wavelength reflectance ratios, while absorption band depths and centers are largely unaffected.

To determine olivine/metal abundances and olivine composition, band depth versus spectral parameters such as absolute reflectance (at 0.56 and 1.8 μm), reflectance ratios (1.8/0.56 μm), band positions (minima and centers), and band widths are all useful. For robust analysis, multiple spectral metrics should be applied. The most reliable approach involves first determining 1 μm region band center, and assigning the spectrum to a low, medium, or high Fa content group. Band minimum in this region can also be used as a check of whether the assemblage may be very metal-rich. Band center position and the presence of absorption features in the 2 μm region can be used to determine whether spectrally significant amounts of pyroxene and/or chromite are present, which will affect olivine \pm metal assemblage characterization. The possibility of a coarser-grained assemblage can best be assessed by whether spectral metrics fall outside the fields defined for fine-grained assemblages, as well as whether minor visible region absorption bands are present.

Band depth in the 1 μm region is used as a common metric, and when plotted against reflectance at 1.8 μm and FWHM, can be used to constrain metal abundance, as these two metrics are least affected by npFe-type spectral reddening. Application of spectral metrics involving reflectance at 0.56 μm and 1.8/0.56 μm reflectance ratio provides further checks on olivine/metal ratios as well as providing indications of spectral reddening due to npFe. Most

spectral metrics change more slowly for high metal abundance assemblages, but the wavelength position of the 0.7 μm region reflectance peak shows large changes at high metal abundances. Olivine + metal slabs (represented by pallasites) can be recognized by the fact that some of their spectral parameters plot outside the field occupied by fine-grained powders.

The olivine-rich asteroids that we have included in our analysis range from metal-free, or nearly so, to some where metal is more abundant than olivine. It also appears that olivine composition includes both low (Fa_{1–33}) and medium (Fa_{34–68}), and possibly high, Fa varieties. We see evidence for space weathering on the majority of the asteroids, in the form of reddening, likely due to npFe. It appears that most of the olivine-rich asteroids can be linked to at least one type of meteorite; alternatively, most olivine-rich meteorites can be linked to at least one plausible asteroidal parent body.

Acknowledgments

We gratefully acknowledge the support provided by the Canadian Space Agency (CSA), the Natural Sciences and Engineering Research Council of Canada, and the University of Winnipeg (UW) for this study. We also wish to thank the Canada Foundation for Innovation, the Manitoba Research Innovations Fund, CSA, and UW for supporting the establishment of the Planetary Spectrophotometer Facility. We further wish to acknowledge the support provided by the NASA-funded multi-user RELAB Facility at Brown University. We thank Neva Fowler-Gerace, Brendt Hyde, and Ian Nicklin from the Royal Ontario Museum for providing samples of the Springwater pallasite and associated data. We also wish to thank Tomáš Kohout and an anonymous reviewer for their many helpful suggestions and comments.

References

- Adams, J.B., 1974. Visible and near-infrared diffuse reflectance spectra of pyroxenes as applied to remote sensing of solid objects in the Solar System. *J. Geophys. Res.* 79, 4829–4836.
- Auten, T.A., 1973. On the brittleness of Gibeon meteoritic iron. *Meteoritics* 8, 189–196.
- Bell, J.F., Hawke, B.R., Singer, R.B., Gaffey, M.J., 1984. The olivine asteroids: Discovery, mineralogy, and relationship to meteorites. *Lunar Planet. Sci.* 15, 48–49 (abstract).
- Bell, J.F., Owensby, P.D., Hawke, B.R., Gaffey, M.J., 1988. The 52-color asteroid survey: Final results and interpretation. *Lunar Planet. Sci.* 19, 57–58 (abstract).
- Benedix, G.K., McCoy, T.J., Keil, K., 1995. Textural and mineralogical variations in winonaite: Clues to the history of the IAB iron-winonaite parent body. *Lunar Planet. Sci.* 26, 99–100.
- Benedix, G.K., McCoy, T.J., Keil, K., Love, S.G., 2000. A petrologic study of the IAB iron meteorites: Constraints on the formation of the IAB-winonaite parent body. *Meteorit. Planet. Sci.* 35, 1127–1141.
- Berlin, J., Lingemann, Stöffer, D., 2003. Visible and near-infrared reflectance spectra of Rumuruti. *Lunar Planet. Sci.* 34, Abstract #1764.
- Binzel, R.P., Rivkin, A.S., Bus, S.J., Sunshine, J.M., Burbine, T.H., 2001. MUSES-C target Asteroid (25143) 1998 SF₃₆: A reddened ordinary chondrite. *Meteorit. Planet. Sci.* 36, 1167–1172.
- Binzel, R.P., Birlan, M., Bus, S.J., 2004. Spectral observations for near-Earth objects including potential target 4660 Nereus: Results from Meudon remote observations at the NASA Infrared Telescope Facility (IRTF). *Planet. Space Sci.* 52, 291–296.
- Birlan, M., Vernazza, P., Nedelcu, D.A., 2007. Spectral properties of nine M-type asteroids. *Astron. Astrophys.* 475, 747–754.
- Bischoff, A. et al., 1994. Acfer 217 – A new member of the Rumuruti chondrite group (R). *Meteoritics* 29, 264–274.
- Boesenberg, J.S. et al., 1995. Pyroxene pallasites: A new pallasite grouplet. *Meteoritics* 30, 488–489.
- Brearely, A.J., Jones, R.H., 1998. Chondritic meteorites. In: Papike, J.J. (Ed.), *Planetary Materials. Reviews in Mineralogy*, vol. 36. Mineralogical Society of America, Washington, DC (Chapter 3).
- Britt, D.T., Pieters, C.M., 1988. Bidirectional reflectance properties of iron–nickel meteorites. *Lunar Planet. Sci.* 18, 503–512.
- Brozović, M., Benner, L.A.M., Taylor, P.A., Nolan, M.C., Howell, E.S., Magri, C., Scheeres, D.J., Giorgini, J.D., Pollock, J.T., Pravec, P., Galád, A., Fang, J., Margot, J.-L., Busch, M.W., Shepard, M.K., Reichart, D.E., Ivarsen, K.M., Haislip, J.B., LaCluyze, A.P., Jao, J., Slade, M.A., Lawrence, K.J., Hicks, M.D., 2011. Radar and

- optical observations and physical modeling of triple near-Earth Asteroid (136617) 1994 CC. *Icarus* 216, 241–256.
- Brunetto, R., Strazzulla, G., 2005. Elastic collisions in ion irradiation experiments: A mechanism for space weathering of silicates. *Icarus* 179, 265–273.
- Brunetto, R., Romano, F., Blanco, A., Fonti, S., Martino, M., Orofino, V., Verrienti, C., 2006a. Space weathering of silicates simulated by nanosecond pulse UV excimer laser. *Icarus* 180, 546–554.
- Brunetto, R., Vernazza, P., Marchi, S., Birlan, M., Fulchignoni, M., Orofino, V., Strazzulla, G., 2006b. Modeling asteroid surfaces from observations and irradiation experiments: The case of 832 Karin. *Icarus* 184, 327–337.
- Brunetto, R., de Leon, J., Licandro, J., 2007. Testing space weathering models on A-type Asteroid (1951) Lick. *Astron. Astrophys.* 472, 653–656.
- Burbine, T.H., 2002. Asteroids: Their composition and impact threat. *Bull. Czech Geol. Surv.* 77, 243–252.
- Burbine, T.H., Binzel, R.P., 2002. Small main-belt asteroid spectroscopic survey in the near-infrared. *Icarus* 159, 468–499.
- Burbine, T.H., McCoy, T.J., Hinrichs, J.L., Lucey, P.G., 2006. Spectral properties of angrites. *Meteorit. Planet. Sci.* 41, 1139–1145.
- Burbine, T.H., Greenwood, R.C., Buchanan, P.C., Franchi, I.A., Smith, C.L., 2007. Reflectance spectra of mesosiderites: Implications for Asteroid 4 Vesta. *Lunar Planet. Sci.* 38, Abstract #2119.
- Burbine, T.H., Buchanan, P.C., Dolkar, T., Binzel, R.P., 2009. Pyroxene mineralogy of near-Earth vestoids. *Meteorit. Planet. Sci.* 44, 1331–1341.
- Burns, R.G., 1970. Crystal field spectra and evidence of cation ordering in olivine minerals. *Am. Mineral.* 55, 1608–1632.
- Burns, R.G., Huggins, F.E., Abu-Eid, R.M., 1972. Polarized absorption spectra of single crystals of lunar pyroxenes and olivines. *Moon* 4, 93–102.
- Bus, S.J., Binzel, R.P., 2002. Phase II of the small main-belt asteroid spectroscopic survey. *Icarus* 158, 106–145.
- Buseck, P.R., 1977. Pallasite meteorites – Mineralogy, petrology and geochemistry. *Geochim. Cosmochim. Acta* 41, 711–740.
- Buseck, P.R., Holdsworth, E., 1977. Phosphate minerals in pallasite meteorites. *Mineral. Mag.* 41, 91–102.
- Buz, J., Ehlmann, B.L., 2014. Effects of grain size on the reflectance spectroscopy of olivine in the vis–NIR and the derivation of olivine composition using Modified Gaussian Modeling. *Lunar Planet. Sci.* 45, Abstract #2810.
- Cahill, J.T.S. et al., 2012. Determination of iron metal optical constants: Implications for ultraviolet, visible, and near-infrared remote sensing of airless bodies. *Geophys. Res. Lett.* 39, L10204.
- Carrez, P. et al., 2002. Low-energy helium ion irradiation-induced amorphization and chemical changes in olivine: Insights for silicate dust evolution in the interstellar medium. *Meteorit. Planet. Sci.* 37, 1599–1614.
- Chapman, C.R., Gaffey, M.J., 1979. Reflectance spectra for 277 asteroids. In: Gehrels, T., Matthews, M. (Eds.), *Asteroids*. Univ. of Arizona Press, Tucson, pp. 25–60.
- Chikami, J., Mikouchi, T., Takeda, H., Miyamoto, M., 1997. Mineralogy and cooling history of the calcium–aluminum–chromium enriched ureilite, Lewis Cliffs 88774. *Meteorit. Planet. Sci.* 32, 343–348.
- Clark, B.E., 1995. Spectral mixing models of S-type asteroids. *J. Geophys. Res.* 100, 14443–14456.
- Clark, R.N., Roush, T.L., 1984. Reflectance spectroscopy: Quantitative analysis techniques for remote sensing applications. *J. Geophys. Res.* 89, 6329–6340.
- Clénet, H., Pinet, P., Daydou, Y., Heuripeau, F., Rosemberg, C., Baratoux, D., Chevrel, S., 2011. A new systematic approach using the Modified Gaussian Model: Insight for the characterization of chemical composition of olivines, pyroxenes and olivine–pyroxene mixtures. *Icarus* 213, 404–422.
- Cloutis, E.A., 1997. Manganese-rich olivines: Identification from spectral reflectance properties. *J. Geophys. Res.* 102, 25575–25580.
- Cloutis, E.A., Gaffey, M.J., Jackowski, T.L., Reed, K.L., 1986. Calibration of phase abundance, composition, and particle size distribution for olivine–orthopyroxene mixtures from reflectance spectra. *J. Geophys. Res.* 91, 11641–11653.
- Cloutis, E.A., Gaffey, M.J., Smith, D.G.W., Lambert, R.St.J., 1990. Metal silicate mixtures: Spectral properties and applications to asteroid taxonomy. *J. Geophys. Res.* 95, 8323–8338.
- Cloutis, E.A., Sunshine, J.M., Morris, R.V., 2004. Spectral reflectance–compositional properties of spinels and chromites: Implications for planetary remote sensing and geothermometry. *Meteorit. Planet. Sci.* 39, 545–565.
- Cloutis, E., Craig, M., Kaletzke, L., McCormack, K., Stewart, L., 2006a. HOSERLab: A new planetary spectrophotometer facility. *Lunar Planet. Sci.* 37, Abstract #2121.
- Cloutis, E.A., Binzel, R.P., Burbine, T.H., Gaffey, M.J., McCoy, T.J., 2006b. Asteroid 3628 Boznemcova: Covered with angrite-like basalts? *Meteorit. Planet. Sci.* 41, 1147–1161.
- Cloutis, E.A., Hardersen, P.S., Bish, D.L., Bailey, D.T., Gaffey, M.J., Craig, M.A., 2010a. Reflectance spectra of iron meteorites: Implications for spectral identification of their parent planets. *Meteorit. Planet. Sci.* 45, 304–332.
- Cloutis, E.A. et al., 2010b. Spectral reflectance properties of ureilites. *Meteorit. Planet. Sci.* 45, 1668–1694.
- Cloutis, E.A., Hudon, P., Hiroi, T., Gaffey, M.J., 2012a. Spectral reflectance properties of carbonaceous chondrites: 3. CR chondrites. *Icarus* 217, 389–407.
- Cloutis, E.A., Hudon, P., Hiroi, T., Gaffey, M.J., Mann, P., Bell III, J.F., 2012b. Spectral reflectance properties of carbonaceous chondrites: 6. CV chondrites. *Icarus* 221, 328–358.
- Cloutis, E.A., Hudon, P., Hiroi, T., Gaffey, M.J., Mann, P., 2012c. Spectral reflectance properties of carbonaceous chondrites: 5. CO chondrites. *Icarus* 220, 466–486.
- Cloutis, E.A., Hudon, P., Hiroi, T., Gaffey, M.J., 2012d. Spectral reflectance properties of carbonaceous chondrites: 7. CK chondrites. *Icarus* 221, 911–924.
- Cloutis, E.A., Hudon, P., Hiroi, T., Gaffey, M.J., Mann, P., 2012e. Spectral reflectance properties of carbonaceous chondrites: 8. “Other” carbonaceous chondrites: CH, ungrouped, polymict, xenolithic inclusions, and R chondrites. *Icarus* 221, 984–1001.
- Cloutis, E.A., Izawa, M.R.M., Pompilio, L., Reddy, V., Hiesinger, H., Nathues, A., Mann, P., Le Corre, L., Palomba, E., Bell III, J.F., 2013. Spectral reflectance properties of HED meteorites + CM2 carbonaceous chondrites: Comparison to HED grain size and compositional variations and implications for the nature of low-albedo features on Asteroid 4 Vesta. *Icarus* 223, 850–877.
- Corder, C.A., Day, J.M.D., Patchen, A.P., Marti, K., Taylor, L.A., 2013. Petrology of acapulcoites and lodranites and the anomalous achondrite Lewis Cliffs 88763. *Lunar Planet. Sci.* 44, Abstract #2653.
- Corder, C.A., Day, J.M.D., Rumble III, D., Assayag, N., Cartigny, P., Taylor, L.A., 2014. Petrology and geochemistry of achondrites LEW 88763, MIL 090206 and MIL 090405: Comparisons with acapulcoites–lodranites, brachinites and chondrites. *Lunar Planet. Sci.* 45, Abstract #2752.
- Craig, M.A., Cloutis, E.A., Bailey, D.T., 2007. The effects of grain size, <45–1000 μm, on the reflectance spectrum of planetary analogs from 0.35–2.5 μm. *Lunar Planet. Sci.* 38, Abstract #1356.
- Cruikshank, D.P., Hartmann, W.K., 1984. The meteorite–asteroid connection: Two olivine-rich asteroids. *Science* 223, 281–283.
- de León, J., Duffard, R., Licandro, J., Lazzaro, D., 2004. Mineralogical characterization of A-type Asteroid (1951) Lick. *Astron. Astrophys.* 422, L59–L62.
- Dollfus, A., 1971. Physical studies of asteroids by polarization of light. In: Gehrels, T. (Ed.), *Physical Studies of Minor Planets*. NASA-SP-267.
- Dollfus, A., Geake, J.E., 1975. Polarimetric properties of the lunar surface and its interpretation. Part 7. Other Solar System objects. *Proc. Lunar Sci. Conf.* 6, 2749–2768.
- Dollfus, A., Mandeville, J.-C., Duseaux, M., 1979. The nature of the M-type asteroids from optical polarimetry. *Icarus* 37, 124–132.
- DuFresne, E.R., Roy, S.K., 1961. A new phosphate mineral from the Springwater pallasite. *Geochim. Cosmochim. Acta* 24, 198–205.
- Eckstrand, O.R. (Ed.), 1984. *Canadian Mineral Deposit Types: A Geological Synopsis*. Economic Geology Report 36. Geol. Surv. Canada, Ottawa.
- Evans, A.M., 1980. *An Introduction to Ore Geology*. Blackwell, London, UK.
- Evans, B.W., Frost, B.R., 1975. Chrome-spinel in progressive metamorphism: A preliminary analysis. *Geochim. Cosmochim. Acta* 39, 959–972.
- Floran, R.J., Prinz, M., Hlava, P.F., Keil, K., Nehru, C.E., Hinthorne, J.R., 1978. The Chassigny meteorite: A cumulate dunite with hydrous amphibole-bearing melt inclusions. *Geochim. Cosmochim. Acta* 42, 1213–1229.
- Fowler-Gerace, N.A., Tait, K.T., Moser, D.E., Hyde, B.C., Barker, I., 2013. Mineralogical investigation of the phosphorus-rich Springwater pallasite. 76 Annual Meteorit. Soc. Meet. Abstract #5276.
- Gaffey, M.J., 1976. Spectral reflectance characteristics of the meteorite classes. *J. Geophys. Res.* 81, 905–920.
- Gaffey, M.J., Bell, J.F., Brown, R.H., Burbine, T.H., Piatek, J.L., Reed, K.L., Chaky, D.A., 1993. Mineralogical variations within the S-type asteroid class. *Icarus* 106, 573–602.
- Gaffey, M.J., Reddy, V., Fieber-Beyer, S., Cloutis, E., 2014. Asteroid (354) Eleonora: Plucking an odd duck. *Lunar Planet. Sci.* 45, Abstract #1453.
- Gardner-Vandy, K.G., Lauretta, D.S., McCoy, T.J., 2013. A petrologic, thermodynamic and experimental study of brachinites: Partial melt residues of an R chondrite-like precursor. *Geochim. Cosmochim. Acta* 122, 36–57.
- Goodrich, C.A., Kita, N.T., Warren, P.H., Rubin, A.E., 2012. MIL 090340 and MIL 090206: Two more brachinite-like achondrites mis-identified as ureilites. *Met. Soc.* 75, Abstract #5272.
- Graham, A.L., Easton, A.J., Hutchison, R., 1977. Forsterite chondrites; the meteorites Kakangari, Mount Morris (Wisconsin), Pontlyfni, and Winona. *Mineral. Mag.* 41, 201–210.
- Grossman, J.N., Zipfel, J., 2001. The meteoritical bulletin, no. 85. *Meteorit. Planet. Sci.* 36, A293–A322.
- Grossman, J.N., Rubin, A.E., MacPherson, G.J., 1988. ALH85085: A unique volatile-poor carbonaceous chondrite with possible implications for nebular fractionation processes. *Earth Planet. Sci. Lett.* 91, 33–54.
- Hardersen, P.S., Cloutis, E.A., Reddy, V., Mothé-Diniz, T., Emery, J.P., 2011. The M-/X-asteroid nomenclature: Results of an NIR spectral survey of 45 main-belt asteroids. *Meteorit. Planet. Sci.* 46, 1910–1938.
- Hinrichs, J.L., Lucey, P.G., 2002. Temperature-dependent near-infrared spectral properties of minerals, meteorites, and lunar soil. *Icarus* 155, 169–180.
- Hinrichs, J.L., Lucey, P.G., Meibom, A., Krot, A.N., 1999. Temperature dependent near-infrared spectra of olivine and H5 ordinary chondrites. *Lunar Planet. Sci.* 30, Abstract #1505.
- Hiroi, T., Sasaki, S., 2001. Importance of space weathering simulation products in compositional modeling of asteroids: 349 Dembowska and 446 Aeternitas as examples. *Meteorit. Planet. Sci.* 36, 1587–1596.
- Hiroi, T., Takeda, H., 1991. Reflectance spectroscopy and mineralogy of primitive achondrites–lodranites. *Proc. NIPR Symp. Antarct. Meteorit.* 4, 163–177.
- Hiroi, T., Bell, J.F., Takeda, H., Pieters, C.M., 1992. Spectral comparison between olivine-rich asteroids and pallasites. *Symp. Antarct. Meteorit.* 17, 53–56.
- Hiroi, T., Bell, J.F., Takeda, H., Pieters, C.M., 1993. Modeling of S-type asteroid spectra using primitive achondrites and iron meteorites. *Icarus* 102, 107–116.
- Hoffmann, H., Berger, M., Neukum, G., 1991. Ni- and Fe-powders: Grain size effects and compositional influence on the spectral reflectance. *Lunar Planet. Sci.* 22, Abstract #1288.

- Hyde, B.C. et al., 2013. Northwest Africa 7680: An ungrouped achondrite with affinities to primitive achondrite groups. 76th Annual Meteorit. Soc. Meet. Abstract #5207.
- Irvine, T.N., 1975. Crystallization sequence in the Muskox intrusion and other layered intrusions: II. Origin of chromite layers and similar deposits of other magmatic ores. *Geochim. Cosmochim. Acta* 39, 991–1020.
- Johnson, T.V., Fanale, F.P., 1973. Optical properties of carbonaceous chondrites and their relationship to asteroids. *J. Geophys. Res.* 78, 8507–8518.
- Kallemeyn, G.W., Rubin, A.E., Wasson, J.T., 1996. The compositional classification of chondrites: VII. The R chondrite group. *Geochim. Cosmochim. Acta* 60, 2243–2256.
- Keil, K., 1962. On the phase composition of meteorites. *J. Geophys. Res.* 67, 4055–4061.
- Keil, K., 1968. Mineralogical and chemical relationships among enstatite chondrites. *J. Geophys. Res.* 73, 6945–6976.
- Keil, K., Fredriksson, K., 1964. The iron, magnesium, and calcium distribution in coexisting olivines and rhombic pyroxenes of chondrites. *J. Geophys. Res.* 69, 3487–3515.
- Kelley, M.S., Gaffey, M.J., 2000. 9 Metis and 113 Amalthea: A genetic asteroid pair. *Icarus* 144, 27–38.
- King, T.V.V., Ridley, W.L., 1987. Relation of spectroscopic reflectance of olivine to mineral chemistry and some remote sensing implications. *J. Geophys. Res.* 92, 11457–11469.
- Kohout, T., Čuda, J., Filip, J., Britt, D., Bradley, T., Tuček, J., Skála, R., Kletetschka, G., Kašlík, J., Malina, O., Šišková, K., Zbořil, R., 2014. Space weathering simulations through controlled growth of iron nanoparticles on olivine. *Icarus* 237, 75–83.
- Lane, M.D., Dyar, M.D., Bishop, J.L., 2007. Spectra of phosphate minerals as obtained by visible–near infrared reflectance, thermal infrared emission, and Mossbauer laboratory analyses. *Lunar Planet. Sci.* 38. Abstract #2210.
- Larouci, N., Jambon, A., Chennaoui A., Boudouma, O., Gattacceca, J., Sonzongi, C., 2013. NWA 5363: Remnants of a terrestrial embryo? 76th Annual Meteorit. Soc. Meet. Abstract #5185.
- Loeffler, M.J., Dukes, C.A., Baragiola, R.A., 2009. Irradiation of olivine by 4 keV He⁺: Simulation of space weathering by the solar wind. *J. Geophys. Res.* 114 (E03003), 2009. <http://dx.doi.org/10.1029/2008JE003249>.
- Lucey, P.G., Riner, M.A., 2011. The optical effects of small iron particles that darken but do not redden: Evidence of intense space weathering on Mercury. *Lunar Planet. Sci.* 42. Abstract #1333.
- Lucey, P.G., Keil, K., Whitely, R., 1998. The influence of temperature on the spectra of the A-asteroids and implications for their silicate chemistry. *J. Geophys. Res.* 103, 5865–5871.
- Marchi, S., Brunetto, R., Magri, S., Lazzarin, M., Gandolfi, D., 2005. Space weathering of near-Earth and main belt silicate-rich asteroids: Observations and ion irradiation experiments. *Astron. Astrophys.* 443, 769–775.
- Marcus, H.L., Hackett Jr., L.H., 1974. The low temperature fracture behavior of iron–nickel meteorites. *Meteoritics* 9, 371–376.
- Masiero, J.R. et al., 2011a. Main belt asteroids with WISE/NEOWISE I: Preliminary albedos and diameters. *Astrophys. J.* 770, 22–64.
- Masiero, J.R. et al., 2011b. Main belt asteroids with WISE/NEOWISE I: Preliminary albedos and diameters. *Astrophys. J.* 741 (68). <http://dx.doi.org/10.1088/0004-637X/741/2/68> (20pp.).
- Mason, B., 1963. The pallasites. *Am. Mus. Novit.* 2163, 1–19.
- Mason, B., 1965. The chemical composition of olivine–bronzite and olivine–hypersthene chondrites. *Am. Mus. Novit.* 2223, 1–37.
- Mason, B., Jarosewich, E., 1973. The Barea, Dyarll Island, and Emery meteorites, and a review of the mesosiderites. *Mineral. Mag.* 39, 204–215.
- Mason, B., Nelen, J.A., Muir, P., Taylor, S.R., 1975. The composition of the Chassigny meteorite. *Meteoritics* 11, 21–27.
- Matsui, T., Schultz, P.H., 1984. On the brittle–ductile behavior of iron meteorites: New experimental constraints. *J. Geophys. Res.* 89 (Suppl.), C323–C328, Proc. Lunar Planet. Sci. Conf. 15, Part 1.
- McCoy, T.J., Keil, K., Scott, E.R.D., Haack, H., 1993. Genesis of the III CD iron meteorites: Evidence from silicate-bearing inclusions. *Meteoritics* 28, 552–560.
- McCoy, T.J. et al., 1996. A petrologic, chemical, and isotopic study of Monument Draw and comparison with other acapulcoites: Evidence for formation by incipient partial melting. *Geochim. Cosmochim. Acta* 60, 2681–2708.
- McKay, G., Lindstrom, D., Yang, S.-R., Wagstaff, J., 1988. Petrology of unique achondrite Lewis Cliffs 86010. *Lunar Planet. Sci.* 19, 762–763 (abstract).
- Mikouchi, T., Chikami, J., Takeda, H., Miyamoto, M., 1995. Mineralogical study of LEW88774: Not so unusual ureilite. *Lunar Planet. Sci.* 26, 871–872 (abstract).
- Mittlefehldt, D.W., McCoy, T.J., Goodrich, C.A., Kracher, A., 1998. Non-chondritic meteorites from asteroidal bodies. In: Papike, J.J. (Ed.), *Planetary Materials. Reviews in Mineralogy*, vol. 36. Mineral. Soc. Am., pp. 4–1–4–195.
- Mittlefehldt, D.W., Bogard, D.D., Berkley, J.L., Garrison, D.H., 2003. Brachinites: Igneous rocks from a differentiated asteroid. *Meteorit. Planet. Sci.* 38, 1601–1625.
- Moroz, L., Schade, U., Wäsch, R., 2000. Reflectance spectra of olivine–orthopyroxene-bearing assemblages at decreased temperatures: Implications for remote sensing of asteroids. *Icarus* 147, 79–93.
- Mothé-Diniz, T., Lazzaro, D., Carvano, J.M., Florczak, M., 2000. Rotationally resolved spectra of some S-type asteroids. *Icarus* 148, 494–507.
- Mothé-Diniz, Carvano, J.M., Bus, S.J., Duffard, R., Burbine, T.H., 2008. Mineralogical analysis of the Eos family from near-infrared spectra. *Icarus* 195, 277–294.
- Nehru, C.E. et al., 1983. Brachina: A new type of meteorite, not a chassignite. *J. Geophys. Res.* 88 (Suppl.), B237–B244, Proc. Lunar Planet. Sci. Conf. 14.
- Noble, S.K., Pieters, C.M., Keller, L.P., 2007. An experimental approach to understanding the optical effects of space weathering. *Icarus* 192, 629–642.
- Noguchi, T. et al., 2011. Incipient space weathering observed on the surface of Itokawa dust particles. *Science* 333, 1121–1125.
- Pieters, C.M., 1983. Strength of mineral absorption features in the transmitted component of near-infrared light: First results from RELAB. *J. Geophys. Res.* 88, 9534–9544.
- Pompilio, L., Pedrazzi, G., Sgavetti, M., Cloutis, E.A., Craig, M.A., Roush, T.L., 2009. Exponential Gaussian approach for spectral modeling: The EGO algorithm. I. Band saturation. *Icarus* 201, 781–794.
- Powell, B.N., 1969. Petrology and chemistry of mesosiderites – I. Textures and composition of nickel–iron. *Geochim. Cosmochim. Acta* 33, 789–810.
- Powell, B.N., 1971. Petrology and chemistry of mesosiderites – II. Silicate textures and compositions and metal–silicate relationships. *Geochim. Cosmochim. Acta* 35, 5–34.
- Prinz, M., Nehru, C.E., Delaney, J.S., Harlow, G.E., Bedell, R.L., 1980. Modal studies of mesosiderites and related achondrites, including the new mesosiderite ALHA 77219. *Lunar Planet. Sci.* 11, 1055–1071.
- Prinz, M., Weisberg, M.K., Nehru, C.E., Delaney, J.S., 1986. A second Brachina-like meteorite. *Lunar Planet. Sci.* 17, 679–680 (abstract).
- Rager, H., Hosoya, S., Weiser, G., 1988. Electron paramagnetic resonance and polarized optical absorption spectra of Ni²⁺ in synthetic forsterite. *Phys. Chem. Miner.* 15, 383–389.
- Reddy, V., Hardsen, P.S., Gaffey, M.J., Abell, P.A., 2005. Mineralogy and temperature-induced spectral investigations of A-type Asteroids 246 Asporina and 446 Aeternitas. *Lunar Planet. Sci.* 36. Abstract #1375.
- Reddy, V., Nathues, A., Gaffey, M.J., Schaeff, S., 2011a. Mineralogical characterization of potential targets for the ASTEX mission scenario. *Planet. Space Sci.* 59, 772–778.
- Reddy, V., Carvano, J.M., Lazzaro, D., Michtchenko, T.A., Gaffey, M.J., Kelley, M.S., Mothé-Diniz, T., Alvarez-Candal, A., Moskovitz, N.A., Cloutis, E.A., Ryan, E.L., 2011b. Mineralogical characterization of Baptistina Asteroid Family: Implications for K/T impactor source. *Icarus* 216, 184–197.
- Remo, J.L., Johnson, A.A., 1975. A preliminary study of the ductile–brittle transition under impact conditions in material from an octahedrite. *J. Geophys. Res.* 80, 3744–3748.
- Rossmann, G.R., Shannon, R.D., Waring, R.K., 1981. Origin of the yellow color of complex nickel oxides. *J. Solid State Chem.* 39, 277–287.
- Roush, T.L., Singer, R.B., 1987. Possible temperature variation effects on the interpretation of spatially resolved reflectance observations of asteroid surfaces. *Icarus* 69, 571–574.
- Sanchez, J., Reddy, V., Kelley, M.S., Cloutis, E.A., Bottke, W.F., Nesvorný, D., Lucas, M.P., Hardsen, P.S., Gaffey, M.J., Abell, P.A., Le Corre, L., 2014. Olivine-dominated asteroids: Mineralogy and origin. *Icarus* 228, 288–300.
- Sasaki, S., Nakamura, K., Hamabe, Y., Kurahashi, E., Hiroi, T., 2001. Production of iron nanoparticles by laser irradiation in a simulation of lunar-like space weathering. *Nature* 410, 555–557.
- Sasaki, S., Hiroi, T., Nakamura, K., Hamabe, Y., Kurahashi, E., Yamada, M., 2002. Simulation of space weathering by nanosecond pulse laser heating: Dependence on mineral composition, weathering trend of asteroids and discovery of nanophase iron particles. *Adv. Space Res.* 29, 783–788.
- Sasaki, S., Kurahashi, E., Yamanaka, C., Nakamura, K., 2003. Laboratory simulation of space weathering: Changes of optical properties and TEM/ESR confirmation of nanophase metallic iron. *Adv. Space Res.* 31, 2537–2542.
- Sawyer, S.R., 1991. A High Resolution CCD Spectroscopic Survey of Low Albedo Main Belt Asteroids. Ph.D. Thesis, Univ. of Texas, Austin.
- Schade, U., Wasch, R., 1999. NIR reflectance spectroscopy of mafic minerals in the temperature range between 80 and 473 K. *Adv. Space Res.* 7, 1253–1256.
- Schulze, H., Bischoff, A., Palme, H., Spettel, B., Dreibus, G., Ottoa, J., 1994. Mineralogy and chemistry of Rumuruti: The first meteorite fall of the new R chondrite group. *Meteoritics* 29, 275–286.
- Scott, E.R.D., 1977. Pallasites–metal composition, classification and relationship with iron meteorites. *Geochim. Cosmochim. Acta* 41, 349–360.
- Scott, E.R.D., Bild, R.W., 1974. Structure and formation of the San Cristobal meteorite, other IB irons and group III CD. *Geochim. Cosmochim. Acta* 38, 1379–1391.
- Scott, E.R.D., Wasson, J.T., 1975. Classification and properties of iron meteorites. *Rev. Geophys. Space Phys.* 13, 527–546.
- Scott, E.R.D., Wasson, J.T., 1976. Chemical classification of iron meteorites – VIII. Groups IC, IIE, IIIF and 97 other irons. *Geochim. Cosmochim. Acta* 40, 103–115.
- Sherman, D.M., Waite, T.D., 1985. Electronic spectra of Fe³⁺ oxides and oxide hydroxides in the near IR to near UV. *Am. Mineral.* 70, 1262–1269.
- Singer, R.B., Roush, T.L., 1985. Effects of temperature on remotely sensed mineral absorption features. *J. Geophys. Res.* 90, 12434–12444.
- Smith, M.R. et al., 1984. Petrogenesis of the SNC (shergottites, nakhlites, chassignites) meteorites: Implications for their origin from a large diverse planet, possibly Mars. *J. Geophys. Res.* 89 (Suppl.), B612–B630, Proc. Lunar Planet. Sci. 14.
- Sunshine, J.M., Pieters, C.M., 1998. Determining the composition of olivine from reflectance spectroscopy. *J. Geophys. Res.* 103, 13675–13688.
- Sunshine, J.M., Binzel, R.P., Burbine, T.H., Bus, S.J., 1998. Is Asteroid 289 Nenetta compositionally analogous to the brachinite meteorites? *Lunar Planet. Sci.* 29. Abstract #1430.
- Sunshine, J.M., Bus, S.J., Burbine, T.H., McCoy, T.J., 2005. Tracing oxygen fugacity in asteroids and meteorites through olivine composition. *Lunar Planet. Sci.* 36. Abstract #1203.

- Sunshine, J.M., Bus, S.J., Corrigan, C.M., McCoy, T.J., Burbine, T.H., 2007. Olivine-dominated asteroids and meteorites: Distinguishing nebular and igneous histories. *Meteorit. Planet. Sci.* 42, 155–170.
- Takeda, H., Saiki, K., Otsuki, M., Hiroi, T., 1993. A new Antarctic meteorite with chromite, orthopyroxene, and metal with reference to a formation model of S asteroids. *Lunar Planet. Sci.* 24, 1395–1396 (abstract).
- Tholen, D.J., 1984. Asteroid Taxonomy from Cluster Analysis of Photometry. Ph.D. Thesis, Univ. of Arizona.
- Usui, F. et al., 2011. Asteroid catalog using Akari: AKARI/IRC mid-infrared asteroid survey. *Publ. Astron. Soc. Jpn.* 63, 1117–1138.
- Warren, P.H., Rubin, A.E., 2012. The Miller Range 090340 dunite: Not a uniquely ferroan ureilite, not even a ureilite. *Lunar Planet. Sci.* 43. Abstract #2528.
- Weisberg, M.K. et al., 2001. A new metal-rich chondrite grouplet. *Meteorit. Planet. Sci.* 36, 401–418.
- Weisberg, M.K., Boesenberg, J.S., Ebel, D.S., 2002. Gujba and origin of the Bencubbin-like (CB) chondrites. *Lunar Planet. Sci.* 33. Abstract #1551.
- Wood, B.J., 1974. Crystal field spectrum of Ni²⁺ in olivine. *Am. Mineral.* 59, 244–248.
- Yamada, M. et al., 1999. Simulation of space weathering of planet-forming materials: Nanosecond pulse laser irradiation and proton implantation on olivine and pyroxene samples. *Earth Planets Space* 51, 1255–1265.
- Yanai, K., 1994. Angrite Asuka-881371: Preliminary examination of a unique meteorite in the Japanese collection of Antarctic meteorites. *Proc. NIPR Symp. Antarct. Meteorit.* 7, 30–41.
- Yugami, K., Takeda, H., Kojima, H., Miyamoto, M., 1996. Distribution of opaque minerals in primitive achondrites. *Lunar Planet. Sci.* 27, 1483–1484 (abstract).
- Zukas, E.G., 1969. Metallurgical results from shock-loaded iron alloys applied to a meteorite. *J. Geophys. Res.* 74, 1993–2001.